UNIVERSITÀ DEGLI STUDI DI PALERMO

Dottorato di Ricerca in Tecnologie e Scienze per la Salute dell'Uomo

Dipartimento di Scienze e Tecnologie Biologiche Chimiche e Farmaceutiche

XXXVI Ciclo

Impact of Surrounding Environments on Spherical Supramolecular Assemblies Resulting from Liquid-Liquid Phase Separation and Aggregation of Globular Proteins

---

IL DOTTORE

Giuseppe De Luca

IL COORDINATORE

Prof. Bruno Giuseppe Pignataro

IL TUTOR

Prof.ssa Valeria Vetri

ANNO CONSEGUIMENTO TITOLO 2024

Università degli Studi di Palermo

Dottorato di Ricerca in Tecnologie e Scienze per la Salute dell'Uomo
Dipartimento di Scienze e Tecnologie Biologiche Chimiche e Farmaceutiche
Settore Scientifico Disciplinare FIS-07

Impact of Surrounding Environments on Spherical Supramolecular Assemblies Resulting from Liquid-Liquid Phase Separation and Aggregation of Globular Proteins

IL DOTTORE
GIUSEPPE DE LUCA

IL COORDINATORE
BRUNO GIUSEPPE PIGNATARO

IL TUTOR
VALERIA VETRI

CICLO XXXVI
ANNO CONSEGUIMENTO TITOLO 2024

Preface

This PhD thesis entitled "Impact of Surrounding Environments on Spherical Supramolecular Assemblies Resulting from Liquid-Liquid Phase Separation and Aggregation of Globular Proteins" was submitted to the Department of Biological, Chemical and Pharmaceutical Science and Technologies at the University of Palermo to obtain the PhD degree in "Technologies and Sciences for Human Health". The project was carried out in the Molecular Biophysics Laboratory, Department of Physic and Chemistry – Emilio Segrè at the University of Palermo, under the supervision of Full Professor Valeria Vetri.

During my PhD program, I completed a six-month research visit abroad at the European Synchrotron Radiation Facility (ESRF) in Grenoble, France. The research was carried out under the supervision of Dr. Marco Cammarata (Staff scientist at ESRF) and in collaboration with Dr. Giorgio Schirò (1st class Researcher at IBS).

The following review and research papers and manuscripts are the result of the work conducted during the PhD project:

- Anselmo S, **De Luca G**, Ferrara V, Pignataro B, Sancataldo G, Vetri V. *Insight into mechanisms of creatinine optical sensing using fluorescein-gold complex.* Methods Appl Fluoresc. 2022 Aug 5;10(4). doi: 10.1088/2050-6120/ac8524.

- Alfano C, Fichou Y, Huber K, Weiss M, Spruijt E, Ebbinghaus S, **De Luca G**, Morando MA, Vetri V, Temussi PA, Pastore A. *Molecular Crowding: The History and Development of a Scientific Paradigm.* Chem Rev. 2024 Mar 27;124(6):3186-3219. doi: 10.1021/acs.chemrev.3c00615. Epub 2024 Mar 11.

- **De Luca G**, Sancataldo G, Militello B, Vetri V, *Surface-Catalysed Liquid-Liquid Phase Separation and Amyloid-Like Assembly in Microscale Compartments.*, Journal of Colloids and Interface Science, (under minor revision), Available at SSRN: https://ssrn.com/abstract=4803885 or http://dx.doi.org/10.2139/ssrn.4803885

The presented thesis is organised as follows:

- In Chapter 1, a general introduction on the state of the art of the main topics that will be discussed in the following Chapters is reported, focusing on

protein folding, aggregation mechanisms and liquid-liquid phase separation process.

- In Chapter 2, the experimental approaches used to analyse the effects of environmental conditions on aggregation and liquid-liquid phase separation phenomena are described, highlighting how combining bulk spectroscopy and microscopy can comprehensively study spatially heterogeneous processes.

- In Chapter 3, the liquid-liquid phase separation of a Bovine Serum Albumin solution is examined, showing the influence of polyethylene glycol concentration and the impact of chaotropic and kosmotropic co-solutes. Water ordering is studied using ACDAN fluorescence as an indicator of solvent dipolar relaxation.

- In Chapter 4, the supramolecular self-assembly of Human Insulin in submicroliter aqueous compartments is examined. This process results in the formation of spherical Human Insulin microparticles. The process is analysed by a combination of quantitative fluorescence techniques.

- In Chapter 5, a summary of the results and conclusions are reported.

- In Appendix A, the activity conducted at ESRF in Grenoble is reported. An introduction to X-ray Photon Correlation Spectroscopy (XPCS) and preliminary results on the analysis of liquid-liquid phase separation by using XPCS are described.

Acknowledgments

I apologize to the reader; these acknowledgments will be written in Italian, to ensure that all those I thank will be able to read and understand them.

Grazie a Valeria, la mia tutor e mentore scientifica. Grazie per avermi introdotto qualche anno fa nel mondo della Biofisica e per essere stata una guida sempre presente da allora. Grazie per avermi sempre spronato a dare il meglio anche quando mi sembrava che il meglio non fosse necessario. Grazie per la tua onestà e schiettezza che mi hanno permesso di crescere infinitamente durante questi anni. Il tuo essere così idealista ancora a questo punto della carriera è fonte di ispirazione.

Un sentito ringraziamento a Marco e Giorgio, per l'immenso supporto, sia scientifico che personale, che mi avete offerto a Grenoble, durante il mio periodo all'estero.

Grazie ai miei colleghi di laboratorio passati e presenti. Grazie a Giuseppe (il nostro RTD di riferimento), Sara, Vittorio, Dirk, Daniele, Kleopatra, Martina, Giorgia ed Anna. Grazie per i momenti di confronto che mi hanno fatto crescere scientificamente e per i momenti di risate che hanno reso la vita in lab durante questi tre anni così piacevole.

Un grazie particolare va a Sara, Giorgia e Martina.

A Sara, per avermi supportato soprattutto all'inizio di questo percorso, quando ancora ero completamente spaesato e confuso.

A Giorgia, per essere sempre una spalla sempre affidabile in laboratorio. Come sai bene, ti stimo molto e ritengo che la tua dedizione, caparbietà e inventiva siano ammirevoli e da esempio.

Infine, a Martina, con la quale ho condiviso tutte le avventure e disavventure francesi. Quanti momenti di puro caos (anche a Palermo), quando nulla andava nella maniera prefissata sia scientificamente che personalmente. Grazie per la tua semplicità e per i preziosi consigli.

Grazie ai miei amici, Francesca, Roberta, Roberto (Pecos), Alice, Salvo, Giovanni e Lidia. Grazie per i suggerimenti e per i momenti di svago e di sfogo che mi hanno permesso di superare questo percorso senza perdere del tutto la sanità mentale.

Grazie alla mia famiglia. Grazie a mia madre e a mio padre, se oggi sto scrivendo queste parole è grazie a voi. Grazie per avermi mostrato ed insegnato sempre la bellezza e l'importanza dello studio. Grazie per essere sempre stati degli esempi da

seguire. Spero un giorno di essere un esempio per qualcun altro almeno la metà di quanto voi lo siate stati per me. Grazie a mia sorella il cui amore mi ha dato una spinta in più nel proseguimento di questo percorso. Vi voglio bene!

Grazie a Piera, la mia seconda mamma che mi ha accolto fin da subito a casa sua facendomi sentire subito parte della famiglia.

Infine, un infinito grazie a Claudia. Grazie per la tua pazienza e la tua tenacia. Grazie per il tuo immenso supporto in ogni circostanza. Grazie per la serenità che mi trasmetti ogni volta che torno a casa. Potrei continuare all'infinito, ma in sintesi, grazie per tutto quello che fai per noi e grazie per esserci sempre in ogni giorno della mia vita. Ti amo.

Abstract

Liquid-Liquid Phase Separation (LLPS) and protein aggregation share several fundamental features rooted in the principles of macromolecular interactions and phase behaviour. Both LLPS and aggregation are recurrent phenomena in nature and are related to the function and dysfunction of living systems and can be interconnected as they are driven by common general principles. These processes involve the transition of proteins from a soluble state to a high-density state, regulated by common dominant intermolecular interactions, such as hydrophobic interactions, electrostatic interactions, and hydrogen bonding. In LLPS, these interactions lead to the formation of distinct liquid phases within a solution, where one phase is protein-rich and the other contains a minor amount of protein molecules. In addition, polyvalent interactions may also coordinate phase transition leading to protein aggregation, which involves the formation of stable intermolecular bonds and resulting in stable solid soluble or insoluble supramolecular assemblies. These phenomena are highly sensitive to environmental conditions such as pH, temperature, ionic strength, the presence of crowding agents, and surface and excluded volume effects, all of which influence the stability and dynamics of protein-protein interactions.

This PhD thesis focuses on the analysis of the supramolecular assembly mechanisms of globular protein in conditions where micron-scale spherical particles are formed both in the liquid state and in the solid state. The analysis of LLPS phenomena of Bovine Serum Albumin is presented in bulk with the aim of highlighting the role of solvent in orchestrating phase transition and how factors such as polarity and molecular order of the medium may affect the formation of protein coacervates. Then the supramolecular assembly of Insulin was studied within submicroliter scale aqueous compartments. A new experimental setup was developed allowing the revealing of a surface-catalysed LLPS triggered by nucleation mechanisms. The presented studies are performed by means of a combination of classical spectroscopic techniques and quantitative fluorescence microscopy. The combination of these techniques with highly sensitive and specific dyes enables the visualization and analysis of characteristic features of the samples under investigation. In particular, Thioflavin T fluorescence lifetime was used to gain information on the molecular structure of supramolecular protein assemblies with high spatial resolution, and ACDAN fluorescence signal was used to probe molecular order and polarity during phase transition. At the end of the thesis, work in progress and

preliminary results of experiments performed using X-ray photon correlation spectroscopy are presented. Although challenging to use in biological samples, this technique may provide unique and valuable information on the microscopic dynamics of density fluctuation and global diffusive motions occurring during LLPS. Beyond the specific results of individual studies, the experimental approaches described in this thesis may also constitute an important outcome. The feasibility of establishing ad hoc conditions to study these phenomena from multiple perspectives could potentially lead to a more comprehensive understanding of these complex and still not fully understood processes.

Contents

Acronyms

2PE   Two-photon excitation.

2PM   Two-photon Microscopy.

BSA   Bovin Serum Albumin.

CLSM   Confocal Laser scanning fluorescence microscopy.

EtOH   Ethanol.

FLIM   Fluorescence lifetime imaging microscopy.

FRAP   Fluorescence Recovery After Photobleaching.

FTIR   Fourier Transform Infrared.

GP   Generalized Polarization.

HI   Human Insulin.

IRF   Instrumental Response Function.

LE   locally excited.

LLPS   Liquid-Liquid Phase Separation.

MPE   multi-photon excitation.

PEG   polyethylene glycol.

PSF   Point Spread Function.

ROI   regions of interest.

SAXS   Small-Angle X-ray Scattering.

TCSPC   Time-Correlated Single-Photon Counting.

ThT   Thioflavin T.

TICT   Twisted Internal Charge-Transfer.

TTC   Two-Times Correlation.

WLL   White Light Laser.

XPCS   X-ray Photon Correlation Spectroscopy.

CHAPTER 1

Introduction

This chapter provides a brief general introduction on the basic concepts and the state of the art of the mechanisms and processes useful to underlie the scientific issues and the experimental conditions depicted in this thesis. Protein folding and aggregation in the energy landscape perspective are briefly described, with a particular focus on amyloid self-assembly. Liquid-Liquid Phase Separation (LLPS) processes and the molecular crowding effects are described.

1.1 PROTEIN FOLDING

Proteins are fundamental macromolecules that play a vital role in all biological processes. Proteins are comprised of one or more long chains of amino acids, linked together by peptide bonds. Amino acids are small organic compounds that represent the building blocks of proteins. Each amino acid consists of a carbon atom bonded to an amine group (-NH2), a carboxyl group (-COOH), a hydrogen atom, and a distinctive side chain, known as the residue. The chain of amino acids without considering the residues is known as the protein backbone. The side chain gives each amino acid its specific chemical and physical characteristics. Amino acids can be hydrophobic, polar charged (positively or negatively), or neutral [1, 2, 3].

The chemical properties of amino acids are crucial for protein structure, as it can be modulated by specific intramolecular interactions between individual residues of the amino acid chains, resulting in a functional structure essential for the proper functionality of living systems. This process, known as folding, has been the subject of extensive research since the 1970s. Folding involves molecular interactions such as electrostatic forces, hydrophobic effects, hydrogen bonding, and Van der Waals interactions, which drive the protein to adopt a particular shape or conformation [2, 4].

The main driving interaction regulating protein folding is the hydrophobic interactions, which drive non-polar amino acid side chains to the interior of the protein structure, away from the aqueous environment. This effect is primarily due to the entropy gain associated with the release of water molecules from the ordered

solvation shell around hydrophobic groups, called clathrates. This results in the hydrophobic compounds sticking to each other, forming clusters that reduce the surface area available to water molecules and, consequently, the number of ordered water molecules around them [2, 4, 5].

The hydrophobic interactions are significantly influenced by temperature. At lower temperatures, water molecules are more structured and form extensive hydrogen-bonded networks. In such conditions, the entropic gain from releasing these water molecules is less pronounced, reducing the hydrophobic effect. As temperature increases, the hydrogen-bonded network of water becomes more dynamic and less structured, increasing the entropy gain when water molecules are displaced from the hydration shell of hydrophobic residues [2].

Additionally, to the hydrophobic interactions between nonpolar residues, electrostatic interactions, van der Waals forces and hydrogen bonds, further stabilize the folded conformation. Electrostatic interactions are long-range columbic interactions which arise between charged residues. Van der Waals are weak, short-range intermolecular forces that arise from interactions between neutral molecules. These may be attractive or repulsive forces between permanent or transient dipoles of the molecules. Van der Waals forces, though individually weak, collectively provide significant stabilizing energy through close packing of atoms in the protein core. Hydrogen bonds form between polar side chains and backbone atoms, or water molecules and in general these occur when a hydrogen atom is shared between generally two electronegative atoms and provide specificity and directionality to the folding process [2, 6].

Similarly to hydrophobic effects, the strength and behaviour of these interactions are significantly influenced by the conditions of the surrounding solution, such as solvent, ionic strength, pH, and temperature. For instance, high ionic strength in a solution, due to high salts concentrations, may shield the electrostatic interactions, reducing the range and strength of these interactions and changes in pH can alter the charge state of ionizable groups in polar residues, influencing the nature and strength of electrostatic interactions. Van der Waals forces are influenced by temperature since high temperatures increase molecular motion, which can weaken the cumulative effect of van der Waals forces by disrupting the close contacts between molecules. Hydrogen bonding is highly sensitive to the solution environment since changes in pH can protonate or deprotonate hydrogen bond donors or acceptors, altering their ability to form hydrogen bonds and, as for van der Waals interactions, increased temperature generally weakens hydrogen bonds by increasing thermal motion, which disrupts the directional and specific nature of these interac-

tions [2]. Moreover, hydrogen bonding with water molecules is strongly influenced by specific chemical compounds which are known to disrupt or strengthen the hydrogen bonds which are formed in water. These are respectively chaotropic and kosmotropic agents. More details on this compound will be given in Chapter 3.

Overall, the interplay between these interactions orchestrates the complex and highly cooperative process of protein folding, ensuring that the protein adopts its native and functional three-dimensional structure.

Now a brief overview of protein structure will be reported, in order to comprehend how these interactions, cooperate to guide a protein towards its native three-dimensional structure. The structure of protein molecules can be organized into four levels characterized by increased complexity: primary, secondary, tertiary, and quaternary [2, 3]. The primary structure is the linear sequence of amino acids in the polypeptide chain and dictates the subsequent levels of protein structure. The amino acid sequence is locally folded in specific structures which describe the secondary structure of the protein. These structures are stabilized primarily by intramolecular hydrogen bonds between the backbone atoms of the amino acids. The two most common types of secondary structure are α-helices and β-sheets. In an α-helix, the backbone of the protein forms a tightly coiled structure resembling a helix, and the β-sheets consist of extended strands of amino acids aligned side by side, with hydrogen bonds forming between adjacent strands [2, 3]. These secondary structures provide stability and rigidity to the protein molecule, contributing to its overall conformation and function. Additionally, random coil can occur between secondary structure elements, facilitating changes in direction and connecting different regions of the polypeptide chain, providing flexibility to the overall protein structure [2, 3]. The three-dimensional spatial conformation of secondary structure elements is the tertiary structure of the protein. The tertiary structure is stabilized by interactions that arise between the residues and interactions with the solvent molecules. This level of structure is stabilized by a variety of interactions, including hydrogen bonds, hydrophobic interactions, van der Waals forces, ionic bonds (salt bridges), and disulfide bridges, which occur between cysteine residues. The specific arrangement of these interactions creates a unique three-dimensional conformation that is critical for the protein function [2, 3]. Some proteins may further assemble into polymeric forms which are composed of multiple identical protein monomers, which is the quaternary structure. The subunits in a quaternary structure are typically held together by non-covalent interactions, such as hydrogen bonds and ionic bonds. The spatial arrangement of these subunits is highly specific and determines the overall geometry and stability of the protein complex. Examples of proteins

with quaternary structure include haemoglobin, which is composed of four subunits and insulin, which is commonly found as hexamers where zinc atoms coordinate six insulin molecules [2, 3].

Proteins that exhibit an ordered and regular structure, composed of 50%-70% α-helices and β-sheets, are referred to as globular proteins. Globular proteins are characterized by their compact, spherical shapes, which result from the folding of polypeptide chains into a tightly packed, three-dimensional structure. They are typically soluble in water, having a hydrophobic core surrounded by hydrophilic residues, which form the protein surface. Usually, if these proteins have disorder random coil, they are found at the edge of the protein molecule because these present a higher number of available atoms to create hydrogen bonds with solvent, with respect to the ordered α-helices and β-sheets [2, 3]. This makes globular proteins very stable, still maintaining a good degree of flexibility. For these reasons, these proteins play crucial roles in numerous biological processes. Examples of globular proteins include insulin, a peptide hormone necessary in the metabolism of glucose and Serum Albumins, a family of transport proteins found in blood.

The process of correctly folding a polypeptide chain into its native and functional state (or simply folding) is driven by an interplay of the several interactions discussed above [2, 4, 5]. The folding process can be described by the energy landscape, as shown in Figure 1.1. Each point of the energy landscape described a specific conformational state of the protein. The width of the funnel-shaped energy landscape is a representation of all the different conformations characterised by the same free energy, and therefore it is associated with the entropic contributions to the folding process [2, 7, 8, 9]. During the folding process the protein travels downhill, decreasing the number of possible conformation state and minimizing the free energy of the system. The funnel profile of the energy landscape is due to the enthalpic and entropic contributions arising from both intramolecular interactions between amino acids, and interactions with the solvent and the overall surrounding environment [2, 7, 8]. The valleys in this landscape denote stable states for the protein molecules. Under specific conditions, it is known that a protein amino acid chain can spontaneously fold by the intrinsic chemical characteristics of the amino acid sequence; however, the specific folding depends on the particular environmental context. The energy landscape facilitates the protein transition into its native state through numerous pathways and intermediates; a smoother funnel surface typically denotes a faster folding process [7, 8, 9]. Environmental fluctuations may drive reactions towards native or non-native contacts while the protein is in its unfolded or partially folded states.
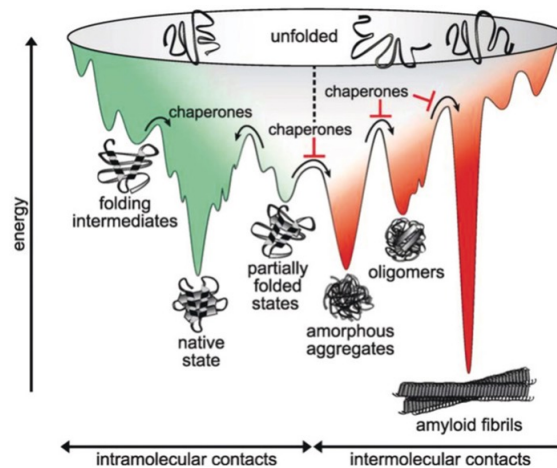
FIGURE 1.1: *Energy landscape for protein folding and protein aggregation processes. During the folding process (shown in green), protein molecules explore various conformations while moving towards the lower part of the "funnel", i.e. the native and functional state of the protein conformation, minimizing its free energy. During this process, protein may be trapped in a misfolded or partially folded state. This may shift the process towards the aggregation pathway, leading to the formation of aggregate species (shown in red), either amorphous aggregates, oligomers or amyloid fibrils, the latter being the most thermodynamically stable state of protein conformation. Figure adapted from [7].*

The molecular interactions underlying protein folding and aggregation process are essentially the same and therefore it is now accepted that the two processes are governed by the same physical principles. As previously explained, the interactions governing folding can be strongly influenced by the surrounding environment (temperature, pH, ionic strength, solvent polarity, etc.), therefore affecting whether the folding process collapses into the formation of the functional state (shown in green) or if it shifts towards the formation of aggregate species (shown in red). As can be observed by the energy landscape in Figure 1.1 in fact if the protein molecule partially folds or misfolds may result in the formation of aggregate species [7, 8, 9].

Moreover, as previously explained, the interactions governing the folding and aggregation process can be strongly influenced by the surrounding environment (temperature, pH, ionic strength, solvent polarity, etc.), therefore the balance between the two processes as well. For instance, the heightened entropic benefit enhances the hydrophobic effect, promoting the aggregation of non-polar side chains and thereby facilitating protein folding. However, if the temperature becomes too high, the destabilization of the protein structure may occur due to excessive thermal motion, potentially leading to denaturation. Thus, the hydrophobic effect exhibits an optimal temperature range where it most effectively drives protein folding.

1.2 AMYLOID AGGREGATES

In the case of off-pathway folding, which leads to the formation of aggregate species, the external condition may drift the process towards the formation of amorphous aggregates or amyloid fibrils. These are known to represent the most thermodynamically stable state within the energy landscape [10, 11], as it is also visible from the narrow and deep peak shown in Figure 1.1.

Amyloid fibrils are elongated (several micrometres long), very thin (few nanometres in width) supramolecular assemblies characterized by a peculiar cross-β structure. The cross-β structure is a distinctive and highly ordered arrangement of β-strands (the elemental part of β-sheets structure). β-strands align perpendicularly to the fibril axis and form extensive β-sheets that run parallel to the fibril axis. These sheets are stabilized by a dense network of hydrogen bonds between the peptide backbones of the β-strands, creating a rigid, very stable and insoluble structure. By x-ray diffraction measurements, the characteristic length of the cross-β structure were revealed. The distance between the β-strands is about 4.7 Å, whereas the separation between β-sheets is approximately 10 Å [12, 13]. At mesoscopic scale, amyloid fibrils are formed by the lateral association of few protofibrils characterized by the same cross-β structure.

Due to the high thermodynamic stability, amyloid aggregates exhibit remarkable mechanical and phisico-chemical properties, such as high young modulus, high electrical conductivity, resistance to harsh conditions and chemical oxidation [14, 15, 16]. Amyloid aggregates exhibit a remarkable property of structural universality, meaning their formation is largely independent of the specific amino acid sequence of the constituent proteins or peptides. This generic nature of amyloid fibrils is primarily due to the fundamental biophysical principles governing their assembly. Although amyloid fibrils represent the most stable state for a protein, altering solution conditions can shift the balance between hydrophobic, electrostatic, and hydrogen bonding interactions. This, in turn, can induce structural modifications in protein molecules or aggregates [17, 18, 19, 20]. For example, changes in the pH, in the solvent properties and more in general in solution and experimental conditions, may change the intra and intermolecular interactions resulting in different species aggregates species and in different assembly kinetics [18, 19, 20, 21].

Due to their dependence on specific experimental conditions amyloid aggregates exhibit a remarkable feature known as polymorphism, despite the generic and sequence-independent nature. Polymorphism refers to the ability of amyloid fibrils to adopt multiple distinct structural forms, even when formed from the same

peptide or protein sequence [8, 19]. Throughout the process of amyloid formation, a spectrum of aggregated species may emerge. This is influenced by both the protein sequence and external conditions, leading to the generation of various intermediate states with distinct structures and specificities. These intermediate states play a crucial role in governing the kinetics and characteristics of the final aggregates. Amyloid-like fibrils are just one of the many species that arise during the aggregation process. Amyloid cross-β structures can further assemble in the so-called three-dimensional superstructure, the most common being particulates and spherulites. Examples of these structures are shown respectively in Figures 1.2a) and 1.2b). These structures form under specific, tunable experimental conditions for various globular proteins.

Protein particulates (Figure 1.2a) are small amyloid-like aggregates. They form at pH near the isoelectric point of the protein under investigation, that is, under conditions of reduced electrostatic charge on the proteins. Their size is on the order of a few micrometres, and they were observed for a variety of protein molecules as β-lactoglobulin, bovine serum albumin, bovine insulin, horse heart myoglobin, hen egg white lysozyme, human transthyretin, human a-synuclein [22], equine lysozyme (see Figure 1.2a) [23], α-lactalbumin [24].
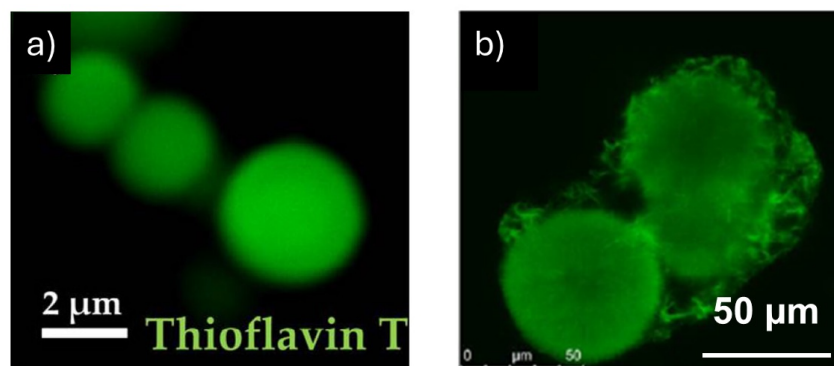
FIGURE 1.2: *Fluorescence microscopy images of amyloid tree-dimensional superstructure: a) equine lysozyme particulates and b) insulin spherulites. Adapted from [19, 23].*

Particulates are very dense and resistant structures and there is no evidence suggesting that these particulates are formed by the specific packing of amyloid fibrils. In contrary particulates formation seems to be driven by Liquid-Liquid Phase Separation (LLPS) process [24, 25]. Particulates in fact form at high temperatures at which protein molecules partially unfold, promoting the hydrophobic interaction between protein molecules. These interactions are mediated by water molecules, which may lead to the formation of spherical droplets, which undergo a very fast liquid-to-solid transition due to the high temperature [25, 26].

Particulates have a peculiar secondary structure, being in an intermediate state between native and amyloid structure [22, 24], presenting minor structure reorganization. This was observed both by Fourier Transform Infrared (FTIR) spectroscopy and by exploiting the fluorescence property of Thioflavin T. Cross-β structures have in fact a strong Infrared signal at 1620 cm^{-1} within the Amide I band [27]. Thioflavin T (ThT) is a gold standard fluorescent dye to study amyloid which will be discussed in the next chapter. In these context, particulates usually present a low, but visible, amyloid IR peak, and they are positive to ThT, indicating an amyloid structure. These observations are also confirmed by the x-ray diffraction pattern which resembles the characteristic distances observed in amyloid-like fibrils [19]. For these reasons, they are often referred to as amyloid-like structures. Another interesting feature of particulates was investigated by Fennema Galparsoro et al. [24] who analysed particulates of α-lactalbumin. They observed that the physical state of these structures depends on the incubation time of particulates. In fact, after 5 hours of incubation, upon decreasing the pH of the solution, α-lactalbumin particulates can be dissolved, in oligomeric species, while at higher incubation time, the particulates remain stable when exposed to acidic conditions.

Contrarily to particulates which have a homogeneous structure, spherulites present a highly heterogeneous structure (see Figure 1.2b) as reference). They are structured in core-corona morphology. The core of spherulites is amorphous and the corona is composed of amyloid fibrils which grow radially from the core [28, 29, 30] . By means of Micro-FTIR we were previously able to explore the secondary structure of insulin within spherulites with micrometric spatial resolution. These measurements showed that the core of the spherulites present a native structure and the 1620 cm^{-1} amyloid component increases towards the edges of the spherulites. Similarly, also the affinity of ThT increase in the same trend. Moreover, the amorphous core of the spherulites was found to be more densely packed than the fibrillar corona [28]. Spherulites are larger than particulates in fact their size is in the order of tens or even hundreds of micrometres. Spherulites form during temperature treatment when proteins are highly charged and therefore at pH far from the isoelectric point of the protein. Moreover, for some proteins, the spherulites coexist with amyloid fibrils, occurring in similar experimental conditions. However, spherulites occur only at quiescent conditions [29]. An example of such a process is insulin molecule, which will be explored in the next chapter. Spherulites present a characteristic pattern, called Maltese cross, observable by cross-polarized light microscopy. This pattern indicates that the outer shell is highly ordered, while the core is more disordered, in line with what was already reported. Spherulite formation and morphology were

8

studied under various conditions as the presence of surfaces and in the solution containing Ethanol to change the polarity of the environment. Surfaces were observed to promote the anisotropic growth of the spherulites [31]. The addition of ethanol changes the polarity of the environment. This results in a slowdown of the aggregation process and the final physical properties of the aggregate. For instance, the spherulites formed in presence of ethanol are deformed, if subjected to high pressure, with respect to the control spherulites which are more resistant to pressure increase [21].

1.3 NUCLEATION MECHANISMS

The microscopic mechanism underlying the protein self-assembly, and the growth of amyloid aggregates will be now discussed. This is of particular interest for the study reported in Chapter 4. The main models to describe amyloid aggregation take into account amyloid fibrils, being the "standard" amyloid aggregate.
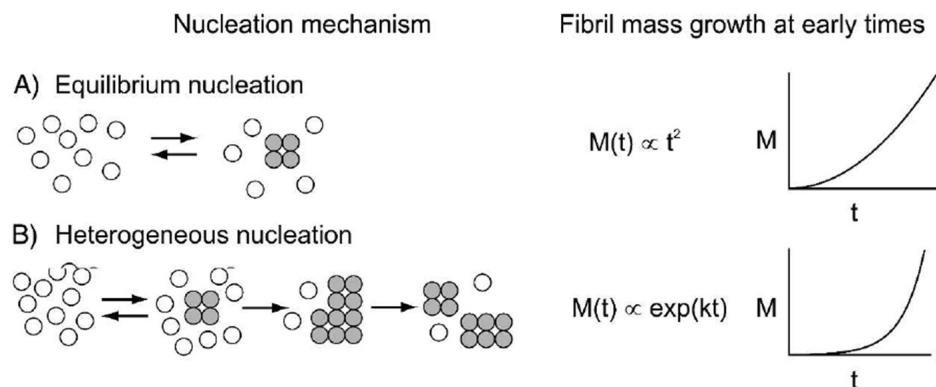

FIGURE 1.3: *Representation of the two nucleation mechanisms: A) primary nucleation mechanism, B) secondary nucleation mechanism. The aggregation kinetics regulated by primary nucleation follow a quadratic trend while the one regulated by a secondary nucleation mechanism is exponential. Adapted from [32].*

Aggregation kinetics describes the rate and pathway through which proteins or peptides transition from soluble monomers to insoluble aggregates, including oligomers, protofibrils, and mature amyloid fibrils. This process typically involved different mechanisms: the nucleation, the growth of the aggregate and the equilibrium process, where the aggregation no longer takes place [33]. Nucleation is a critical initial step in the aggregation process of amyloid fibrils, playing a pivotal role in determining the kinetics and pathway of amyloid formation. This process involves the formation of a small, unstable cluster of misfolded protein or peptide molecules, known as a nucleus, which acts as a template for further aggregation.

9

This process is responsible for increasing the number of aggregates. Two types of nucleation processes exist, primary nucleation, also known as homogeneous nucleation, and secondary nucleation, also known as heterogeneous nucleation. A representation of these two nucleation mechanisms is shown in Figure 1.3. Primary nucleation is the nucleation which arises from the monomers in solution. These interact forming oligomers and more complex species from which the aggregation occurs (Figure 1.3a). The polymerization of various functional filaments, such as actin [34] and tubulin [35], has been shown to proceed through primary nucleation. The secondary nucleation indicates an auto-catalytic process, where the nuclei, from which an aggregation event begins, form on the surface of a preexisting aggregate or the fragment of larger aggregates (Figure 1.3b). This process was found to be main mechanism of aggregation in many systems [32, 36, 37, 38, 39, 40]. Moreover, all the aggregation processes where different aggregates species occurs can be considered heterogeneous. Clearly, each aggregation process has to start from a primary nucleation, but during the aggregation, the two nucleation mechanisms may coexist. Which of the two processes is more predominant depends on the experimental conditions, such as the identity of the protein, the temperature at which the aggregation process occurs, the concentrations of protein or solutes, pH, etc. The nucleation mechanism strongly affects the time dependence of the aggregation process. The aggregation kinetics where a primary nucleation mechanism is predominant follow a quadratic time dependency. Secondary nucleation, being an autocatalytic process, results in a faster process and the aggregation kinetics has an exponential dependency over [41, 42] (shown in Figure 1.3b).
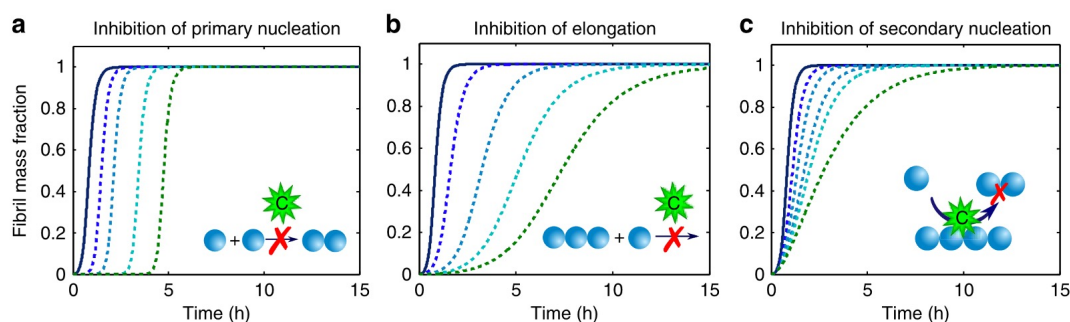
FIGURE 1.4: *Effects of microscopic mechanism in the aggregation process: numerical simulation of the aggregation kinetics illustrates how the inhibition of a) primary nucleation, b) elongation and aggregate growth, and c) secondary nucleation affect the aggregation kinetics shape. a) The inhibition of primary nucleation leads to an increase in the duration of the lag phase, maintaining the growth phase unaltered. b) A reduction of the elongation process results in the increase of the lag and reduction of the growth phase. c) The reduction of the secondary nucleation rate changes the shape of the kinetics from sigmoidal to concave, while the lag phase remains unaffected. Adapted from [41]*

By studying the aggregation kinetics, it is possible to gain important information on the underlying mechanisms of the aggregation process [41, 43, 44, 45]. The shape of the kinetics may explicit the mechanisms which drive the aggregation process. If a process is dominated by a single nucleation mechanism the shape of the kinetics may be different. In bulk, if the aggregation process is dominated by secondary nucleation, the kinetics has a sigmoidal shape, while if it is dominated by secondary nucleation mechanism, the kinetics has a concave shape, as shown by the Figure 1.4a) and 1.4c) [41]. In any case, the aggregation kinetics is composed of three phases: lag phase, growth phase, and equilibrium phase. During the lag phase, the system undergoes a period of minimal observable aggregation as nuclei slowly form and small aggregate growth as well. Once the majority of nuclei are formed, the process transitions into the growth phase, characterized by a rapid increase in aggregate formation. Secondary processes, such as fragmentation and secondary nucleation, further accelerate this phase by generating additional nucleation sites. Finally, the system enters the equilibrium phase, where the rate of monomer addition balances with the rate of fibril dissociation. In this phase, the concentration of monomers and fibrils reaches a dynamic equilibrium, and the overall level of aggregation stabilizes. Even if many processes occur in the lag phase, in first approximation, it can be associated with the primary nucleation rate, therefore a decrease of the lag phase mainly indicates an increase of the lag phase, as shown by Figure 1.4a). The elongation and the secondary nucleation strongly affect the growth phase of the aggregation kinetics.

1.4 Liquid-liquid phase separation

Liquid-Liquid Phase Separation (LLPS) is a fundamental biophysical process whereby a homogenous solution of biomacromolecules separates into two distinct liquid phases, a diluted phase and a concentrated or condensed phase [26, 46, 47, 48]. These two phases coexist and are in dynamical equilibrium with each other. The concentrated phase which results in a LLPS occurs in the form of spherical liquid droplets. LLPS is responsible for the formation of many structures within the cell which are not bound by a membrane. These are called membrane-less organelles and are involved in a variety of cellular processes, playing a critical role in cellular organization, biochemical reaction regulation, and signal transduction [46, 48, 49].

The molecular driving mechanisms underlying the formation of membrane-less organelles within the cellular environment are often studied in vitro using model systems to control and selectively manipulate the experimental condition. This al-

11

lows for a detailed analysis of the fundamental principles governing phase separation, free from the complexities of the cellular milieu. By investigating this process in vitro, it was observed that, similarly to aggregation processes, LLPS is a general process which can occur for many if not all proteins [49, 50]. Both intrinsically disordered proteins and well-structured proteins as globular proteins were observed to undergo LLPS process, resulting in the formation of spherical liquid coacervates. Moreover Wang et al. [51] have more recently reported that even oligomeric peptides may undergo LLPS in vitro in specific experimental and solution conditions, further suggesting the generality of this process. In particular, this phase separation is stimulated by factors such as low temperature, crowding agents like polyethylene glycol (PEG), and pH levels close to the isoelectric point. Depending on the solution conditions, coacervates may be composed of one molecular species (homotypic coacervation) or two or more molecular species (heterotypic coacervation). The sample coacervation occurs through the self-association of the protein upon variation of the environmental conditions such as temperature, pressure, pH [50, 52, 53]. Protein association is regulated by the same interactions which regulate the aggregation process, but to a different extent, since the interactions within a liquid phase are weaker and transient. This is an indication of the strong dependence of LLPS processes by the environmental conditions. Contrarily to aggregation processes, LLPS is a reversible phenomenon allowing phase-separated droplets to dynamically form and dissolve in response to changes in the environmental surroundings.

LLPS is driven by a balance of enthalpic and entropic contributions [47, 48]. Enthalpic contributions arise from favourable intermolecular interactions, such as hydrogen bonds, van der Waals forces, and electrostatic interactions, between the aggregated molecules. These interactions lower the overall enthalpy of the system, stabilizing the dense phase. The entropic contribution to LLPS is more difficult to evaluate because the process creates two phases with markedly different entropic characteristics. In the dense phase, water molecules are more bound and restricted due to their interactions with the concentrated protein molecules, resulting in lower entropy with respect to the homogeneous [54]. Conversely, in the dilute phase, water molecules are freer and behave more like bulk water, contributing to higher entropy [55]. This significant difference in water molecule behaviour between the two phases complicates the accurate assessment of the overall entropic contribution to the phase separation process.

Nevertheless, enthalpically favourable multivalent protein-protein interactions and protein-water interactions are necessary for LLPS to occur [48, 55]. In particular, the coacervation process takes place when protein-protein interactions become

more favourable than protein-water interactions, resulting in protein association. Thus, as already mentioned all the main interactions which occur between protein molecules and between protein and solvent discussed above are involved in the process. For this reason, LLPS is often described to be driven by multivalent interactions [26, 48]. Importantly, whether a solution undergoes phase separation strongly depends on the environmental conditions and the concentration and identities of the protein. Factors such as temperature, salt type and concentration, co-solutes, pH, and the volume excluded by other molecules play crucial roles in determining phase separation [26].

In this context, the contribution from hydration water to the LLPS is essential to study but nevertheless, it is largely unanalysed. The contributions of local hydration water to the thermodynamics of protein interactions are challenging to map accurately. Hydrophilic and hydrophobic hydration water populations have distinct thermodynamic properties that are difficult to isolate and measure. Standard calorimetry approaches, which are typically used to study these interactions, cannot provide the detailed local mapping required to understand these contributions fully [56, 57]. Additionally, the local hydration environment around proteins is influenced by numerous factors, making it a complex system to study. In a recent study by Pezzotti et al. [54] THz spectroscopy was used to explore the role of hydration water in LLPS, showing the entropic gain from realizing bound-water during LLPS process undergone by α-elastin.

The main model assessing the role of water in LLPS is the Flory–Huggins theory [58]. According to this theory whether the phase transition of a polymer or protein solution occurs is dictated by the water-water, water-protein, and protein-protein interaction. The theory introduced a parameter χ to quantify the energetic cost associated with polymer chain sites being occupied by solvent molecules rather than interacting with another chain. When $\chi < 0$, the interactions between the protein and water molecules are energetically favourable, causing the polymer to dissolve, resulting in a homogeneous solution regime. Conversely, when $\chi > 0$, interactions between protein molecules are energetically favoured over interactions with the solvent, leading to the polymer adopting a compact conformation, indicating that the proteins are not soluble in water, i.e. hydrophobic protein. Ultimately, as χ reaches critical values ($\chi \gg 0$), enthalpic changes become dominant over the entropy of mixing, resulting in a positive contribution to the free energy of mixing. As a consequence, the solution separates into two phases, a protein-rich phase and a protein-depleted phase, and therefore LLPS occurs. This theory is simplified, considering just one protein but it can be adapted to systems containing more

13

than one component. Remarkably, recent studies have utilized this model to predict the phase diagrams of intracellular proteins [59, 60, 61]. However, the limitation of this theory is that it considers proteins/polymers as neutral homogeneous chains and therefore cannot account for electrostatic interactions.

An important aspect that was not discussed until now is the effect of macro-molecular crowding on LLPS [47]. Macromolecular crowding can induce LLPS of proteins by strengthening intermolecular interactions. Crowding agents can influence the formation and composition of the dense phase. The role of molecular crowding in the context of LLPS is complex and not fully understood yet. Certainly, it implies a combination of forces and interaction that occur between molecules, which usually promote LLPS. Synthetic crowding agents, such as PEG, Ficoll or dextran, are commonly added in studies of protein LLPS in vitro [62, 63]. The presence on PEG and other synthetic crowding was reported to induce phase separation in conditions where phase separation does not occur and to reduce the concentration of protein needed for phase separation. Park et al. [64] observed how the addition of PEG to a solution containing poly-lysine and hyaluronic acid, which undergoes phase separation already, led to an increase of the coacervates volume fraction and to a decrease of the transition temperature. This result was attributed to the dehydration of the other components of the samples induced by PEG. However, the interactions between PEG or the other synthetic crowders and protein molecules depend on the specificity of the proteins.

The general mechanism to explain why molecular crowding promotes the LLPS is the excluded volume. The excluded volume is the reduction of available volume for protein molecules. This primarily stabilizes the folded state of the protein, by reducing the conformational entropy. This was for the first time proposed by Minton [65] in 1981 and more recently it was also observed experimentally [66, 67]). The excluded volume effect is also expected to favour protein association [65], due to the depletion interactions. These are attractive interactions which arise from the entropically-driven reduction of excluded volume which occur if two single protein molecules combine, as the associated state of protein molecules is more compact. The overall effect is a non-specific attraction between the protein molecules, which result in the increase of protein-protein interactions.

Experimental approaches

This chapter provides a brief overview of the experimental techniques employed in this thesis, along with a summary of the methods utilized in the conducted experiments. The main aim of this chapter is to highlight how the combination of bulk spectroscopy and microscopy techniques may give a comprehensive framework for spatial heterogeneous processes as LLPS phenomena. The presented approach allows to monitor the time evolution of the involved events, since the early stages at different spatial scales.

2.1 UV-Vis absorption spectroscopy

Ultraviolet-visible (UV – Vis) absorption spectroscopy is used to measure the concentration of molecules which have an intrinsic chromophore, such as proteins and fluorescent dyes. The concentration is measured by means of the Lambert-Beer law:

$$A = \epsilon \cdot C \cdot d \tag{2.1}$$

where A is the absorption, ϵ is the molar extinction coefficient, C is the concentration and d is the optical path of the sample. The extinction molar coefficient ϵ is an intrinsic characteristic of the chromophore and it is the absorbance per unity of concentration and optical path. In particular, the aromatic amino acids in protein (tryptophan, tyrosine and phenylalanine), absorb radiation at about 280 nm.

Molecular concentrations were measured by UV – Vis spectroscopy using a Jasco – V770 spectrophotometer. The molar extinction coefficient used for Human Insulin is $\epsilon = 1$ at 276 nm for 1.0 mg/ml, for Bovine Serum Albumin is $\epsilon = 0.667$ ml mg^{-1} cm^{-1} at 280 nm, for ThT is $\epsilon = 36,000$ M^{-1} cm^{-1} at 412 nm, for Alexa647 is $\epsilon = 270,000$ M^{-1} cm^{-1} at 650 nm, for ACDAN is $\epsilon = 18,400$ M^{-1} cm^{-1} at 360 nm.

2.2 SCATTERING AND TURBIDITY MEASUREMENTS

Turbidity measurements were performed to monitor the protein assembly in solution during the LLPS processes. The increase in turbidity of a sample is due to the increase of elastic scattering in parallel to the formation of protein coacervates in the solution [68, 69].

Scattering intensity was acquired at the same wavelength used to illuminate the sample and at 90° with respect to the illumination beam to be sure that scattering light is the only contribution to the detected light. These are the same experimental conditions wherein fluorescence measurements are performed. The growth of the Rayleigh scattering peak allows to follow molecular self-assembly kinetics.

Scattering intensity may also provide information on the number and the size of the scatterer species in solution. In fact, according to Rayleigh's law, which describes the angular distribution of scattering for not absorbing spheres that are significantly smaller than the wavelength, the scattering intensity I_S is:

$$I_S \propto N \cdot V^2 \tag{2.2}$$

where N is the number of scatterers and V is the volume of each scatterer. To obtain detailed information on the size and number of scatterers more accurate analysis has to be carried out (Dynamic Light Scattering), which is however outside the aim of this thesis. Moreover, the conditions of incident wavelength greater than the object in solution is expected to be satisfied only in the early stage of protein self-assembly during the LLPS process.

Turbidity measurements were acquired using a Jasco-FP-8500 spectrofluorometer equipped with a Jasco ETC-815 peltier as temperature controller.

2.3 FLUORESCENCE SPECTROSCOPY

Fluorescence spectroscopy is a widely used technique in biophysics. Fluorescence is extremely sensitive to the modifications of the fluorophore, and this makes it a powerful tool to study many biological systems and their temporal evolution [70, 71, 72, 73]. Fluorescence may be exploited in combination with microscopy techniques, to obtain quantitative data to understand the phenomenon under investigation.

Fluorescence spectroscopy and many fluorescence microscopy techniques make use of fluorescence intensity to gather information about the composition of the sample, concentration, and molecular changes in the microenvironment. In addition

to intensity, fluorescence lifetime is another crucial feature, which depends solely on the intrinsic properties of the fluorophore. It is independent of factors such as concentration, scattering, and other mechanisms that can affect fluorescence intensity. The combined study of both features allows for a comprehensive framework of the system.

By means of specific extrinsic fluorescent probes, fluorescence may provide information about different and specific aspects of the system study. In this thesis were used three different fluorescent probes: Thioflavin T, to investigate Human Insulin amyloid-like supramolecular self-assembly, Alexa 647 to label Human Insulin and explore its dynamics, and ACDAN to study the molecular ordering and the dipolar relaxation of Bovine Serum Albumin coacervates in LLPS processes.

Fluorescence spectra in bulk were acquired using a Jasco-FP-8500 spectrofluorometer equipped with a Jasco ETC-815 peltier as temperature controller.

2.3.1 Thioflavin T

Thioflavin T (ThT) is a fluorescent dye used to study the amyloid aggregates in vitro and ex vivo. ThT was used in the context of amyloid studies for the first time in 1959 by Vassar and Culling. By means of fluorescence microscopy, they reported how ThT specifically adheres to amyloid deposits increasing fluorescence intensity and marking an important development in amyloid-specific staining techniques, highlighting the advantages of using ThT with respect to more diffuse dyes as Congo red or methyl violet, which require a complex staining protocol. Since then, the popularity of this fluorescent probe has continued to increase, eventually becoming a gold standard in the study of amyloid aggregates and their formation [74]. Figure 2.1a) shows a fluorescence microscopy image of glucagon amyloid fibrils stained with ThT, highlighting the elevated sensitivity and specificity of ThT for amyloid fibrils.

In Figure 2.1b) the molecular structure of ThT is reported. ThT is a molecule composed of three molecular moieties: 1) a benzothiazole ring, 2) a benzene ring, and 3) a dimethylamine group. These three moieties are rigid, but they can rotate along the same axes: from now on, the rotation between the first and the second group will be denoted by the angle φ, and the rotation between the second and the third group will be denoted by the angle ψ. The ThT molecule adopts a nearly planar conformation at its minimum energy state, with the energy minimum occurring at $\varphi = 37°$ and $\psi = 0°$. The angle $\varphi = 37°$ seems to arise from steric interactions between the methyl group of the benzothiazole (group I) and the hydrogen atoms of the benzene (group II) [76, 77]. The photophysical properties of ThT are predom-
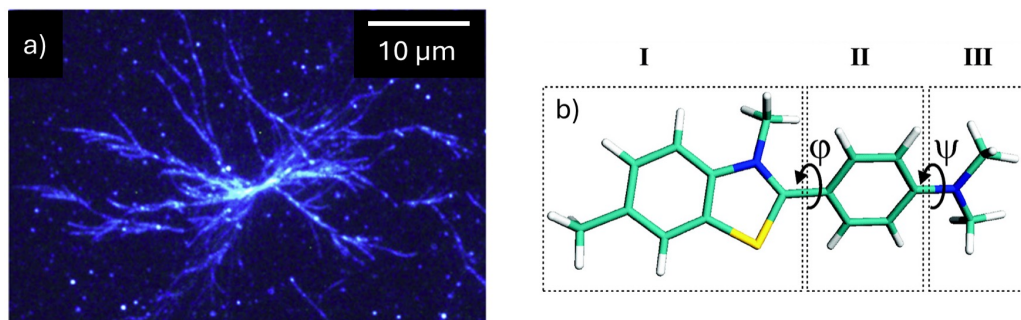
FIGURE 2.1: *a) TIRF microscopy image of branched glucagon amyloid fibrils stained by ThT [75]. Chemical structure of ThT molecule: I) benzothiazole ring, II) a benzene ring, and III) a dimethylamine group. Carbon atoms are coloured in cyan, Hydrogen in white, Nitrogen in blue and Sulphur in yellow. The three moieties can rotate with respect to each other as highlighted by the angles φ and ψ [76].*

inantly influenced by the rotation of these three moieties, and for this reason, ThT molecule is considered a molecular rotor. Moreover, it has been demonstrated that the more crucial of the two rotations for explaining the photophysical properties of ThT is the one defined by φ, as the energy barrier to rotate the dimethylamine group is much higher.
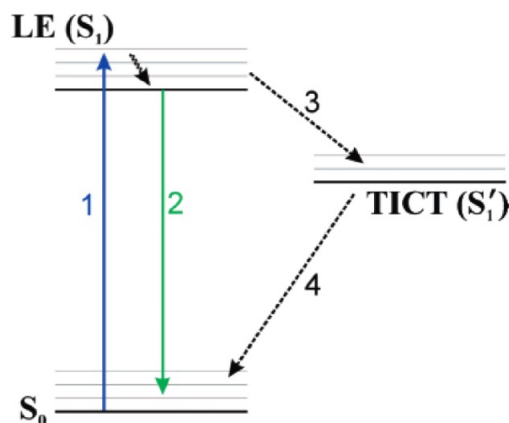

FIGURE 2.2: *Jablonski Diagram for Thioflavin T molecule: upon excitation, ThT transitions from the planar ground state S_0 to the planar locally excited (LE) state S_1. From the LE state, ThT can follow either a radiative or a non-radiative pathway. If the φ rotation is allowed, a charge transfer occurs in ThT, resulting in a change of ThT conformation to the twisted internal charge-transfer (TICT) state, which is non-fluorescent, and the molecule returns to the ground state through internal conversion. If the rotation is forbidden, ThT emits a photon through fluorescence and returns to the ground state S_0 from the LE state [76].*

The molecular functioning of ThT is reported in Figure 2.2. Upon excitation, ThT goes from the planar ground state S_0 to the planar locally excited (LE) state S_1. Following a charge transfer, which causes a φ rotation, ThT conformation changes from the LE state to a T-state known as the Twisted Internal Charge-Transfer (TICT) state. The TICT state is non-fluorescent and the ThT molecule returns to the ground

state S_0 through internal conversion. If the rotation is hindered by the environment, the charge transfer cannot occur and therefore ThT cannot transition to the TICT state. This results in an increase of ThT quantum yield and in the emission of a photon through fluorescence process [76].

Thus, this mechanism highlights how molecular rotors are sensitive to the viscosity of the environment. In fact, in a low-viscosity environment (i.e., water) the transition from the LE state to the TICT is possible and ThT does not fluoresce, since the absorbed energy is dissipated through the rotation of the moieties. Contrarily, when ThT experiences a rigid environment, such as amyloid structures, the rotation is hindered, and the molecule can return to the ground state preferentially emitting a photon since the rate of the non-radiative pathways is strongly decreased [76].

The binding of ThT on amyloid structures was extensively investigated. It was observed how ThT binds to amyloid fibrils formed from different proteins, regardless of the specific amino acid sequences, secondary structure, and/or tridimensional organization of the examined native proteins. On the other hand, the quantum yield of ThT can vary significantly depending on the morphology of the amyloid [78]. Moreover, a slight increase of ThT fluorescence is observed in presence of proteins with a large amount of β-sheets structure. All these observations combined with the notion that amyloid structures are exclusively formed by β-strands, lead to the conclusion that ThT recognizes a structural feature common among fibrils. The most widely accepted model for the ThT binding sites of amyloid structure is the so-called "channel model", shown in Figure 2.3. ThT binds on the β-strand surface, formed by the β-sheets stacking [74]. Specifically, the side chain of the residues which form the β-strands creates a channel wherein the ThT places. This channel is parallel to the axis of the fibrils and is exposed to the solvent, allowing ThT to enter. For ThT to bind, the channel must consist of at least 5 consecutive β-sheets. [74, 79].

For these reasons, ThT is highly sensitive to differences in the β-structure within amyloid aggregates [80], allowing to investigate it by exploiting its spectroscopic properties.

Naiki et al. [81] and Levine III [82] were among the first who characterized the absorption and fluorescence spectra of ThT upon binding to amyloid. Nowadays, since ThT is considered a gold standard in amyloid studies, ThT spectroscopic properties was extensively studied: Figure 2.4a) report the differences between fluorescence and absorption (in the inset) spectra of bound (in red) and unbound (in blue) ThT. Upon binding the quantum yield of ThT increase dramatically and its absorp-
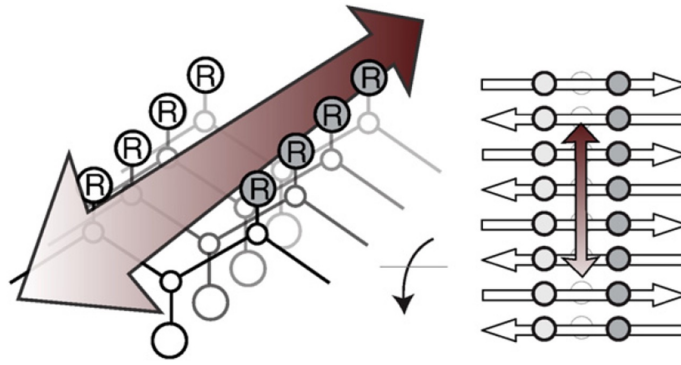
19

Figure 2.3: *Channel binding model of ThT to amyloid structures. ThT binds along the axis of the fibrils into the channel formed by the side chain of the residues which form the β-strands on the β-sheets surface [74].*

tion spectrum is red-shifted, as shown in Figure 2.4a). In Figure 2.4b) time-resolved fluorescence measurements are shown: the fluorescence decay of bound ThT is reported in red, the fluorescence decay of unbound ThT is reported in blue and the instrumental response function is reported in black. ThT in water has a very short fluorescence lifetime in the picosecond range (1-10 ps) [77, 83], and therefore is very difficult to detect. For instance, in Figure 2.4b) it is overlapped with the instrumental response function which in this experimental setup corresponds to 100 ps decay. Contrarily when ThT is bound to an amyloid structure, its fluorescence lifetime strongly increases to the nanosecond scale with average lifetime which ranges from 1 ns to 2 ns [24, 28, 77, 84, 85].
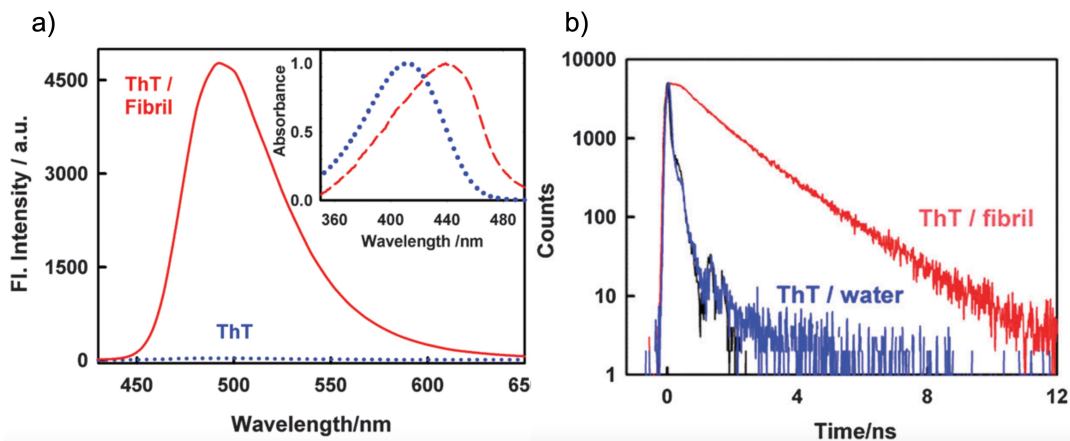

Figure 2.4: *Spectroscopic properties of ThT in presence of amyloid fibrils (shown in red) and in water (shown in blue). a) fluorescence spectra of ThT: ThT quantum yield dramatically increase in presence of amyloid fibrils. In the inset, the absorption spectra of ThT are shown. The absorption spectrum of bound ThT is red-shifted with respect to the absorption spectrum of unbound ThT. b) The fluorescence lifetime of bound ThT is longer than the lifetime of unbound ThT, which is almost overlapped with the instrumental response function (shown in black). Figure adapted from [84]*

The fluorescence decay of bound ThT is not a single exponential decay and the

most common model used to fit the data is a double exponential decay [77, 85]. This model is supported by the analysis of ThT lifetime by means of the phasor approach (see below for details) [24, 28, 86, 87, 88]. By means of this analysis method it was possible to determine the two single-exponential components: the short lifetime component ranges from 0.4 ns to 0.7 ns and the long lifetime component ranges from 2.4 ns to 2.7 ns. The short lifetime component is associated with non-specific binding sites in amyloid structures, which exhibit greater flexibility. Thus, it is linked to the overall protein density within the aggregate and the overall viscosity of the environment. On the contrary, the long lifetime component is attributed to highly specific binding sites of the amyloid structures, characterized by the specific arrangement of the β-strand architecture. Tightly packed β-sheets in amyloid fibrils results in longer ThT lifetime.

The combination of high specificity for amyloid structures, its sensibility, and the fact that the fluorescence contribution from unbound ThT is basically zero, makes ThT a perfect probe to investigate amyloid aggregates.

2.3.2 ACDAN

ACDAN (6-acetyl-2-dimethylamino naphthalene) is a fluorophore from the DAN family, synthesized by Gregorio Weber in the late '70s and introduced for the first time together with PRODAN and LAURDAN, in an important paper in 1979 [89]. In this paper, these dyes were reported to be useful tools to study the nanosecond relaxation processes in biological systems.
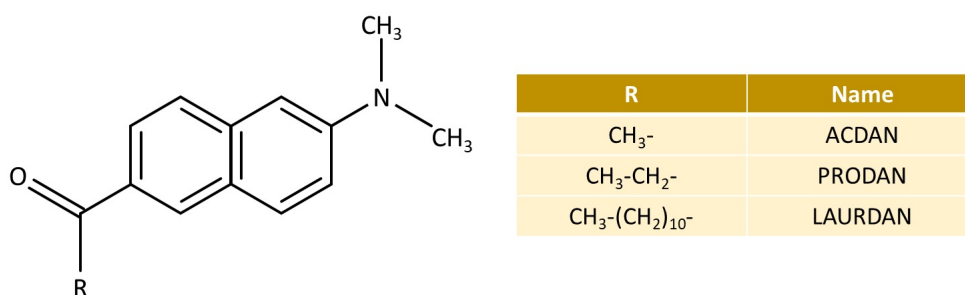

R	Name
CH$_3$-	ACDAN
CH$_3$-CH$_2$-	PRODAN
CH$_3$-(CH$_2$)$_{10}$-	LAURDAN

Figure 2.5: *Chemical structure of ACDAN, PRODAN and LAURDAN. The common structure is the naphthalene moiety, modified on the 2,6 ring positions with an amine group (electron donor) and a carbonyl group (electron acceptor), which generate dipole moments. They differ by the R group, as shown in the table. ACDAN is the most hydrophilic, having the modified naphthalene moiety linked to a methyl group, and LAURDAN is the most hydrophobic, presenting a lipid tail (chain of lauric fatty acid). PRODAN stands in between the two with an ethyl group.*

Figure 2.5 shows the chemical structure of ACDAN, PRODAN and LAURDAN. These three dyes have a naphthalene moiety modified on the 2,6 ring positions with

21

an electron donor group (the amine) and an electron acceptor group (the carbonyl group), which generate a dipole moment. The difference between ACDAN, PRODAN and LAURDAN is in the terminal R-group next to the carbonyl group, as shown by the table in Figure 2.5. In the ACDAN molecule the modified naphthalene moiety is linked to a methyl group, in PRODAN it is linked to an ethyl group, while in LAURDAN it is linked to a lipid tail, specifically the chain of lauric fatty acid. Due to the different R-groups, ACDAN, PRODAN and LAURDAN have different chemical properties and in particular different hydrophilicity/hydrophobicity: among them, ACDAN is most hydrophilic, while LAURDAN is the most hydrophobic, and PRODAN stands in between the two. For this reason, these three dyes can be used to study different systems yet providing similar information about the solvent dipolar relaxation that translates into specificity, depending on the system. LAURDAN partitions exclusively to membranes, inserting between lipid molecules and more in general in hydrophobic environments, PRODAN is found in both membranes and water (hydrophobic and hydrophilic domains) and ACDAN exhibits the greatest preference for aqueous phases with negligible partition to hydrophobic environments.

Since their introduction in 1979, LAURDAN and PRODAN have been extensively used for the study of various systems [90], while before 2015 ACDAN was used in very few papers. Among them, one paper in 1995 investigates the effect of ethanol-induced lipid interdigitation on the solubility of ACDAN, PRODAN and LAURDAN in dipalmitoylphosphatidylcholine (DPPC) membranes [91]. In 2015 PRODAN and ACDAN were proposed as tools to measure water dipolar relaxation in highly crowded environments, such as the cell cytosol, providing information on the dynamics of water molecules within crowded environments, similar to LAURDAN in membrane studies [92]. In particular, employing PRODAN and ACDAN, the authors were able to monitor the metabolic oscillation of the glycolysis process. In suspensions of Saccharomyces cerevisiae, a species of yeast, they observed that the fluorescence oscillation of the DAN dyes has the same frequency as the metabolic oscillation of NADH and ATP. This coupled with additional experiments on model crowded systems, supports the idea that the DAN fluorescence oscillations arise from periodic changes in the dipolar (rotational) relaxation of water, and not from further interactions with other suspension components. Therefore, the metabolic processes influence and are influenced by the physical properties of the intracellular environment, highlighting the role of water in the entire process.

ACDAN spectroscopic properties were recently used to study in vivo the development of macromolecular crowding in the ocular lens of a zebrafish [94]. Authors
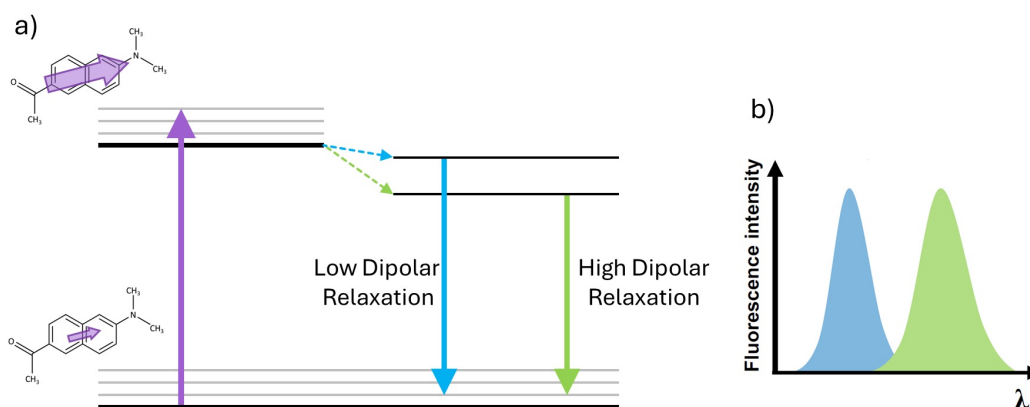
Figure 2.6: *a) Simplified Jablonski diagram for ACDAN: the absorption transition between the ground state and the excited state is shown by a purple arrow. b) Figurative sketches of the ACDAN fluorescence spectra [93]. In the excited state, ACDAN has a higher dipole moment with respect to the ground state, which reorganizes the dipoles in solution, leading to their dipolar relaxation. The dipolar relaxation lowers the energy of the ACDAN excited state. When the dipolar relaxation is low (cyan arrow), the energy lost by ACDAN is low and the fluorescence spectrum is blue-shifted, while when the dipolar relaxation is high (green arrow), ACDAN loses more energy and the fluorescence spectrum is red-shifted.*

observed that ACDAN is sensitive to macromolecular crowding both in vitro and in vivo, validating its utility as a nano-environmental sensor for measuring water dynamics. Dipolar relaxation is in fact responsive to macromolecular crowding because of ACDAN sensitivity to the water molecules hindered mobility and to their number with respect to the solute concentration. From a spectroscopic point of view, the increase of the macromolecular crowding translates in a spectral blue-shifted of the ACDAN fluorescence spectrum.

To better explain the action mechanism of ACDAN dye, a simplified Jablonski diagram for the probe is reported in Figure 2.6a) and the sketches of two figurative ACDAN fluorescence spectra are shown in Figure 2.6b). In the ground state, ACDAN molecules present a dipole moment, due to the presence of the carbonyl and amine group linked to the naphthalene moiety. As usual for many dyes, ACDAN dipole moment increases when the molecule is excited following an absorption transition, shown as a purple arrow in Figure 2.6a). The higher electric field, resulting from the increase of the dipole moment in the excited state, may reorganize solvent dipoles or more in general, other dipoles present in the solution. Specifically, this results in the orientation of the solvent dipoles in the same direction as the fluorophore dipole, leading to the solvent dipolar relaxation. The dipolar relaxation lowers the energy of the excited state and shifts the fluorescence spectrum to longer wavelengths. If the rotational degree of freedom of the solvent molecules is higher, the solvent dipoles can reorient in the same direction as the fluorophore dipole, and

so it is solvent dipolar relaxation (green arrow in Figure 2.6). This results in the red-shift of ACDAN fluorescence spectrum, as shown in Figure 2.6b). On the contrary, a hindered rotation translates into a lower reorganization of the dipoles and solvent low dipolar relaxation (shown as a cyan arrow), and the ACDAN fluorescence spectrum blue-shifts.

To quantify ACDAN spectral shift Generalized Polarization (GP) is commonly used. GP is a spectroscopic parameter in the 1990 [95] by Parassi and Gratton for LAURDAN fluorescence to reveal phase fluctuation in phospholipid membranes and is now used for all DAN probes. GP is defined as:

$$GP = \frac{I_B - I_R}{I_B + I_R} \tag{2.3}$$

where I_B and I_R are the fluorescence intensity measured respectively at a chosen short (blue) and long (red) wavelength (or band of wavelengths) of the fluorescence spectrum. GP is a weighted difference, therefore its value ranges from -1 to +1, the lower the value the greater the extent of dipolar relaxation. In studies using AC-DAN, it is possible to exploit GP to distinguish between the two different "states" of the solvent: relaxed (freer to rotate and more disordered) and unrelaxed (less free and more ordered). This is of course a simplified description which has to be used taking into account the specificity of the system in analysis.

ACDAN is used to investigate the molecular ordering of a physical phase, by the dynamics of the water dipoles in solution [92, 93, 94, 96, 97]. Molecular crowding implies the high concentration of macromolecules and high excluded volume effects. This translates to a lesser amount of bulk water and more water "bound" to the hydration shell of the macromolecules (both crowding agents and protein). Numerous experimental and theoretical studies have confirmed that the mobility of water molecules is significantly decreased near other molecules [98, 99]. In this regard, it is possible to correlate the macromolecular crowding to the reduced dynamic of water molecules [94]. Indeed, from a thermodynamical point of view, in an ordered phase the water diffusion is reduced, and the hydrogen bonds are more stable in clathrate-like structures. This is expected to reduce the solvent dipolar relaxation since the dipoles are less able to move and orient towards the electric field. On the contrary, in a disordered phase, the hydrogen bonding is less stable, allowing for a higher dynamic of the dipoles in the solution, resulting in higher dipolar relaxation.

The solvent dipolar relaxation is more pronounced when the probe experiences a solvent with a higher polarity [72]. From a microscopic point of view, a polar solvent has a high dielectric constant and therefore the single dipoles, which constitute

the solvent, have a higher dipole moment, so in this regard, ACDAN is also a sensor for the solvent polarity.

In particular, when the fluorescent probe experiences a more polar solution the fluorescence spectrum is red-shifted, while in a less polar solution, the fluorescence spectrum is blue-shifted. Despite the solvent polarity and its dipolar relaxation are linked, being two faces of the same coin, in solution containing other compounds, the link between these two concepts is not always so simple. The polarity of the overall solution and the solvent dipolar relaxation depends on the solution condition, which may modify the viscosity and other physico-chemical properties of the solution. For instance, simply the addition of solute may increase or decrease the viscosity of the solution, shielding charges, etc.

ACDAN being highly hydrophilic presents a high quantum yield in aqueous media with respect to other dyes sensitive to dipolar relaxation and polarity, such as the already mentioned LAURDAN, or for instance, Nile Red and 8-anilinonaphthalene-1-sulfonic acid (ANS), which are poorly soluble in water.

2.4 Fluorescence microscopy

Fluorescence microscopy is a widely used technique to visualize and analyse in real-time and with spatial resolution many biophysical phenomena on the nano, and microscale, such as the protein supramolecular assembles. The coupling of optical microscopy with fluorescence allows to exploit the high sensibility and specificity of the fluorescence as contrast method. Fluorescence microscopy was extensively used for the acquisition of measurements reported in this thesis. Details of each technique will be reported below.

2.4.1 Spatial resolution

The spatial resolution is one of the most important characteristics of a microscope. It is the minimum distance measured between two objects in the image such that they can be distinguished as separate objects [100]. In the 19th century, the German physicist and astronomer Ernst Abbe theorized that the resolution limit for an optical microscope is imposed by diffraction of light, and he defined an expression that has become a fundamental law for the development of optical microscopy [100, 101]:

$$\Delta x = \frac{\lambda}{2 \cdot NA} \tag{2.4}$$

25

where Δx is the minimum distance (or resolution limit) between two points in the image, λ is the wavelength collected by the microscope objective and NA is the numerical aperture of the used objective, and it is defined as:

$$NA = n \sin \theta \qquad (2.5)$$

with n being the refractive index of the surrounding medium and θ being half of the angle of the aperture of the objective. The numerical aperture NA describes the ability of a convex lens to collect light: a high numerical aperture allows it to gather more light, resulting in a stronger signal, and since it can capture more refracted rays, it thus enhances the resolution. Thus, the resolution limit depends on the geometrical characteristic of the objective and on the nature of the light collected by the objective. The spatial resolution for a fluorescence microscope is about 200 nm. For instance, one of the most used objectives for acquiring measurements reported in this thesis is a 63×/1.40-0.60 oil objective, where 63× is the maximum magnification, 1.40 is the numerical aperture and 0.60 is the iris diaphragm. The resolution limit for such an objective, collecting 550 nm light, is about 196 nm.

The image of an object through an optical instrument is the collection of image points formed by the interference of light which comes from every source point of the object [100, 101]. Each image point is actually a diffraction figure called an Airy disk, which is simply a diffraction pattern with a cylindric symmetry, shown in Figure 2.7.
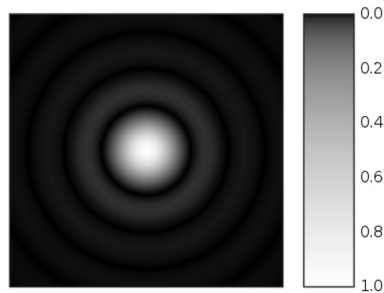

FIGURE 2.7: *Representation of the Airy disk. It is a diffraction pattern with cylindrical symmetry: the light intensity is highest at the centre and decreases in the radial direction. The central peak is surrounded by concentric rings with lower intensity.*

The bi-dimensional image of an object is the convolution of the real object and the Airy disk [101]. The size of the Airy disk is related to the wavelength of the radiation and the numerical aperture NA and in particular the radius of the first maximum (r_{Airy}) is determined by the equation:

$$r_{Airy} = 0.61 \frac{\lambda}{NA} \qquad (2.6)$$

When an object is smaller than the resolving power of the instrument, its image will consist of an Airy disk. In an image, two points are distinguishable if the diffraction figures that constitute their images are also distinguishable, that is when the central maxima of the Airy disks are at a distance greater than their width. Contrarily if the central maxima of the Airy disks are overlapped, the points are not distinguishable. The size of the Airy disk sets therefore an upper limit for the resolution of an optical instrument [100, 101], which can be quantified by the following expression:

$$\Delta x_{min} \geq 0.61 \frac{\lambda}{NA} \tag{2.7}$$

where Δx_{min} is the resolution limit of the microscope. This expression is the Rayleigh limit and according to it, two adjacent points are resolved if the centre of the Airy disk of the first point lies at the same position as the first minimum of the Airy disk associated with the second point [101], as shown in Figure 2.8.
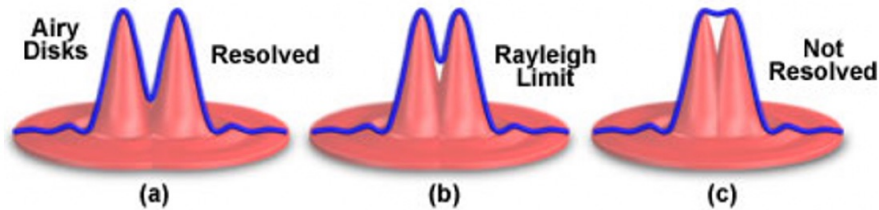

FIGURE 2.8: *Graphical representation of the Rayleigh limit. a) Two adjacent points are resolved if the distance between them is higher than the radius of the Airy disk. b) The Rayleigh limit is satisfied when the distance between the points and the size of the Airy disk size is the same. c) Below that limit the two points are not resolved anymore. [https://www.olympus-lifescience.com/es/microscope-resource/primer/digitalimaging/deconvolution/deconresolution/].*

Everything described so far applies to two dimensions but can be easily extended to three dimensions: the image of a point source through an optical system is a three-dimensional diffraction figure called the Point Spread Function (PSF). In the absence of aberrations in an aligned system, PSF describes a rotational ellipsoid whose dimensions depend on the wavelength of the radiation conveyed by the lens and the numerical aperture of the lens. Thus, the Airy disk is the projection of the PSF onto the focal plane of the lens of the optical system. The image of an object is the convolution of the real shape of the object with the PSF. Similarly to the Airy disk, the extension of the PSF in three dimensions constitutes the resolution limit along the three dimensions [100]. Therefore, analogous to the definition of lateral resolution Δx_{min}, it is possible to define an axial resolution Δz_{min} using the following expression:

$$\Delta z_{min} = 1.67 \, \frac{n \cdot \lambda}{NA^2} \qquad (2.8)$$

where Δz_{min} is the position of the first diffraction minimum on the z axis.

2.5 CONFOCAL LASER SCANNING FLUORESCENCE MICROSCOPY (CLSM)

The evolution of fluorescence microscopy has led to the development of Confocal Laser scanning fluorescence microscopy (CLSM). This technique has pushed the resolution achievable by a microscope up to the theoretical limit proposed by Abbe, by optical sectioning the sample and selectively accessing the fluorescence signals from different focal planes within the sample. As a consequence, CLSM allows for generation of three-dimensional images.

In a conventional widefield fluorescence microscope, the light source is a lamp which emits a continuous spectrum, and single specific regions of the spectrum are selected through a filter. The source radiation uniformly illuminates a large portion of the sample, limited by the objective numerical aperture. At this region, the sample absorbs the radiation and emits fluorescence. The fluorescence is then collected to reconstruct the image in a single acquisition. In the image reconstruction, contributions from out-of-focus planes are included. This causes a decrease in the signal-to-noise ratio of the image and a drastic reduction in its resolution [100].

CLSM is designed to address the several limitations of traditional widefield fluorescence microscopy. The radiation source in a confocal microscope is a laser, therefore there is no need for a filter to select a specific spectral range. The radiation is diffracted by a pinhole and after going through a dichroic mirror, it is focused by the objective on the sample [100, 101]. The radiation illuminates a double optical cone with its vertex at the focal point. At this region, the radiation is absorbed by the sample and it emits fluorescence. The fluorescence is collected by the objective, and it is acquired by the photomultiplier. The greatest difference between the CLSM and the widefield microscopy is as simple as revolutionary in its effects: the presence of a second pinhole in front of a photomultiplier, which allows to shield all the contributions from the out-of-focus planes and only allowing the contribution from the focal plane to pass through. The absence of overlapping contributions from the out-of-focus planes of the sample makes the resulting image sharper. The acquired fluorescence is therefore only emitted by a small region of the sample (the vertex of the double focal cone). This localized collection results in a reduced signal, which

is basically offset by using a laser as the radiation source because it is significantly brighter than a conventional lamp. Additionally, since the signal originates from a small illumination volume within the sample, reconstructing an image of the sample requires multiple acquisitions from different points of the sample, by scanning the sample and capturing photons emitted from each point. For this reason, confocal microscopy is defined as a scanning microscopy technique [100].

Another advantage of CLSM over widefield microscopy, also due to the small volume of illumination, is the ability to perform optical sectioning of the sample by acquiring images at different depths along the z-axis. This allows for the reconstruction of a three-dimensional model of the sample. By means of CLSM it is also possible to acquire spectral (x, y, λ) or temporal (x, y, t) information for each pixel of the image, enabling the discrimination of different species or studying the progression of evolving processes over time [100].

The experiments were performed using a Leica TCS SP5 confocal laser scanning microscope, with a 63×/1.40-0.60 and 40×/1.25-0.75 oil objective, and a scanning frequency 400 Hz (Leica Microsystems, Germany). The laser source is Leica Supercontinuum White Light Laser (WLL). The analysis of the microscopy data was performed by the open-source software ImageJ Fiji (https://imagej.net/software/fiji/).

2.6   FLUORESCENCE RECOVERY AFTER PHOTOBLEACHING (FRAP)

Fluorescence Recovery After Photobleaching (FRAP) is a microscopy technique used to obtain information on the dynamics and mobility of the fluorescent molecules in a system. If the molecular species under analysis are not fluorescent, the studied molecules can also be labelled with a fluorescent probe. FRAP is based on a phenomenon which is usually avoided in any fluorescence-based technique: photobleaching [102]. Photobleaching is the irreversible loss of fluorescence by a molecule, due to prolonged exposure to high-intensity light. This loss of fluorescence is caused by photochemical alterations of the fluorophore itself or of its surroundings, which prevents it from emitting light [102].

In a FRAP experiment (see Figure 2.9 as reference), a region of interest within the sample is photobleached using a high-intensity laser beam. Following the photobleaching process, it is possible to observe a fluorescence recovery This recovery occurs as unbleached fluorescent molecules from surrounding areas diffuse into the bleached region and as photobleached molecules within the bleached zone diffuse out of the bleached region. The recovery of fluorescence is therefore monitored over time by capturing images at set intervals. Thus, the recovery rate provides in-

formation on the molecular diffusion and mobility of the fluorescent species within the sample, which are also indicative of the viscosity of the sample environment.

After enough time the equilibrium is reached, and the fluorescence recovery arrives at the plateau. In general, the fluorescence does not reach its initial value and the difference between the final and the initial fluorescence value denotes the percentage of the immobile fraction within the region of interest.
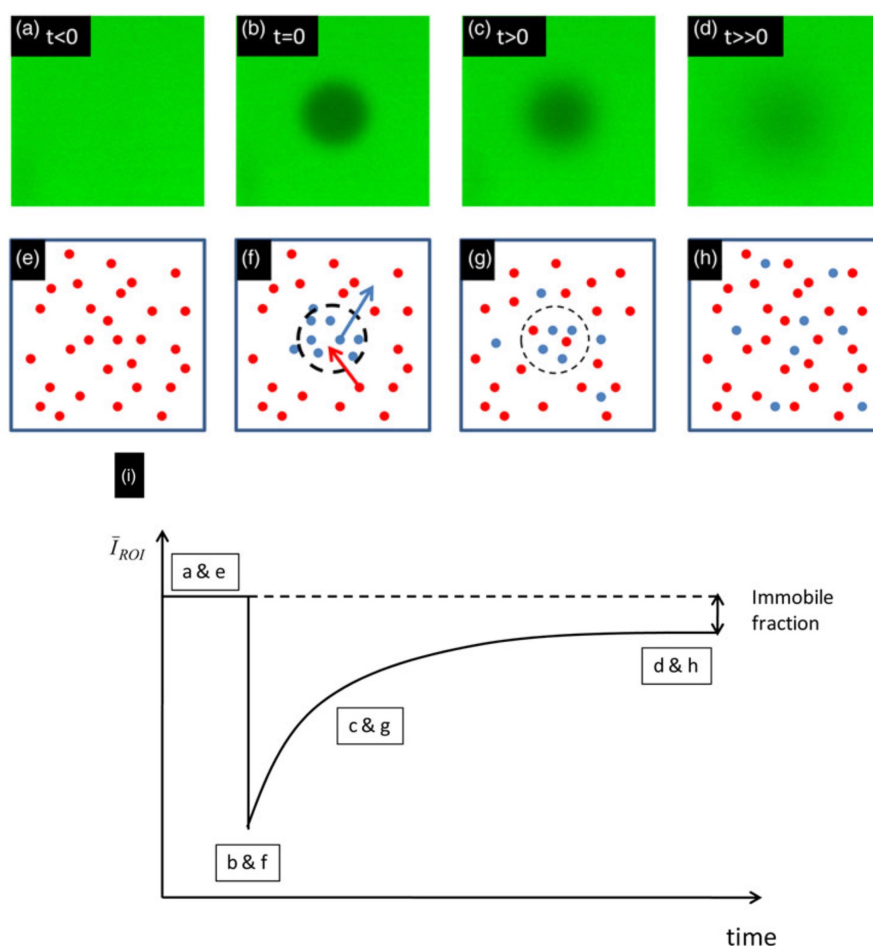

FIGURE 2.9: *FRAP experiment: a-d) Fluorescence microscopy images of the sample during different phases of a FRAP experiment and e-h) illustration of the same process at the molecular level. a), e) fluorescence of the sample before the photobleaching (t < 0); b), f) the sample is photobleached in a region of interest (t = 0); c), g) fluorescence recovery in the region of interest after photobleaching due the diffusion of the bleached molecules out of the bleached region and the unbleached molecules in the bleached region.; d), h) the equilibrium is reached and the fluorescence recovery stops. i) profile of fluorescence recovery: the difference between the final and initial value provides the percentage of the immobile fraction of the sample. Figure adapted from [103]*

In this thesis FRAP was used to investigate the mobility of Human Insulin molecules labelled with Alexa 647 within different regions of Insulin coacervates.

FRAP experiments were performed using FRAP wizard of the Leica TCS SP5 confocal laser scanning microscope control software and WLL as an excitation/bleaching

source. The 256 × 256 pixels images were acquired with a 63×/1.4 oil objective, and scanning frequency 400 Hz. The analysis of the microscopy data was performed by the open-source software ImageJ Fiji (https://imagej.net/software/fiji/).

2.7 Two-Photon Excitation process

The Two-photon excitation (2PE) process, or more in general the multi-photon excitation (MPE) process, is a nonlinear optical process that involves the simultaneous absorption of two or more photons by a fluorophore. From the excited state, photons are then emitted through fluorescence with higher energy than the absorbed photons.

This phenomenon was first theorized by Maria Göppert-Mayer in 1931 in her PhD thesis, while the first experimental observation of a two-photon excitation process occurred in 1961 by Wolfgang Kaiser and C. G. B. Garrett in a CaF2:Eu2+ crystal [100].
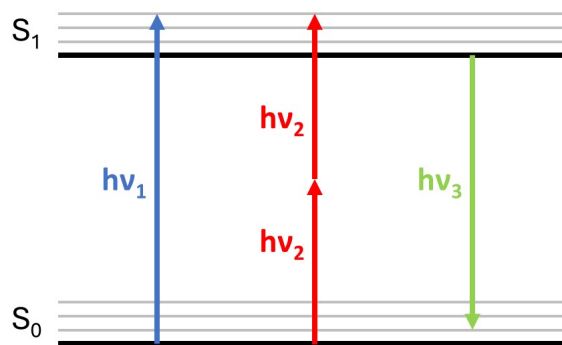

FIGURE 2.10: *Simplified Jablonski diagram showing a single-photon excitation process (in blue) and a two-photon excitation process (in red). On the right, the fluorescence process is reported in green.*

Figure 2.10 displays the Jablonski diagram of a system with two energy levels: S_0 is the ground singlet state, and S_1 is the first excited singlet state. The electronic levels are illustrated by thick black lines, while the vibrational states are shown as grey lines. The blue arrow represents a linear single-photon absorption transition from the S_0 state to the S_1 state. For a photon to induce this transition between S_0 and S_1, the photon's energy must match the energy difference between these two levels. The red arrows represent the transition from the ground state to the excited state via a two-photon excitation process. This transition occurs when the combined energies of two photons, which are absorbed simultaneously by the same system, equal the energy required for the transition in the case of single-photon absorption [72]. Therefore, the energy of a single photon is half of the energy needed for

the transition to occur. In principle, the photons absorbed during a two-photon excitation may be different since the important factor is the sum of the energies. However, from an experimental point of view, a fluorophore is always excited by a laser source, which emits coherent photons at the same energy, so the energies of the photon used for a two-photon excitation are always the same [72].

The fluorescence process is depicted by a green arrow. This illustrates how fluorescence is independent of the type of absorption transition, whether it is linear (single-photon) or two-photon. The fluorescence occurs regardless of how the excitation was achieved and the emitted radiation exhibits the same properties in terms of the shape of the emission spectrum and lifetimes [72].

In the case of a linear excitation, the transition probability depends linearly on the intensity of the incident radiation, therefore each point of the sample which is illuminated (even in the non-focal planes) has a non-zero probability of absorbing a photon and consequently emitting another one. Instead, the transition probability for a 2PE process depends on the square of the radiation intensity. This, coupled with the fact that 2PE processes have a cross-section several orders of magnitude smaller than the cross-section of linear processes, ensures that the absorption and subsequent fluorescence occur only at the focal point of the objective (where the intensity of the laser beam is maximized), and drop to zero almost immediately as one moves away from the focal point. Therefore, for 2PE to occur, it is necessary that the excitation beam incident on the sample has a high photon flux and that it is confined both spatially and temporally [72].

From a practical point of view, these experimental conditions are achieved using pulsed lasers as radiation source. Typically, the laser frequency is between 80 and 100 MHz and the maximum power of each pulse is about 100 kW and their duration is about 100 fs [104].

2.8   TWO-PHOTON MICROSCOPY (2PM)

Two-photon Microscopy (2PM) is a fluorescence microscopy technique where the fluorescence is obtained by 2PE of the sample. Similarly to CLSM, 2PM is also a scanning microscopy technique. In both techniques, the radiation is focused on a specific point of the sample, and therefore multiple acquisitions are needed to reconstruct a single image. This also results in the acquisition of images at various depths, allowing for the reconstruction of a three-dimensional model of the sample [100, 101]. As already described, in the 2PM the excitation process occurs solely at the focal plane of the objective, within a volume on the order of the femtoliter.

This results in a fundamental difference between Confocal Laser scanning fluorescence microscopy (CLSM) and 2PM: whilst in the former the optical sectioning is achieved by the presence of a pinhole in front of the detection system, which does not let the emission from the out-of-focus planes to pass through, in the 2PM it is an intrinsic property of the excitation process. Thus, the pinhole loses its function, and if present, must be completely open.

As already mentioned, the 2PE is experimentally achieved using an infrared (IR) pulsed laser source. Typically, the laser source used is a titanium-sapphire laser (Ti:Sa) which may be tuned to emit radiation between 700 nm and 1050 nm [101]. Illuminating the sample with IR radiation offers the important advantage of performing less invasive measurements. IR radiation is in fact less energetic than UV radiation and for this reason, it is ideal for biological samples which are often prone to photo-degradation processes which may cause the deterioration of the whole sample. Examples include photo-oxidation and photobleaching which are phenomena often observed in samples irradiated by high energy radiation as UV light [105]. Moreover, even if the power of the single pulse is quite high, the average energy deposited on the sample is critically lower compared to using a continuous-wave laser. The radiation-matter interactions for IR radiation are lower than the interactions for UV and visible light. In fact, in any medium, longer wavelength radiation is less scattered, as demonstrated by the fact that Rayleigh scattering intensity depends on the radiation wavelength as (λ-4). This results in higher penetration into the sample and in the reduction of unwanted scattering contributions.

In this thesis, two-photon excitation is used to measure the fluorescence emitted by ThT and ACDAN, since it enables the UV excitation of the dyes, reducing the scattering contribution which is higher in confocal microscopy.

The experiments were performed using a Leica TCS SP5 confocal laser scanning microscope, with a 63×/1.40-0.60 and 40×/1.25-0.75 oil objective, and a scanning frequency 400 Hz (Leica Microsystems, Germany). The laser source is a Spectra-Physics Mai-Tai Ti:Sa ultra-fast laser. The analysis of the microscopy data was performed by the open-source software ImageJ Fiji (https://imagej.net/software/fiji/).

2.9 Fluorescence Lifetime Imaging Microscopy (FLIM)

Fluorescence lifetime imaging microscopy (FLIM) is a microscopy technique where the contrast of an image is not provided by the fluorescence intensity as it is usual, but by its lifetime. A FLIM measurement contains information about the fluorescence decay of the molecular species in each pixel of the image. Two methods

exist to measure the fluorescence lifetime: the time domain and the frequency domain. The measurements reported in this thesis were acquired using the time domain methods and therefore only the time domain will be explained in this chapter. The time domain method is based on the Time-Correlated Single-Photon Counting (TCSPC) method [72]. Using a pulsed laser source, the detector measures one fluorescence photon for each pulse of the laser and measures the acquisition delay with respect to the laser pulse. This results in a histogram of the detected photon distribution over time [72].

The measured decay profile is influenced by the Instrumental Response Function (IRF), which collects the effect due to the excitation source, the response of the detector, and the electronic components [106]. The IRF represent the lower detection limit of a FLIM system because it is the fastest signal that the system can detect [106]. Since the measured signal is the convolution of the real fluorescence decay and the IRF, this also implies that shorter lifetimes are more strongly affected by the IRF than longer decays.

FLIM measurements were acquired in the time domain by means of a Leica TCS SP5 confocal laser scanning microscope coupled with picoHarp 300 TCSPC module (Picoquant, Germany). 256 × 256 pixels FLIM images were collected with a 63×/1.4 oil objective and scanning frequency 400 Hz. The laser source are Leica Supercontinuum White Light Laser (WLL) and Spectra-Physics Mai-Tai Ti:Sa ultrafast laser.

2.9.1 PHASOR APPROACH TO ANALYSE FLIM DATA

In 2008 a new method for the analysis of FLIM data was introduced by Michelle Digman and Enrico Gratton [107] to overcome the difficulties which arise from the fit-based analysis of complex fluorescence decays. This method is based on the Fourier transform of fluorescence lifetime decay and it is called Phasor approach. The phasor approach implies a graphical representation of the fluorescence lifetime decays, allowing the visualisation of the lifetime distributions in a polar plot, known as phasor plot. Through the Fourier transform, each fluorescence decay $I(t)$ is mapped to a point (phasor) in the phasor plot. The coordinates of the phasor correspond to the real part and the imaginary part of the Fourier transform $\tilde{I}(\omega)$ of decay $I(t)$:

$$\tilde{I}(\omega) = \int_{-\infty}^{+\infty} I(t)e^{i\omega t}dt \qquad (2.9)$$

where ω is the laser frequency [107, 108]. By rewriting the complex exponential using trigonometric functions, it is possible to get the real and imaginary parts of the function $\tilde{I}(\omega)$. The real part, $g(\omega)$, represents the x-axis on the phasor plot, while the imaginary part, $s(\omega)$, represents the y-axis:

$$g(\omega) = \frac{\int_{-\infty}^{+\infty} I(t)\cos(\omega t)dt}{\int_0^{+\infty} I(t)dt} \tag{2.10}$$

$$s(\omega) = \frac{\int_{-\infty}^{+\infty} I(t)\sin(\omega t)dt}{\int_0^{+\infty} I(t)dt} \tag{2.11}$$

where the integral in the denominator serves as a normalization factor for $g(\omega)$ and $s(\omega)$ [108]. By solving the previous integral, the following expressions for $g(\omega)$ and $s(\omega)$ are derived:

$$g(\omega) = \sum_{i=1}^{N} \frac{f_i}{1 + \omega^2\tau_i^2} \tag{2.12}$$

$$s(\omega) = \sum_{i=1}^{N} \frac{f_i\omega\tau_i}{1 + \omega^2\tau_i^2} \tag{2.13}$$

where the summation runs over all components of the exponential decay, τ_i is the lifetime of the i-th component, and f_i is the weight of the i-th component. The weight f_i is defined as follows:

$$f_i = \frac{\alpha_i\tau_i}{\sum_{j=1}^{N} \alpha_j\tau_j} \tag{2.14}$$

The α_i terms in the previous expression are the weight of the single components of the multi-exponential decay. The sum of all f_i is normalized to one.

In cases where the decay has only one component, the expressions for $g(\omega)$ and $s(\omega)$ simplify as follows:

$$g(\omega) = \frac{1}{1 + \omega^2\tau^2} \tag{2.15}$$

$$s(\omega) = \frac{\omega\tau}{1 + \omega^2\tau^2} \tag{2.16}$$

By combining the previous equations for $g(\omega)$ and $s(\omega)$, a simple expression for the lifetime as a function of $g(\omega)$ and $s(\omega)$ is obtained:

35

$$\tau = \frac{1}{\omega}\frac{s}{g} \tag{2.17}$$

It is worth noticing that the fluorescence lifetime τ is zero when $s = 0$ and it tends to infinity when $g = 0$. Moreover, substituting τ in the equation for $g(\omega)$ and $s(\omega)$ as the expression just found the following equation is obtained:

$$(g - 0.5)^2 + s^2 = 0.25 \tag{2.18}$$

This equation describes the "universal circle", which is the region of the phasor plot, where the phasors associated with single-exponential lifetime decays lie. It is a circumference centred at the point (0.5; 0) with a radius of 0.5. The functions for $g(\omega)$ and $s(\omega)$ are defined for values greater than zero, thus this expression is defined for the upper half of the circumference. On the universal circle, short lifetimes are mapped close to the point (1; 0) and long lifetimes near the origin (0; 0), as shown in Figure 2.11.
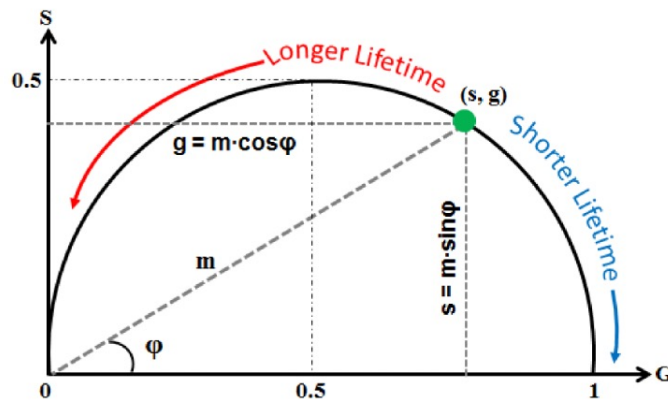

FIGURE 2.11: *The semicircumference centred in the point (0.5; 0) with a radius of 0.5 is the "universal circle", which is the region of the polar plot where the phasors associated with the single-exponential lifetime decays lie. Short lifetimes lie near the point (1; 0) and long lifetimes lie in correspondence of the origin (0; 0). Figure adapted from [108].*

Fourier transform is a linear operator, therefore the phasors are linear as well. This implies that the values of the coordinates $g(\omega)$ and $s(\omega)$ of a multi-exponential fluorescence decay may be expressed as the linear composition of the coordinates of its components which are single-exponential decay. This linear property is highlighted by the following expressions:

$$g(\omega) = \sum_{i=1}^{N} f_i g_i \qquad (2.19)$$

$$s(\omega) = \sum_{i=1}^{N} f_i s_i \qquad (2.20)$$

An important consequence of the linearity property of the phasors is that multi-component decays on the phasor plane fall within the universal circle. In particular, a two-component lifetime decay aligns with a straight line that connects the two individual lifetime components of the complex decay. Furthermore, the distance of a phasor point on the line from one of the two single components (normalized to the total length of the chord) is the weight of the other single component in the complex lifetime, and vice versa. The weights are often referred to as a fraction. See Figure 2.12 as a reference. This approach allows for the accurate identification of the components in a multi-exponential decay [107, 109]. Therefore, data itself indicates the most suitable model to use, eliminating the need to arbitrarily impose one.
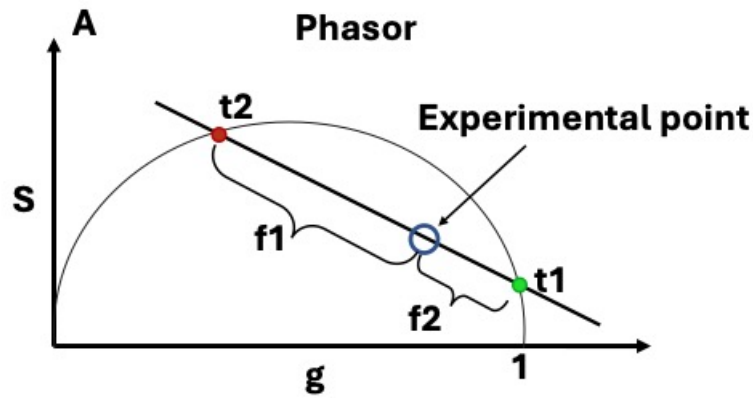

FIGURE 2.12: *Single-exponential decays lie on the universal circle, and multi-exponential decays lie within the circle. The phasor associated with a two-component decay (t1 and t2) lies on the straight line connecting the two components. The distances (f1 and f2) between the experimental point and the components are proportional to the weights of the components themselves. Figure adapted from [110].*

Experimentally, FLIM data in the phasor plot appear as clouds of points which are the fluorescence lifetime distributions. To spatially localize the fluorescence lifetime distributions obtained in the phasor plot, phasor distributions can be selected using coloured cursors. As result, all the pixels of the original image, associated with the phasors selected by the cursor, will be coloured with the same colour of the used cursor (Figure 2.13a), obtaining a new image in false colour called "phasor

map" (Figure 2.13b) [109]. For a two-components lifetime, known the two single components, it is possible to analyse the data and to obtain the map of the fraction of the first component, therefore providing overall information of the lifetime with a higher spatial resolution. The resulting image has a continuous colour code, and it is called "fraction map" [109].
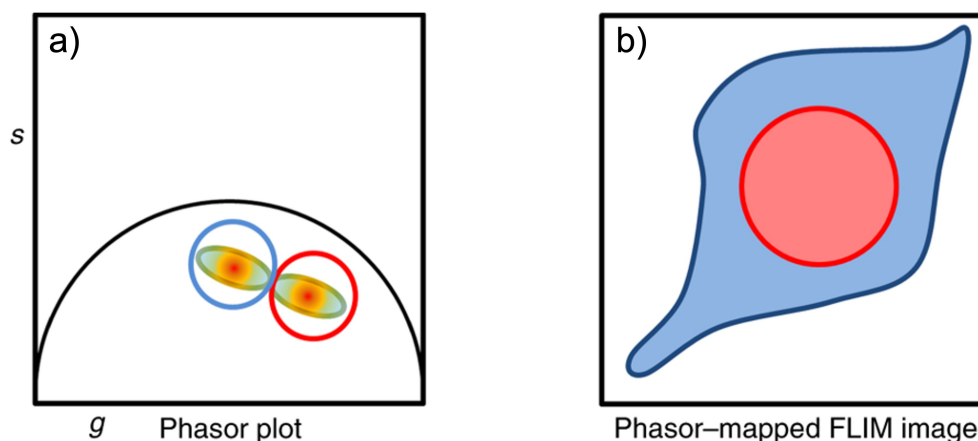

FIGURE 2.13: *Cursor analysis of FLIM data. a) Lifetime distributions may be selected by cursors with different colours. b) The pixel corresponding to the distribution selected by a cursor will be marked with the same colour as the used cursor. Figure adapted from [109].*

2.10 MODEL PROTEINS

This experimental study is carried out using model globular proteins. The use of model protein to investigate aggregation and LLPS phenomena offers several advantages in elucidating the underlying mechanisms of these complex biophysical processes. Firstly, model proteins allow for precise control over experimental conditions, including protein concentration, sequence, and post-translational modifications, facilitating systematic studies to dissect the key factors influencing aggregation and LLPS. Secondly, model proteins have a specific and well-known structure enabling easier identification of critical molecular interactions and structural features driving aggregation and LLPS. In this study Bovine Serum Albumin and Human Insulin were used.

2.10.1 BOVINE SERUM ALBUMIN

Bovin Serum Albumin (BSA) is a well-known globular protein characterized by high structural stability. Serum Albumin proteins are derived from blood serum, and they are widely utilized in various biochemical applications due to their stability.

Serum albumin proteins mainly serve as carriers for several small molecules, such as hormones, fatty acids, peptides, etc., which must be delivered within the organism. Serum Albumin proteins also play a role in the regulation of the oncotic pressure and the blood pH.

The amino acids sequence of BSA is composed of a single polypeptide chain of 583 residues, with a molecular weight of approximately 66.5 kDa. It has three homologous domains (I, II, and III), each formed by two subdomains (A and B), as shown in Figure 2.14. The organization in three domains forms its characteristic heart shape. These domains are arranged to create two hydrophobic pockets, which serve the role of binding sites for many ligands, located in the subdomains IIA and IIIA [111, 112].
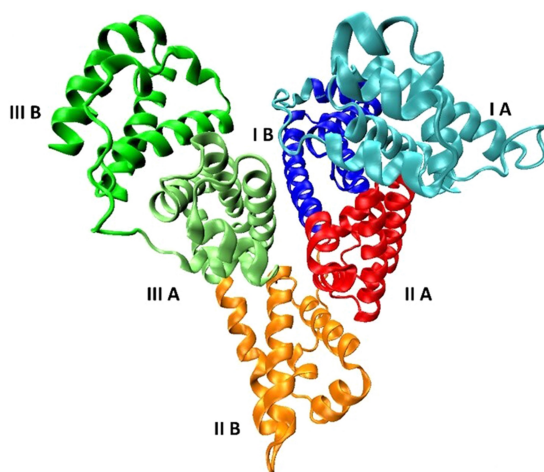

FIGURE 2.14: *BSA tridimensional conformation. BSA is organized into three domains (I, II and III) which form its characteristics heart shape. Each domain is divided into two sub domains (A and B) [113].*

BSA contains 17 disulfide bridges, which stabilize its tridimensional structure providing a degree of rigidity within each domain yet permitting considerable alterations in the BSA shape in response to solution conditions as temperature and pH fluctuations. The secondary structure of BSA consists primarily of alpha-helices and turns. It has been reported that BSA contains approximately 67% alpha-helices, which are crucial for the stability and flexibility of the entire molecule [114]. The alpha-helical content helps in maintaining the structural integrity of BSA under varying experimental conditions. From a thermodynamical point of view, the high stability of BSA translates into a high denaturation temperature of about 60°C. Its isoelectric point is about 4.5 − 5.0 indicating that in acidic pH, BSA is positively charged while at alkaline pH, it is negatively charged.

Being a transport protein, the binding ability is crucial for the function of BSA. These pockets are characterized by their nonpolar environment [115], which al-

lows hydrophobic interactions with various lipophilic compounds. The flexibility of the loop regions around these pockets allows BSA to accommodate ligands of various sizes, enhancing its binding versatility. The presence of non-specific and flexible biding sites permits BSA to easily interact with multiple molecular species. This makes BSA a useful model system to characterize how intermolecular interactions, are affected by macromolecular crowding and LLPS processes [116]. For this reason, in the recent years, many papers on the LLPS of BSA were published [53, 116, 117, 118, 119].

In the context of this thesis BSA was used to investigate LLPS processes and how the molecular ordering affects this phenomenon.

2.10.2 HUMAN INSULIN

Insulin is a protein hormone produced in the islets of Langerhans in the pancreas and it plays a crucial role in the metabolism of carbohydrates. Its amino acid sequence is well known (Figure 2.15): it is a dipeptide of 51 amino acids (MW 5808 Da) divided into two chains, A-chain (21 amino acids) and B-chain (30 amino acids), linked by two disulfide bridges (CysA7-CysB7 and CysA20-CysB19). A-chain contains an additional disulfide bridge between cysteine 6 and 11.
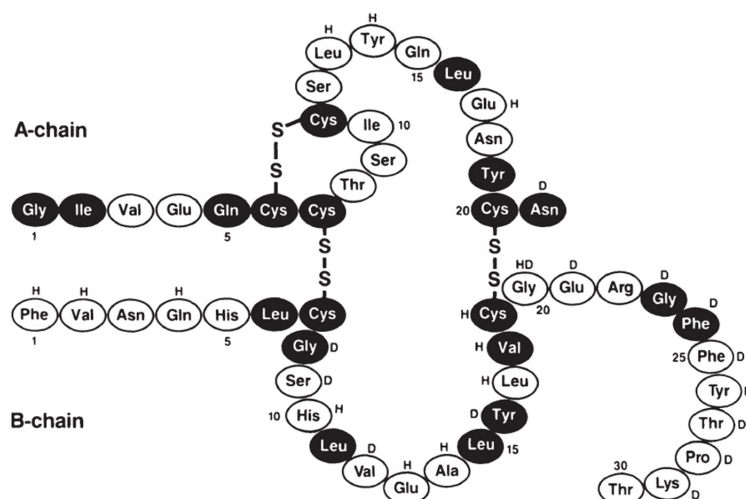
FIGURE 2.15: *Amino acid sequence of Human Insulin. The letters above each amino acid indicate the residues involved in the association of the molecule: D, dimer formation; H, hexamer formation. [120]*

The secondary structure of the A-chain consists of two alpha helices, and the B-chain is composed of a combination of an alpha helix and a beta sheet (Figure 2.16). In solution, Insulin is organized as monomers, dimers, tetramers, and hexamers, depending on the solution conditions as revealed for the first time in 1969 by Dorothy

Crowfoot Hodgkin through X-ray crystallography. The physiological predominant form is the hexamer, wherein three insulin dimers are coordinated by zinc ions. At low concentrations and low pH, Insulin is found as dimers and monomers.
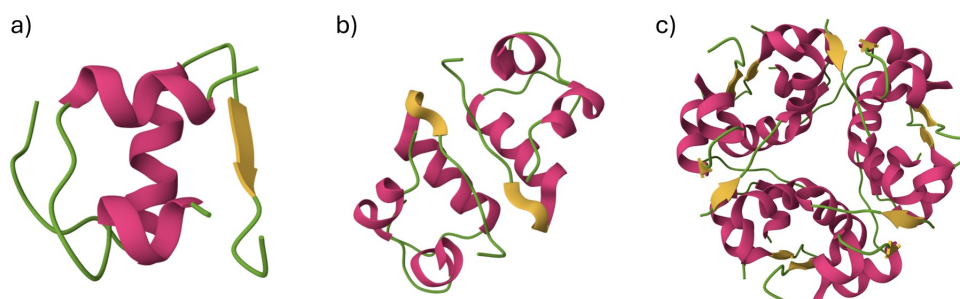

FIGURE 2.16: *Tertiary and quaternary structure of Human Insulin: a) monomer, b) dimer, and c) hexamer. The molecules are coloured according to the secondary structure: α-helix in pink, β-sheet in yellow and random coil in green.*

For the context of this thesis, it is important to note that insulin forms as a monomer in solutions with low pH and acetic acid. Conversely, in the presence of HCl, a prevalence of dimers is observed. The tertiary structure of the monomer is stabilized by hydrogen bonding, hydrophobic, van der Waals, and electrostatic interactions between residues from both chains. In particular, the Insulin monomer presents a hydrophobic core with polar residues positioned on the outer surface.

Human insulin is considered a model protein to study amyloid aggregation. The mechanism underlying the formation and the growth of amyloid aggregates was observed to be common to many other proteins [121], which for instance may be involved in the onset of neurodegenerative pathological conditions as α-synuclein for Alzheimer disease.

Insulin is highly amylogenic at acidic pH and high temperature, in presence of elevated salt concentration [40, 122]. In vitro insulin aggregation may result in the formation of different amyloid structures, characterized by specific morphologies. In Figure 2.17a) a representative TEM image of amyloid fibrils is reported: they are the most common and they occur at the solution condition just mentioned, both in quiescent and shaking conditions. At quiescent conditions insulin amyloid fibrils coexist with spherulites as shown in Figure 2.17b). Spherulites are tridimensional amyloid superstructures constituted by an amorphous core from which a corona of fibrils develops radially. If the aggregation process is carried out at a pH near the insulin isoelectric point which ranges between 4.5 and 5.0, insulin particulates occur, shown in Figure 2.17c). Particulates are micrometres size homogeneous aggregates, which exhibit a molecular structure that falls between the native and amyloid struc-
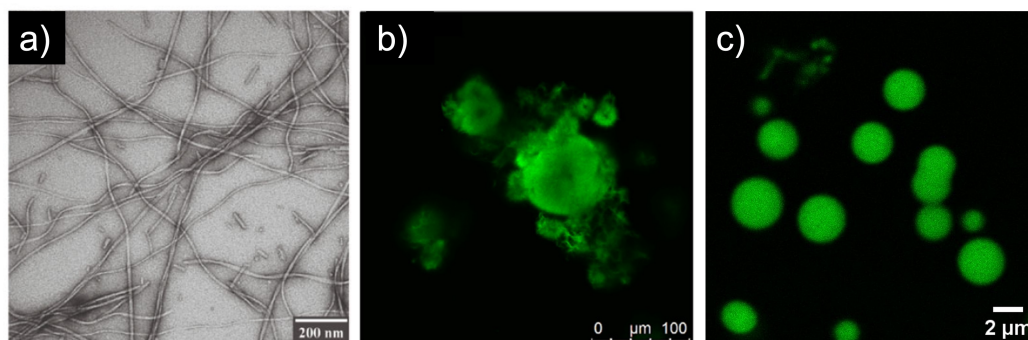
tures, often called amyloid-like.

FIGURE 2.17: *Structural polymorphism of Human Insulin aggregates which occur in different solution conditions. a) TEM image of human insulin amyloid fibrils [122], b) CLSM image of human insulin spherulites and fibril bundles stained by ThT [28], c) CLSM image of human insulin particulates stained by ThT.*

Thus, Insulin aggregation strongly depends on the solution conditions, such as pH, temperature, ionic strength, and protein concentration, which dictate the morphology of the aggregate species that occur, and the formation of amyloid superstructure is primarily controlled by electrostatic interactions [18].

Human insulin aggregation takes place in three phases: nucleation phase, growth phase and equilibrium phase [42, 123, 124, 125, 126]. During the nucleation phase (also known as lag phase) the protein undergoes conformational and structural changes which lead to the formation of oligomeric species. The association of oligomers produce the nuclei from which the growth of the aggregates starts. After the formation of the nuclei, more oligomers start to interact, and the aggregates start to grow: this is the beginning of the growth phase. Depending on the forming species the oligomers in solution self-assemble around the nuclei with different geometry: elongation along an axis in the case of fibril [74, 126], radial growth from centre point (nuclei) in the case of particulates or spherulites [31, 121, 127]. Finally, in the equilibrium phase, all the mature aggregates are formed and the process ends.

In 2008 Foderà et al. [40] studied the amyloid aggregation of insulin by means ThT fluorescence intensity. They observed how the thermally induced aggregation kinetics at low pH and high ionic strength did not show the same results. This translates into a higher variability of the aggregation kinetics both in terms of final ThT fluorescence intensity, and duration of the entire kinetics. This effect is more pronounced at lower protein concentrations, and it was associated with the stochastic origin of insulin aggregation at its early stages. The stochastic behaviour was attributed to the heterogeneous nucleation that insulin undergoes upon aggregation [42]. The aggregation process was found to be autocatalytic since the formation of fibrils promotes the formation of new nucleation points and new fibrils growth.

This can occur by two main mechanisms: fragmentation of pre-existing fibrils, or nucleation on the surface of the fibrils which results in their branching. The consequence of this autocatalytic process is that the growth phase of insulin aggregation is exponential since after the formation of the first nuclei (primary nucleation), the secondary nucleation takes over.

Many studies reported that insulin aggregation may be promoted by the presence of solid hydrophobic surfaces [128, 129, 130, 131]. Sluzky et al. showed that insulin aggregation begins with conformational alterations of the monomer at hydrophobic interfaces, specifically at the aqueous-solid interface [128, 131]. The initiation of this process occurs through the diffusion and adsorption of protein molecules to the interface. The primary driving force behind this process is the hydrophobic interaction between the monomer and the hydrophobic interface. Following this, the protein molecules within the boundary layer associate with these exposed hydrophobic regions, leading to the formation of aggregates. Eventually, these aggregates may desorb from the surface into the aqueous solution and act as nuclei for subsequent fibrillation. Sluzky et al. also reported that the addition of non-ionic surfactants or other additives to the solution may stabilize the native conformation state of insulin. This was observed to prevent the fibril formation of insulin at hydrophobic interfaces [128, 131]. In contrast to hydrophobic surfaces, a significantly longer lag phase for insulin aggregation has been noted in the presence of highly hydrophilic surfaces. This observation is likely attributable to the reduced extent of conformational changes induced in insulin by the hydrophilic surface [132].

For the aim of this thesis, another interesting aspect to discuss is what happens to insulin at the interface between water and a non-miscible liquid such as oil, being a liquid-liquid hydrophobic interface. Kwon et al. [133] monitored by means of spectroscopy techniques the aggregation of insulin at the interface between an aqueous solution and an organic solvent [133]. They found out that the insulin aggregation rate at the interfaces dramatically increases with respect to the aggregation process which occurs in solution. This phenomenon is likely due to the increased mobility of the liquid-liquid interface compared to a solid-liquid interface. Insulin can move more freely through the interface, to a certain degree. This promotes the unfolding and the fibril formation.

CHAPTER 3

Ordering of water molecules in Liquid-Liquid Phase Separation

In this chapter, the liquid-liquid phase separation of a Bovine Serum Albumin solution was studied in the presence of polymers as crowding agents and salts. These additives are crucial for the occurrence of LLPS phenomena in multicomponent protein systems. The first part of this study consists of assessing experimental conditions where LLPS occurs in the presence of PEG as crowding agent and in the following section the effect of chaotropic and kosmotropic co-solute to the LLPS. In the third section water ordering on the observed phenomenon is investigated and analysed using 6-acetyl-2-dimethylamino naphthalene fluorescent dye, more commonly known as ACDAN. ACDAN is described in literature as sensitive to the dipolar relaxation of the surrounding environment, particularly to water, given its abundance and strong dipole. For this reason, ACDAN is used to probe variations in the rotational degrees of freedom of water due to interactions with resulting macromolecules. Analysing the model system can greatly enhance understanding.

3.1 INTRODUCTION

In this study LLPS of BSA was induced by the addition of polyethylene glycol (PEG). PEG is often used for this porpoise in protein system [50, 53, 63, 64, 116, 134, 135]. This hydrophilic non-ionic polymer stands out among various additives its low impact on the biological activity of cellular components. In protein crystallography, PEG emerges as the premier precipitating agent for generating protein crystals. It is widely used to mimic crowding effects in vitro so that understating the thermodynamic properties of protein-PEG aqueous solutions holds fundamental significance [136]. In general, its effects on proteins are summarized as mutual volume exclusion on the entropy of the system.

In order to gain information on the role of molecular ordering in LLPS we analysed BSA condensation in the presence of non-ionic kosmotropic and chaotropic agents. This is aimed at the idea of controlling water dynamics and hydrogen bond

network and observing the resulting effects in phase separation. Entropic contributions are indeed fundamental to favour the separation of liquid phases where the component of the solution is differently organized. In a simplified description it is possible to think that in the condensed phase, proteins become close to each other inducing modification in the hydration water ordering. Water molecules experience confinement induced by high density of proteins in the condensate, or they can be replaced by sidechain [137]. LLPS is favoured in solution conditions where the entropy gain induced by water molecules release in the condensed phase and the free-energy gain from the formation of weak attractive intermolecular interactions are sufficient to offset the entropy loss due to molecular condensation. The subtle balance between hydrophobic and hydrophilic solvation contributions allows tuning different events and the final equilibrium state of the solution [138] and drives the reversible formation of protein compartments. To have direct experimental evidence on laws regulating this delicate equilibrium is difficult and the pivotal role of protein-solvent solvent-solvent interaction regulating is to be explored yet.

The terms "kosmotrope" and "chaotrope" emerged in the context of solvent properties referring to chemical compounds with the ability to increase or decrease, the structuring of water, respectively. The term 'kosmotrope' also denotes salts that promote the stabilization of protein structures, whereas 'chaotropes' are salts that induce a destabilization of protein structures. The term chaotropicity for the first time was used to describe the destabilization effects on DNA molecules in presence of salt ions ($NaClO_4$, KI, $LiCl$, etc.) [139]. The authors discussed the possibility that the observed effects were the result of changes in the thermodynamic activity of water, pointing out the role of water in regulating the stability of the macromolecules structure. However, they did not exclude that the salt ions interact directly with DNA molecules. About twenty years later, in the 80s, attention shifted to the effect of these compounds on water organization rather than to their direct effects on organic macromolecules such as proteins and nucleic acids, and since then, scientific research has focused on this aspect.

Nowadays, a large part of the literature agrees that chaotropic and kosmotropic compounds have effects on macromolecules and that these effects are mediated by water. In general, kosmotropic agents tend to stabilize proteins. These compounds are preferentially solubilized within the bulk of the solution and excluded from the hydration shell of the protein. This reduces the diffusion of water within the region near the protein, making its surface less flexible and thus stabilizing the native state of a protein [140]. On the contrary, chaotropic agents destabilize proteins by displacing water from the hydration shell [141]. In this way, the network of wa-

ter molecules is perturbed due to the disruption of hydrogen bonds between water molecules and to the formation of weaker hydrogen bonds between the chaotropic agent and water, leading also to an increase of water diffusivity. This increases the flexibility of proteins, thereby facilitating their denaturation.

Importantly, both ionic and non-ionic kosmotropic and chaotropic compounds exist. Ionic compounds include salts from the Hofmeister series, whose ordering or disordering power is mainly ascribed to the polarization they induce on water molecules in their solvation shell. Their influence on protein aggregation [142] and on LLPS has been investigated [117, 143]. Non-ionic compounds are highly soluble organic compounds with little or no tendency to aggregate, such as trehalose, glycerol (kosmotropic), urea, ethanol (chaotropic).

Both ionic and non-ionic kosmotropic compounds show analogous chemical behaviour when considering their interactions with proteins. Instead, ionic and non-ionic chaotropic compounds show profound different behaviour in protein solutions. Ionic compounds tend not to interact with proteins, acting only on water structure, non-ionic compounds, have been shown to directly interact with protein molecules due to their smaller hydration shell [144]. For example, non-ionic compounds, such as urea or acetone, can interact with hydrophobic patches and suppress native folding [145, 146].

3.2 Experimental results and discussion

3.2.1 Liquid-Liquid Phase Separation of BSA induced by thermal treatment

The dynamic processes during a LLPS of a BSA solution were investigated, by using temperature as a triggering physical parameter for phase transition, since it is one of the most easy-to-access experimental conditions to modify. After screening several experimental conditions, the optimal ones were selected. The solution consists of 25 mg/ml BSA dissolved in 100 mM Acetate buffer at pH 4.6 in the presence of PEG-4000, as a molecular crowding agent. PEG is commonly used in literature to induce LLPS in protein and in biomacromolecules solution [47, 147], and therefore to modulating the phase behaviour of biomolecular systems. Being an inert biocompatible polymer, generally, its interaction with protein is minimal and its main effect on protein solution is due to exclusion volume effects [147, 148]. The specific effects of PEG on protein LLPS depends on the concentration and molecular weight: in particular higher concentration and higher molecular weight favours

the LLPS process [50, 147, 149, 150], without altering the propensity of protein phase separation under identical solution conditions.
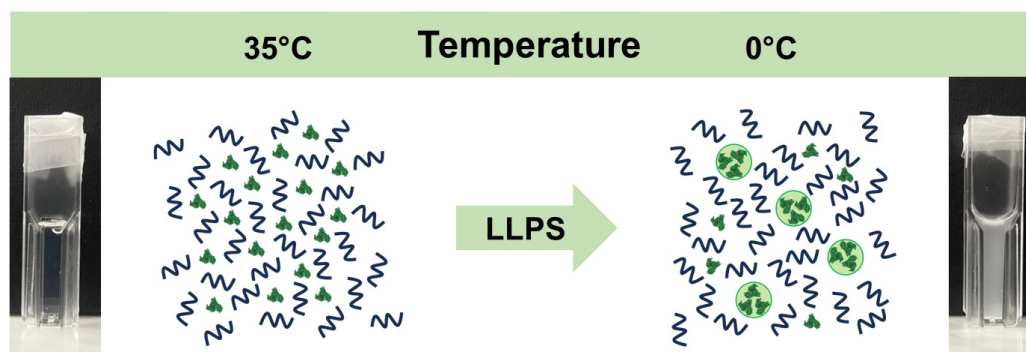

FIGURE 3.1: *BSA 5 mg/ml (shown as green molecules in the sketch) is dissolved in 100 mM acetate buffer at pH 4.6 and 68 mg/ml PEG-4000 (blue waves) is added as crowder agent. At 35°C the solution is clear, indicating the homogeneity of the solution. Upon decreasing the temperature, the solution becomes turbid and white. This indicates the formation of BSA coacervates afterwards LLPS occurs, reported as green circles in the right part of the sketch.*

In Figure 3.1 photographs of the sample prior to and after the occurrence of LLPS and a schematic representation of the process are reported. The sample consists of 5 mg/ml BSA and 68 mg/ml PEG-4000 dissolved in 100 mM acetate buffer (pH = 4.6). The photo on the right shows the appearance of the solution at 35°C: the solution is clear, indicating a homogeneous solution as shown by the schematic representation, where the PEG-4000 molecules, shown as blue waves, and the BSA molecules, shown in green, are homogeneously distributed over the entire volume. Upon decreasing the temperature, the solution becomes turbid and white, indicating the formation of coacervates. These are represented as circles containing BSA molecules. According to literature [26, 47, 48], the diluted phase is depleted from protein molecules, which are thus sequestered by the formed coacervate.

BSA is known to undergo LLPS in presence of multivalent cations [53, 118, 151], or in presence of PEG with different molecular weight and in different solution conditions [50, 116, 117, 134, 152, 153]. The study reported in this thesis is focused on the LLPS induces by PEG.

It is known that BSA molecules in general exhibit a poor affinity for PEG [154, 155]). However, by increasing PEG molecular weight the molecular affinity between BSA and PEG increases as well mainly due to hydrophobic interactions [155]. For instance, having a compact structure, PEG 8000 was found to perturb the protein surface, interacting with the tyrosine and tryptophan residues [154]. Similar results were also reported for PEG with higher molecular weights (PEG 10000 and PEG 20000) which were observed to bind to BSA surface [155]. The extent of these interactions depends on the PEG concentration. PEG with lower molecular

weights, being more flexible and less compact, cannot penetrate the hydration layer, resulting in a lower interaction with BSA surface [154]. To reduce the PEG-BSA in the study here reported, PEG 4000 was used.

As mentioned above the main reason why PEG induces LLPS of BSA solution is the excluded volume effect. Excluded volume induces depletion interactions between BSA molecules [134, 147]. These are entropic interactions which result in attractive forces between large colloidal particles (as protein) and arise to reduce the excluded volume for arise to decrease the excluded volume for the molecular crowders. Depletion interactions are the main driving forces for coacervates formations [147]. This leads to phase separation into a protein-rich phase and a PEG-rich phase when the temperature is lowered [134]. At higher temperatures, thermal motion contributes to keeping protein molecules dispersed. When the temperature decreases, the reduced kinetic energy favours the formation of more stable interactions between protein molecules, promoting LLPS. Moreover, another factor to keep in mind is that upon decreasing the temperature, the solubility of BSA in water decreases, leading to enhanced protein-protein interactions over protein-solvent interactions. PEG amplifies these effects by promoting closer proximity of protein molecules, by means of the exclusion volume effects, further favouring LLPS of the BSA solution at low temperature [147].

The sample was then investigated by means of fluorescence microscopy to analyse the coacervates at the microscale level.

Four representative two-photon microscopy fluorescence images are reported in Figure 3.2. ACDAN was used as a fluorescent probe to image the coacervate since ACDAN fluorescence arises mainly from the coacervates. Specific details and uses of this fluorescent dye will be investigated below. The sample presents several spherical BSA coacervates which are the green circles in the images. The coacervates have different sizes ranging from a few micrometres to about ten micrometres, and they are dispersed in all the solution volume. The coacervates are highly dynamic and coalesce when they encounter and touch each other. This indicates their liquid behaviour. Moreover, the coacervates tend to sediment to the bottom of the glass coverslip.

To gain information on the PEG concentration effects on BSA LLPS, the scattering intensity of the solution throughout the transition was monitored as a function of temperature. The sample underwent a heat treatment consisting of a temperature ramp from 35°C to 0°C (scan rate is 15°C/hour) and elastic scattering was measured at 650nm i.e. where no absorption or fluorescence signal is expected from the sample.
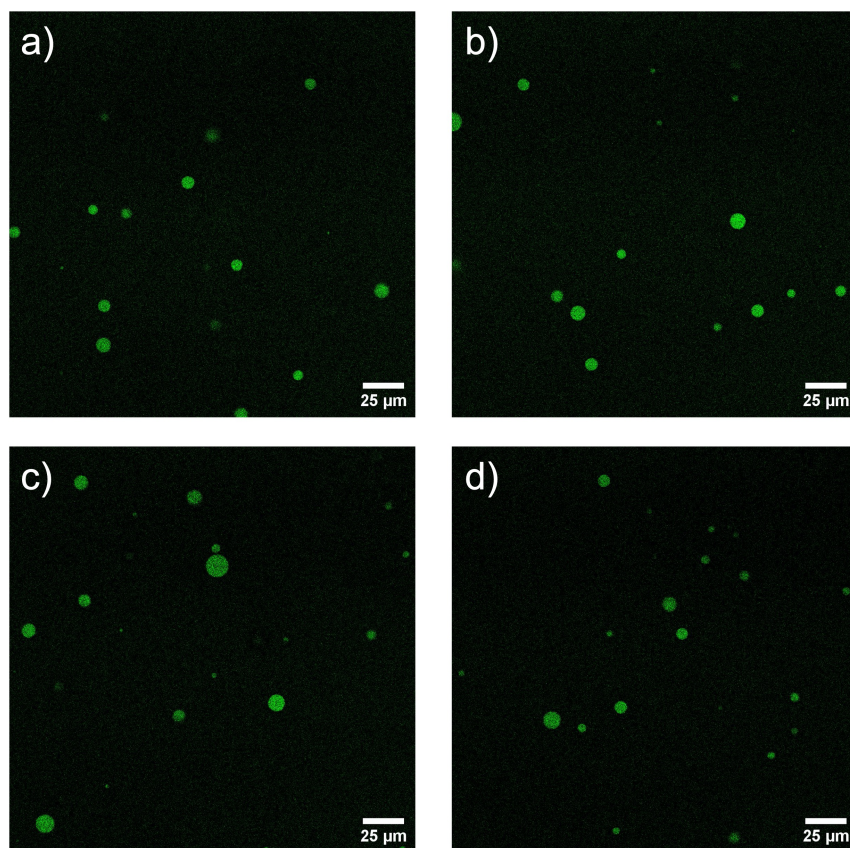
FIGURE 3.2: *1024×1024 pixels representative two-photon microscopy fluorescence images of a sample consisting in 25 mg/ml BSA, and 76 mg/ml PEG 4000 dissolved in 100 mM acetate buffer at pH = 4.6. At this PEG concentration the solution the BSA coacervates are present at room temperature 23°C. The sample is stained with 30 μM ACDAN (λ_{exc} = 780 nm, detection range = 450 - 600 nm).*

In Figure 3.3a), the scattering intensity as a function of temperature is reported for BSA samples containing increasing concentrations of PEG (ranging from 60 mg/ml to 76 mg/ml). At each PEG concentration, an increase in scattering intensity is observed below a certain temperature. At temperatures lower than this threshold, a relatively linear growth in signal intensity is observed until reaching a certain point, after which the intensity begins to decrease due to sample sedimentation (data not reported). Specifically, when the solution is in a single phase, it remains homogeneous and transparent, leading to negligible scattering intensity. When cooled below the transition temperature, the solution begins to separate into two phases. At the macroscopic level, the phase separation is evident as at low temperatures the samples become turbid (as shown in Figure 3.1) and afterwards the samples separate in two distinct phases, as a consequence of coacervates coalescence and sedimentation. Even after sedimentation of the dense phase has occurred, the LLPS process can be reversed bringing back the sample to 35°C and agitating it to mix the two phases.
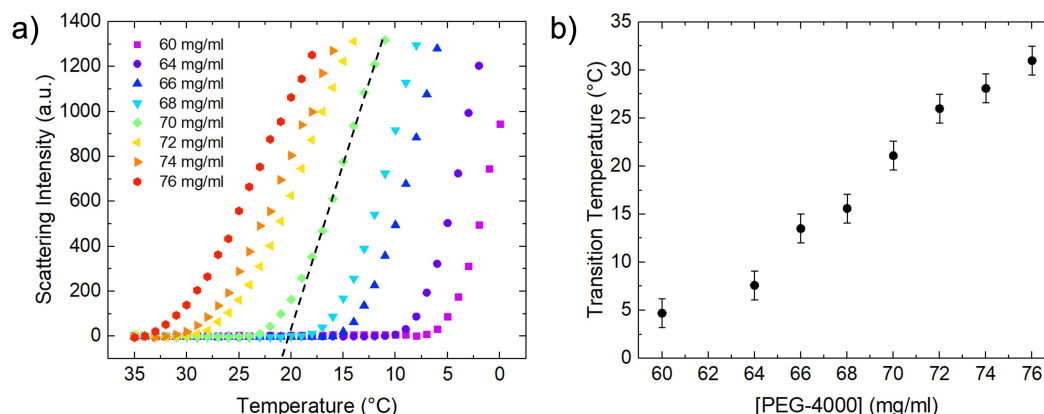
Figure 3.3: *a) Scattering intensity of the sample (BSA 25 mg/ml, PEG-4000, in acetate buffer 100 mM at pH 4.6) was measured at 650 nm as a function of temperature. The scan temperature is 15°C/hour. The black dashed line is a representative linear fit of the growth phase of the scattering data. When the solution is homogeneous the scattering intensity at this wavelength is negligible, but it dramatically increases when the sample undergoes a phase separation. With increasing PEG concentration, the LLPS in the sample occurs at increasing temperatures. b) Phase Transition temperature from the temperature scans at different PEG concentrations measured as the x-intercept of the linear fit (black dashed line). The transition temperature increases with increasing PEG concentration.*

The scattering intensity measurements in the growth region were fitted using a straight line, and the transition temperature was determined as the resulting x-intercept at each PEG concentration. These data are reported in Figure 3.3b), representing a branch of the phase diagram of the sample. Above the experimental points depicted, the solution is homogeneous, while below these points, the solution separates. Notably, as the PEG concentration increases, the temperature transition temperature also rises. This observation is in agreement with what is already present in literature [117, 134, 147]. The excluded volume effect which induces LLPS, depends on the concentration of the crowding agent in solution. In this context, the transition temperature is the temperature at which the depletion forces between BSA molecules overcome the repulsive interactions which governate the homogeneous phase. This translates into the occurrence of LLPS. Increasing the PEG concentration, the excluded volume effects are greater and therefore the depletion forces overcome the repulsive interaction at higher temperatures. The fact that the temperature transition depends on the PEG concentration is an indication that, in the analysed concentration range, LLPS is induced mainly by the exclusion volume effects, and not by other specific interactions (e.g., between PEG and BSA) which could arise within the solution [147]. This is further suggested by the fact that the scattering data at different PEG concentrations present linear regions with similar slopes. This indicates that the same LLPS process occurs in each sample, and that the PEG concentration does not affect the propensity of BSA to undergo LLPS.

51

3.2.2 PHASE STABILITY ALTERATION INDUCED BY NON-IONIC KOSMOTROPIC AND CHAOTROPIC AGENTS

The main aim of the study is to analyse the role of water and in general molecular order in the LLPS process. For this reason, the impact of both chaotropic and kosmotropic compounds on the LLPS process under examination was investigated. In particular, non-ionic disordering and ordering compounds were selected. Ethanol (EtOH) was used as a chaotropic agent and Glycerol as a kosmotropic one.

Other studies on protein LLPS were conducted using salts from the Hofmeister series [143, 156]. These salts induce significant modification in water structure and ordering at quite high concentrations (hundreds of millimolar/molar). Strong intermolecular electrostatic interactions may induce changes in the analysed system which can overshadow the possibly weaker contributions of water ordering, mediated by transient hydrogen bonds and interactions with lower potential, such as Van der Waals effects, and so forth. In order to reduce electrostatic long-range interactions effects, all the experiments were performed in solution at pH close to the isoelectric point of BSA which is reported to range from pH 4.5 to 5.0.

Analogous measurements to the ones reported above were performed keeping PEG 4000 concentration at 68 mg/ml in the presence of EtOH and Glycerol. These experiments are aimed at evaluating whether and how different concentrations of these additives impacted LLPS. PEG concentration was selected to optimise measurement conditions allowing having similar dynamical ranges both above and below the transition temperature. From now on the 68 mg/ml PEG sample will be called the standard sample. In Figure 3.4 the results of the experiments using solution containing EtOH are reported: Figure 3.4a) shows the scattering intensity as a function of the temperature at various concentrations of EtOH. In Figure 3.4b) the transition temperatures for each temperature scan are reported. The transition temperatures are obtained as described above. The temperature scan presents an analogous profile to the one in the absence of EtOH in the temperature range explored revealing that EtOH affects the LLPS occurrence. Specifically at increasing EtOH concentration the transition temperatures shift to higher values. At concentrations higher than 4% v/v the sample undergoes to LLPS at a higher temperature than 35°C. Our experimental setup therefore did not allow us to detect if at higher EtOH concentrations the observable effect changes or if it reaches a plateau at a certain concentration. From data reported in Figure 3.4b) it is evident that in the concentration range under analysis, the transition temperature depends on EtOH Concentration. All these observations indicate that the LLPS process is promoted by the

addition of EtOH to the solution, with the effectiveness increasing in correlation with higher EtOH concentrations. It cannot be excluded that the described effects are not due to a direct interaction between EtOH and BSA molecules. However, EtOH is known to induce modification in the hydration shell of protein molecules. It is reported that the presence of EtOH induces the exclusion of water molecules from the protein hydration layer causing its thinning. This significantly destabilizes the protein conformational state, leading to a loss of its three-dimensional structure, and a looser structure. This, in turn, modifies protein-protein and protein–water intermolecular interactions, and it was described for many proteins, including BSA [157, 158, 159]. In particular, larger surfaces enable a greater number of protein-protein interactions, that therefore facilitate LLPS. This effect is known to be concentration dependent, in line with the presented results [21, 157, 160, 161].
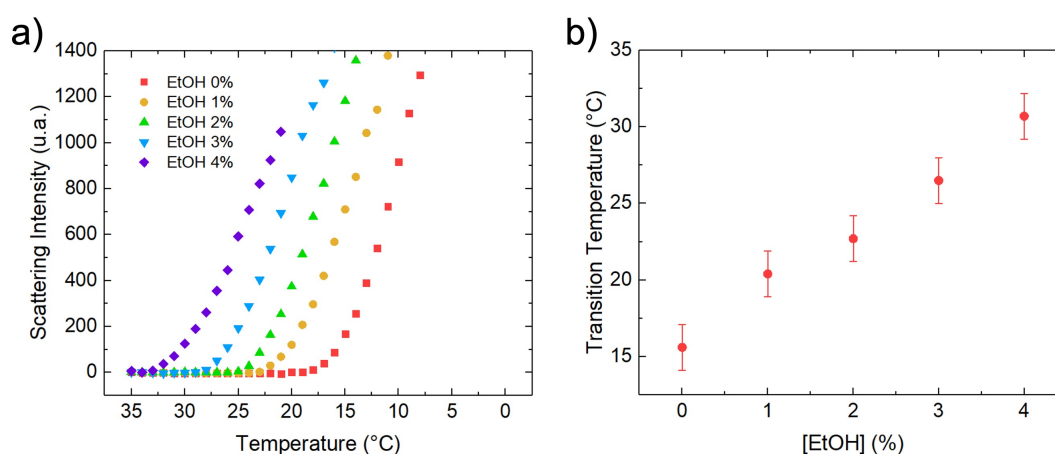

FIGURE 3.4: *Effect of non-ionic chaotropic agent on LLPS process. a) Scattering intensity measurements as a function of the temperature of the standard sample (BSA 25 mg/ml, PEG-4000 68 mg/ml, in acetate buffer 100 mM at pH 4.6, scan rate 15°C/h) at different EtOH concentration. Increasing the EtOH concentration, the LLPS occurs at higher temperatures indicating the process is favoured. b) Transition temperature increases linearly with the ethanol concentration.*

Figure 3.5 shows the effect of Glycerol on the BSA LLPS. Similarly to what reported above, Figure 3.5a) shows scattering measurements as a function of temperature at various concentrations of Glycerol. In Figure 3.5b), the transition temperatures obtained from each temperature scan, as described above, are reported. All the temperature scans are similar to each other, including the one measured without Glycerol, in the examined temperature range. Glycerol affects the occurrence of LLPS, similarly to EtOH. However, contrarily to EtOH, LLPS in these samples occurs at lower temperatures, i.e., the transition temperature decreases at increasing Glycerol concentration. This indicates that the addition of Glycerol to the sample makes LLPS process less energetically favourable and at even higher concentrations, it completely inhibits the phase separation. Glycerol concentrations higher

than 8% v/v were not investigated, since the sample undergoes LLPS at a temperature below the investigated temperature range. Data reported in Figure 3.5b) show that in the concentration range, under analysis, the transition temperature depends on Glycerol concentration.
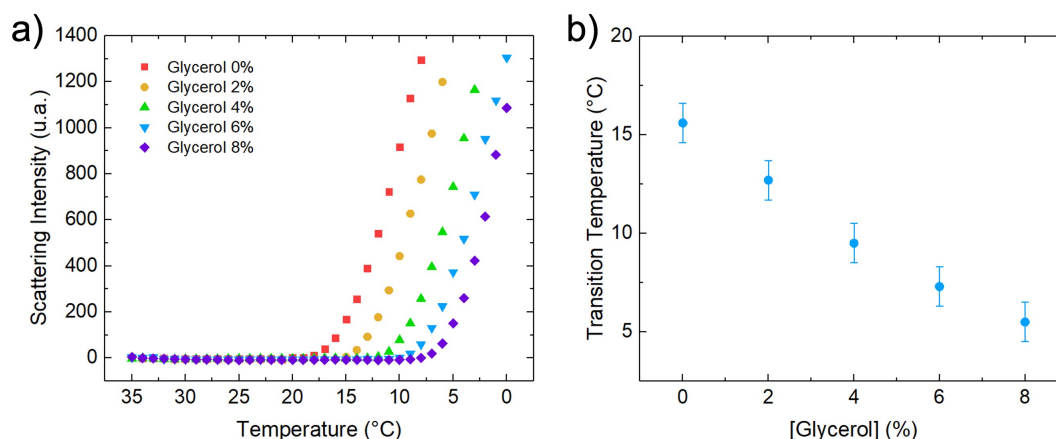

FIGURE 3.5: *Effect of non-ionic kosmotropic agent on LLPS process. a) Scattering curves of the standard sample (BSA 25 mg/ml, PEG-4000 68 mg/ml, in acetate buffer 100 mM at pH 4.6, scan rate 15°C/hour) with different concentration of glycerol as kosmotropic agent. LLPS occur at lower temperatures as the glycerol concentration increases, denoting that glycerol stabilizes of sample. b) Transition temperature decreases linearly with the glycerol concentration.*

As expected, the influence on the addition of glycerol to the solution has the opposite result to what was observed for EtOH. It has been demonstrated that glycerol enhances protein structure and protein stability [161, 162]. Being strongly hydrophilic, glycerol molecules strongly bind from 2 to 4 water molecules and its hydration has been determined to be about 5.58 water. Conversely, its affinity for polar residues on the protein surface is weaker. Therefore, glycerol molecules are thermodynamically favoured to be preferentially excluded from the hydration shell of protein molecules. This leads to a more ordered and stable hydration shell of protein molecules. As a result of increased stability of protein structure, the intermolecular protein interactions are diminished, and therefore LLPS and more in general all the supramolecular assembly processes are reduced. From a microscopical point of view, this reflects also an overall increase in solution viscosity, which results in a reduction of the dynamic of molecules. This provides a heuristic explanation for which glycerol prevents LLPS from occurring at higher concentrations.

3.2.3 PROBING WATER USING ACDAN FLUORESCENCE

To evaluate the overall molecular ordering of the system during LLPS process, and its possible modifications, we exploit the spectroscopic properties of the fluores-

cent molecule ACDAN (6-acetyl-2-dimethylamino naphthalene). This molecule is a probe from the DAN family and among LAURDAN and PRODAN it is the most hydrophilic. ACDAN fluorescence depends on both the dipolar relaxation and the polarity of the solution. The dipolar relaxation is the ability of the dipoles in solution to rotate and to be re-oriented by ACDAN molecules. Higher dipolar relaxation indicates a freer molecule and a more disordered state, while low dipolar relaxation indicates that the rotation of the molecules is hindered and a more rigid and ordered state. For this reason, in literature, it is often used to explore the order of water molecules and to thus probe the crowded milieu both in vitro and in vivo [92, 94, 96]. When ACDAN experience a higher dipolar relaxation of the solution, its fluorescence spectrum is red-shifted, while if the dipolar relaxation is lower ACDAN fluorescence is blue-shifts. Similarly, when the dye experiences a polar solvent the fluorescence red shifts, otherwise it blue shifts. More details on the functioning of the ACDAN and its fluorescence properties are reported in Chapter 2.
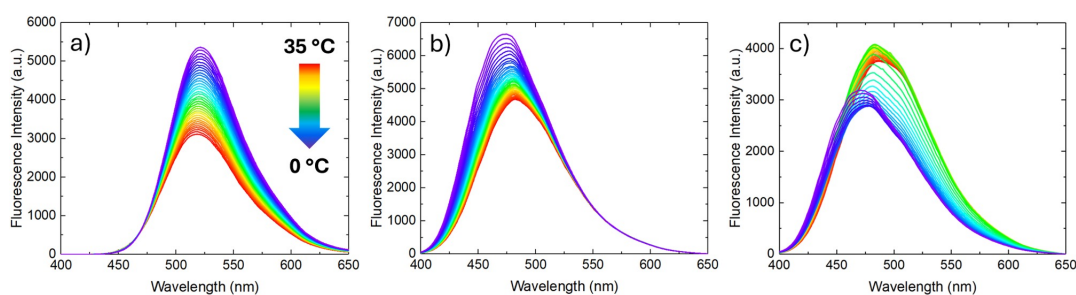

Figure 3.6: *ACDAN fluorescence spectra of three samples: a) 68 mg/ml PEG in 100 mM acetate buffer pH 4.6, b) 25 mg/ml BSA in 100 mM acetate buffer pH 4.6, c) standard sample. 30 μM ACDAN was added to each sample. The spectra were acquired during a temperature scan from 35°C to 0°C, with a scan rate of 15°C/hour. The trend of the ACDAN fluorescence spectra for the standard sample is different from the others, which do not undergo LLPS, being non-monotonic. The fluorescence spectra are corrected for instrumental response. λ_{exc} = 390 nm, Excitation bandwidth = 2.5 nm, Emission bandwidth = 2.5 nm, scan speed = 100 nm/min.*

Here ACDAN is used to probe in bulk how the molecular environment of the solution changes when it undergoes a LLPS process, by monitoring the modifications in its fluorescence spectra. In Figure 3.6 the ACDAN fluoresce spectra during the temperature scan in three samples are reported. The samples consist in: a) 68 mg/ml PEG, b) 25 mg/ml BSA, and c) a standard sample which is the combination of the two. All the samples were dissolved in 100 mM acetate buffer pH 4.6 and 30 μM ACDAN was added to the solutions. The temperature scan is measured from 35°C to 0°C and the scan rate is 15°C/hour. The first two measurements are used as a reference for taking into account the effect induced by the thermal treatment on single components of the standard sample. Figure 3.6a) shows the ACDAN fluorescence

spectra measured in the PEG sample. The first spectrum measured at 35°C (shown in red) is centred at about 520 nm. During the temperature scan, the fluorescence intensity increases while the temperature decreases. In Figure 3.6b) the ACDAN fluorescence spectra are reported for the BSA sample. The spectrum acquired at 35°C is centred at 480 nm. Similarly, to the PEG experiment, the fluorescence intensity increases while the temperature decreases. Moreover, the spectra measured at lower temperatures are blue-shifted. It is possible to speculate that the increase of the fluorescence intensity at lower temperatures is solely induced by thermal effects since these two samples do not change and do not undergo LLPS.

Figure 3.6c) show the ACDAN fluorescence spectra of the standard sample. The first spectrum measured at 35°C is centred at about 490 nm. It is evident how the fluorescence spectra acquired during the temperature ramp do not monotonically increase while the temperature decreases, as it is reported for ACDAN spectra measured in the PEG sample and in the BSA sample. This is probably due to the phase transition which occurs in the standard sample. By lowering the temperature, the overall fluorescence intensity increases and the spectral shape changes, towards shorter wavelengths. At about 20°C the fluorescence intensity starts to decrease while continuing to blue-shift, until about 8°C. At this temperature, until the end of the temperature ramp, the fluorescence intensity increases again. Changes in fluorescence spectra clearly indicate a non-monotonic decrease of dipolar relaxation during the temperature scan. The observed spectral changes certainly result from the combined effects of changes in the molecular environment experienced by AC-DAN and the intrinsic effects of temperature. Indeed, at lower temperatures, the rate of the radiative pathway is higher. Moreover, at low temperatures, the solvents usually become more viscous, and the time for solvent reorientation increases, resulting in the lowering of dipolar relaxation [72]. This would translate into an increase in fluorescence intensity and a blue shift. It is reasonable to speculate that in the temperature range between 35°C and 20°C the spectra modifications are dominated by the thermal effects since macroscopic effects of LLPS are not observed (as shown in Figure 3.3a). On the opposite, in the range between 20°C, and 8°C the fluorescence modifications are strongly affected by LLPS as the fluorescence intensity is observed to decrease. Similarly, below 8°C the fluorescence intensity starts to increase suggesting that modifications due to phase transition are ended. In this case, it is not possible to rule out further evolution of the sample, due for instance to the maturation of the protein coacervates.

In order to quantify ACDAN fluorescence spectra changes as a function of temperature, Generalized Polarization (GP) was calculated at 450 nm and 560 nm:

$$GP = \frac{I_{450} - I_{560}}{I_{450} + I_{560}} \tag{3.1}$$

Figure 3.7shows that ACDAN GP changes as a function of temperature for the same three samples in which ACDAN fluorescence was measured: 25 mg/ml BSA (blue squares), standard sample (green circles), and 68 mg/ml PEG (yellow triangles).
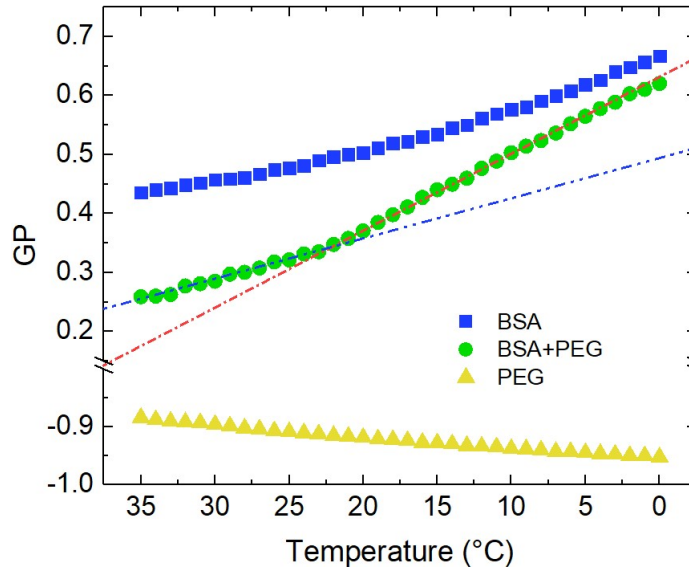

Figure 3.7: *GP of ACDAN fluorescence spectra for three samples: 25 mg/ml BSA (blue squares), standard sample (green circles), and 68 mg/ml PEG (yellow triangles). All the samples were prepared in 100 mM acetate buffer pH 4.6 and 30 μM ACDAN was added to each sample. The spectra were acquired during a temperature scan from 35°C to 0°C, with a scan rate of 15°C/hour. GP was calculated at 450 nm and 560 nm. GP of the standard sample shows a binodal trend, highlighted by the blue and red dashed lines. The slope change occurs at about the transition temperature of the standard sample.*

GP measured in the BSA sample start from a positive value at 35°C and increase almost linearly. Contrarily the GP measured in the PEG sample starts from a negative value and slightly decreases linearly as well. The standard sample starts from a positive value between the BSA sample the initial value and the PEG sample's initial value, indicating that ACDAN is sensitive to both the BSA and the PEG environment. Overall, the GP measured for the standard sample increase. Importantly, it presents a present a biphasic behaviour, highlighted by the blue and the red dashed lines shown in Figure 3.7. The blue dashed line corresponds to the slope of the initial growth of the GP measured in the standard sample. The blue dashed line is parallel to the GP data calculated in the BSA sample, denoting that the variation of GP value and more in general of the fluorescence spectra are caused by the same thermal effects. A change of the slope is observed at about 20°C, which is the same temperature at which the trend inversion of ACDAN fluorescence spectra intensity

is observable, as shown in Figure 3.6c). This temperature is also compatible with the transition temperature for this sample. The slight difference between the two obtained temperatures might be due to the fact that fluorescence processes are more sensitive to modification in the micro-environment than scattering. After 20°C the slope of the GP data increases as shown by the red dashed line, indicating that a new process (LLPS in this case) is taking place in the sample. Both the GP and the overall fluorescence spectra suggest that ACDAN fluorescence is sensitive to the variation of the micro-environment caused by LLPS process.

The variations in the environment which ACDAN experiences in the different samples are then investigated. Figure 3.8 shows a comparison between normalized ACDAN fluorescence spectra at 35°C (reported in panel a) and at 0°C (reported in panel b) for the same three samples: 68 mg/ml PEG (yellow), 25 mg/ml BSA (blue) and standard sample (green). As described above, data reported in Figure 3.7 show that the ACDAN fluorescence spectrum measured in the BSA sample present a pronounced blue-shift with respect to the ACDAN fluorescence acquired at the same condition in the PEG sample. The ACDAN fluorescence measured in the standard sample stands in between and its spectrum is a linear combination of the PEG and BSA spectra.
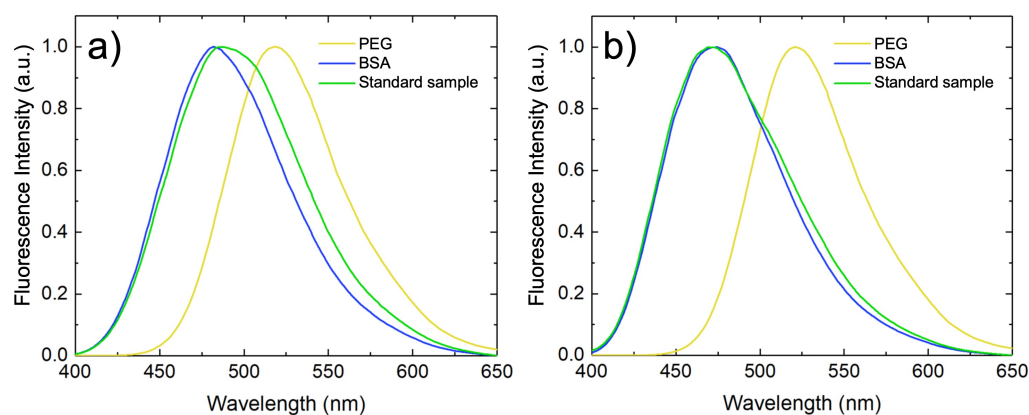

FIGURE 3.8: *Normalized fluorescence spectra of ACDAN in three samples: of the 25 mg/ml BSA (blue), standard sample (green), and 68 mg/ml PEG (yellow). All the samples were prepared in 100 mM acetate buffer pH 4.6 and 30 μM ACDAN was added to each sample. a) Spectra acquired at 35°C and b) spectra acquired at 0°C, after the temperature ramp. λ_{exc} = 390 nm, Excitation bandwidth = 2.5 nm, Emission bandwidth = 2.5 nm, scan speed = 100 nm/min.*

Figure 3.8b) shows that at 0°C, after LLPS occurs, the ACDAN fluorescence spectrum in the standard sample almost overlaps with the ACDAN fluorescence spectrum in the BSA sample measured at the same experimental condition, having, in addition, a small red component at the same position of ACDAN fluorescence spectrum in the PEG sample. The fact that the ACDAN fluorescence measured in the standard sample resembles the ACDAN fluorescence measured in the BSA sam-

ple may be an indication of a higher affinity of ACDAN for the BSA environment with respect to the PEG environment. This is also suggested by the fact that the standard sample GP value is similar to the BSA GP value. To explore the origin of the blue shift in the BSA with respect to the PEG sample and the reason behind which the ACDAN fluorescence in the standard sample at 0°C strongly resembles the fluorescence in the BSA sample, some observation from the measurements reported above must be highlighted.

As shown by the fluorescence microscopy images reported in Figure 3.2, after LLPS takes place, the ACDAN fluorescence signal mostly arises from protein condensates. The diluted phase presents a diffuse fluorescence signal, in line with the fact that ACDAN is highly hydrophilic, but it is much lower than the fluorescence intensity detected within the coacervates. This may denote either an increase of ACDAN concentration within the dense phase or a modification of the microenvironment experienced by the dye or both. However as shown in Figure 3.6, when comparing ACDAN fluorescence intensity measured in the BSA sample with the one measured in the PEG sample, in the BSA sample it is always higher, even if non phase separation occurs. The fact that the ACDAN fluorescence intensity is higher even in this case, suggests that the dye preferentially partitions to the BSA molecules and therefore when LLPS takes place, it partitions to the coacervates.

Being highly soluble, ACDAN is used in literature to investigate the dipolar relaxation of water in crowded solution [92, 93, 94, 96, 97, 163], connecting it to the rotational dynamics of water.

For instance, Ambroggio et al. [163] observed the LLPS of the capsid proteins of the Dengue virus and the Zika virus and reported how the water relaxation sensed by ACDAN within the coacervates of these two proteins were different and how their structure may therefore impact on the structure of water. Thoke et al. [92], reported how ACDAN fluorescence can probe in vitro the water dynamics in yeast cells (Saccharomyces cerevisiae) during the metabolism of glucose, detecting a strong coupling between ACDAN fluorescence intensity and the concentration of both ATP and NADH. They moreover highlighted how ACDAN does not partition in cellular membranes, being highly hydrophilic. Vorontsova et al. [94] used ACDAN as a tool to quantitively monitor the water activity to study in vivo the macromolecular crowding in a zebrafish ocular lens.

The presented results highlight a direct interaction between the BSA and ACTAN dye. BSA is a transport protein renowned for its binding capabilities, attributed to its hydrophobic pockets. These pockets make BSA able to interact with a wide variety of molecules also thanks to the structural flexibility of these binding sites.

59

This has certainly to be taken into account for the interpretation of fluorescence experiment results. The interaction between a dye of the same family (PRODAN) and BSA was previously described. This interaction results in a spectral blue-shift and in an increase of fluorescence intensity, in line with what was reported before [89]. PRODAN and ACDAN are two similar molecules only differing by the presence of an ethyl group (PRODAN) instead of a methyl group (ACDAN), making PRODAN slightly more hydrophobic and therefore increasing its binding ability to hydrophobic pockets of BSA. ACDAN is sensitive to water dipolar relaxation, but it is not possible to exclude that the signal reflects the properties of hydration water protein. The spectral blue shift indicates that either ACDAN experiences a more hydrophobic environment or a lower dipolar relaxation or both. Therefore, it is reasonable to speculate that some ACDAN molecules enter within the BSA pockets, sensing its hydrophobic environment. This results in a spectral blue shift due to the restricted mobility of the molecules within the pockets.

All the measurements reported so far are bulk measurements obtained in cuvette. Bulk measurements provide averaged data over large sample volumes, which is ideal for obtaining representative and statistically significant information about the overall properties of a sample. These measurements do not allow to discern specific fluorescence features of the different phases formed following a LLPS. More detailed information can be obtained taking advantage of the spatial resolution that microscopy can offer. Moreover, and more importantly, for the aim of the study reported in this chapter, microscopy techniques provided quantitative information using smaller sample volumes.

Two-photon microscopy was used to analyse and compare the ACDAN fluorescence in the homogeneous phase before LLPS occur, and in the diluted and concentrated phase of the samples. The normalized ACDAN fluorescence spectra in the homogeneous phase (green squares), in the diluted phase (magenta circles) and in the concentrated phase (cyan triangles) are reported in Figure 3.9a). Figure 3.9b) shows a table reporting the GP values for the homogeneous, diluted and concentrated phases. GP were calculated using the same wavelength of the previous analysis (450 nm and 560 nm).

ACDAN fluorescence reported in Figure 3.9a) was excited at 780 nm and the fluorescence signal was acquired in the range between 400 nm and 650 nm. The fluorescence spectra were acquired at pixel resolution within the image, using a 15 nm bandwidth and 5 nm step size. The sample used for the homogeneous phase is the standard sample (68 mg/ml PEG) which has a transition temperature below room temperature, and the sample used for the diluted and concentrated phase contains 76
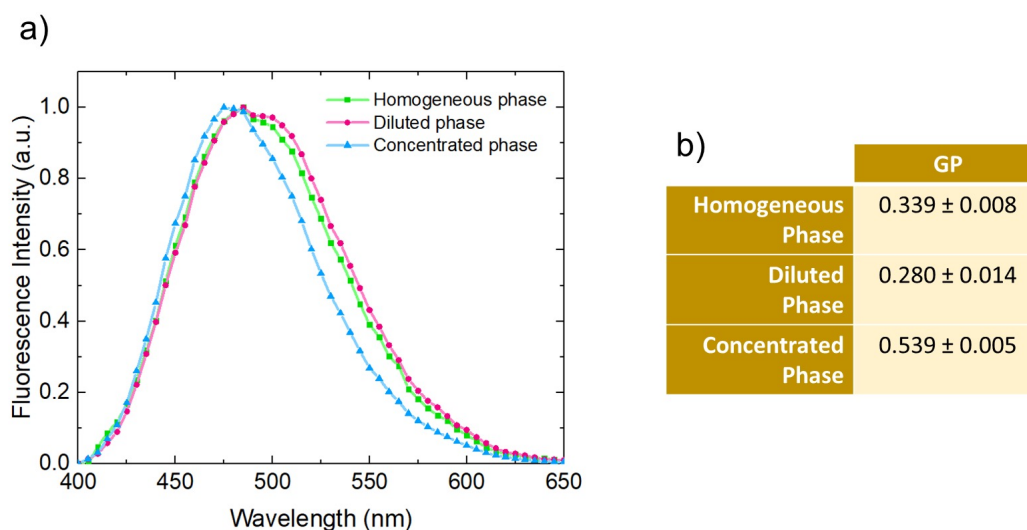
a)

b)

	GP
Homogeneous Phase	0.339 ± 0.008
Diluted Phase	0.280 ± 0.014
Concentrated Phase	0.539 ± 0.005

FIGURE 3.9: *a) Normalized fluorescence spectra of homogeneous phase (green squares), diluted phase (magenta circles) and concentrated phase (cyan triangles), acquired by two-photon microscopy (α_{exc} = 780 nm, bandwidth = 15 nm, step size = 5 nm). The homogeneous phase is the standard sample (68 mg/ml PEG) and the concentrated phase and diluted phase are obtained from a sample containing 76 mg/ml PEG and 25 mg/ml BSA. The concentrated phase spectrum and the diluted phase spectrum are respectively blue-shifted and red-shifted with respect to the homogeneous phase. b) GP of ACDAN fluorescence spectra showed on the left calculated at 450 nm and 560 nm. The higher GP indicates a more ordered phase.*

mg/ml PEG, which is already separated at room temperature. As already mentioned, it is reasonable to compare processes at different PEG concentrations, because the LLPS process is the same and what changes is the fraction of the dense phase that separates from the rest of the solution. The concentrated phase and the diluted phase were physically separated by centrifugation ($10^4 \times$g for 10 min at 20°C) since the protein coacervates which occur following LLPS are highly dynamic, and it could not be possible to perform long measurements as the one needed to acquire the fluorescence spectrum. However, the use of microscopy techniques was still necessary since the volume fraction of the dense phase is very small, being 20 μl for 1 ml of the total solution volume.

To compare the microscopy results to the bulk reported above the ACDAN fluorescence spectra were corrected for instrumental response using the bulk spectra as a reference. The normalized fluorescence spectrum of the homogeneous phase sample is centred at 490 nm, in line with the data reported in Figure 3.6c). The spectrum is composed of two components; the blue component is centred at about 475 nm, and it is slightly more intense than the green component which is centred at about 500 nm. This results in a positive GP value GP = 0.339 ± 0.008 in line with the GP value reported in Figure 3.7. The concentrated phase spectrum has a higher blue component and a lower green, revealing a lower solvent dipolar relaxation and

a higher molecular order. The GP value for the concentrated is 0.539 ± 0.005. On the contrary the diluted phase spectrum is very similar to the homogeneous phase, indicating that the composition and the order degree of the diluted phase following the LLPS do not differ much from the ones of the homogeneous phase. However, it is possible to observe a slight but significant increase in the green component of the diluted phase with respect to the homogeneous phase. In accordance with this, the calculated GP value for the diluted phase is 0.280 ± 0.014. This can be rationalized as many molecules (both protein and crowding agents) are segregated in the concentrated phase and therefore the molecular crowding and the excluded volume effects are decreased with respect to the initial homogeneous phase. This results in the increase of solvent dipolar relaxation and thus in the decrease of the overall molecular order of the phase.

To explore whether these modifications are detectable by the ACDAN fluorescence lifetime, FLIM measurements were performed on the concentrated phase and diluted phase. The concentrated and the diluted phases are obtained, as explained above, from a sample containing 76 mg/ml PEG and 25 mg/ml BSA, after a centrifugation to separate the two phases. ACDAN fluorescence lifetime has not been explored in any published paper, and only an abstract is available on this topic [164]. Therefore, the results will be interpreted and discussed on the basis of another DAN fluorescent probe, whose lifetime is much more studied, i.e. LAURDAN. LAURDAN is a hydrophobic dye which mainly partitions in the lipid membrane and similarly to ACDAN, it is sensitive to the polarity of its environment and to the dipolar relaxation of water molecules around the LAURDAN molecule. FLIM analysis of LAURDAN fluorescence lifetime, allows disentangling these two properties, evaluating them separately, selecting the detection range properly. The blue channel allows to investigate the polarity effects of the environment and the green channel allows to investigate the dipolar relaxation of water molecules in the proximity of the fluorescent molecule.

In analogy with LAURDAN fluorescence, two acquisition ranges were selected to perform FLIM measurements. The blue channel was set as 430 nm – 460 nm and the green channel was set as 550 nm – 580 nm. FLIM data are analysed by means of the phasor approach, which provides a graphical representation of the data and does not require to impose an a priori model, which on the contrary the fit analysis need. More details on this analysis method are provided in Chapter 2.

In Figure 3.10 the phasor analysis of FLIM measurements on the diluted and concentrated phase in the blue channel is reported. FLIM measurements of homogeneous samples are intended to provide a graphical representation of the data. As
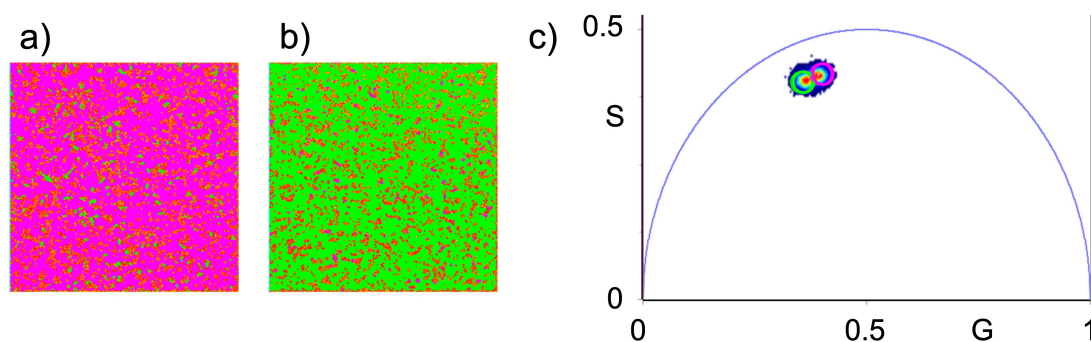
FIGURE 3.10: *FLIM data of ACDAN fluorescence analysed by means of the phasor approach: a-b) phasor maps of the a) concentrated phase and b) diluted phase acquired in the blue channel (430 nm – 460 nm) associated with the polarity of the micro-environment experienced by the ACDAN. c) Phasor plot shows two lifetime distributions that are selected by a magenta and green cursor. The phasor maps are coloured according to the colour of the cursors.*

expected, the images do not show any structure over the diffraction images and only diffused ACDAN fluorescence is observed. Figure 3.10a-b) shows the phasor maps of respectively the concentrated phase and diluted phase obtained from the phasor analysis. In Figure 3.10c) the phasor plot is reported, where it is shown two lifetime distributions (clouds of points), selected by two coloured cursors. The green cursor was used to select the longer lifetime distribution and the magenta was used to select the shorter lifetime distribution. The phasor maps highlight that both the concentrated and diluted phase images are uniformly coloured respectively in magenta and green. This suggests that each phase is homogeneous, as expected, and that ACDAN experiences slightly different polarity within the concentrated and diluted phase. In particular, the diluted phase presents a lower molecular crowding and therefore the water-protein ratio is higher. For these reasons, within the diluted phase (shorter lifetime) ACDAN is expected to experience a more polar environment, with respect to the concentrated phase (longer lifetime). Moreover, if a high contribution of ACDAN fluorescence derives from the ACDAN molecules which sense the hydration of BSA both outside and within the pockets, it is reasonable to assume that ACDAN molecules within the dense phase experience a less polar and more rigid environment. This is in line with the ACDAN spectral red-shift observed within the diluted phase.

Figure 3.11 shows FLIM measurements analysed by phasor on the diluted phase and concentrated phase in the green channel. Figure 3.11a-b) shows the phasor maps of the concentrated and diluted phases respectively. In Figure 3.11c) the phasor plot is reported, showing two well-distinct lifetime distributions. In line with the analysis reported above, the two lifetime distributions are selected by two cursors: the shorter lifetime distribution is selected by a magenta cursor and the longer

lifetime distribution is selected by a green cursor. Looking at the phasor maps is evident that the lifetime distribution selected by the magenta cursor is associated with the concentrated phase (panel a) and the lifetime distribution selected by the green one is associated with the diluted phase (panel b).
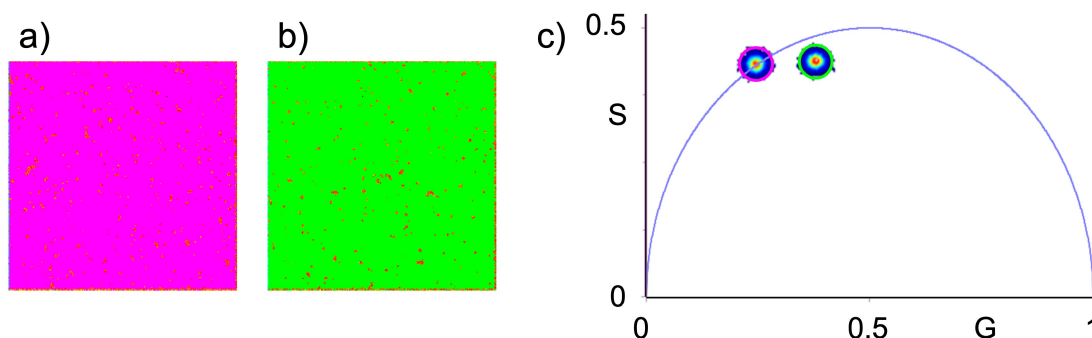

FIGURE 3.11: *FLIM data of ACDAN fluorescence analysed by means of the phasor approach: a-b) phasor maps of the a) concentrated phase and b) diluted phase acquired in the green channel (550 nm – 580 nm) associated with the solvent dipolar relaxation. c) Phasor plot shows two lifetime distributions which are selected by a magenta and green cursors. The phasor maps are coloured according to the colour of the cursors.*

Also in this case, the phasor maps are homogeneously coloured by single colours, denoting that the dipolar relaxation of water is quite different in the two phases. The water dipolar relaxation within the concentrated phase is higher because the environment is more crowded. Moreover, since less water molecules are presented with respect to the BSA molecules, as discussed above, BSA molecules are more dehydrated and the overall environment more rigid. This results in an increase in AC-DAN fluorescence lifetime. In contrary, the diluted phase which presents a shorter ACDAN fluorescence lifetime, shows a higher dipolar relaxation, in line with the data reported in Figure 3.9.

FLIM data for the homogeneous phase were not reported for a higher clarity. However, it is worth mentioning that the ACDAN fluorescence lifetime for the homogeneous phase lies between the concentrated phase data and the diluted phase data, being located nearer the latter, in line with the spectra shown in Figure 3.9a).

3.3 CONCLUSIONS

In this chapter, the liquid-liquid phase separation process of a BSA and PEG solution was investigated. The PEG was used as a crowding agent and the LLPS was induced by thermal effects. The main aim of the study is to explore the role of water in LLPS processes.

The first part of the study focused on establishing the experimental conditions under which LLPS occurs with PEG as the crowding agent. PEG, a widely used polymer, is known for its ability to induce phase separation through volume exclusion effects, which effectively increase the local concentration of proteins by reducing the available volume in the solution. The systematic variation of PEG concentration led to the notable observation that higher concentrations significantly promoted phase separation, consistent with findings in the literature. This was demonstrated by an increase in scattering intensity at lower temperatures, suggesting the formation of BSA-rich coacervates and subsequent phase separation.

In the second part of the study the impact of two ordering and disordering cosolutes were explored. By monitoring the scattering intensity, it was also possible to show the effects of non-ionic kosmotropic, compounds, as glycerol, and non-ionic chaotropic compounds, as ethanol, on LLPS. The reported results showed that Ethanol promotes the LLPS increasing the transition temperature, while glycerol, suppresses the process, acting as a stabilizing agent. This is probably due to the effects of the two compounds on the hydration shell of BSA, but effects due to viscosity and direct interaction with the protein molecules cannot be excluded.

In the third part of the study, the effect of water ordering on LLPS was examined by using the ACDAN dye. ACDAN fluorescence properties allowed us to gain insights into the molecular ordering changes occurring during phase separation. This dye was observed to be sensitive to the LLPS as its fluorescence signal critically changes within the different environments within the concentrated phase (BSA coacervates) and the diluted phase. A global view of the data may also suggest that the ACDAN fluorescence signal could be sensitive to BSA-bound water. By monitoring the fluorescence spectra of ACDAN in solutions of BSA and PEG, we observed significant variations in fluorescence lifetime between the condensed and diluted phases.

Moreover, ACDAN fluorescence lifetime was analysed for the first time by means of phasor approach. In line with what was reported for LAURDAN fluorescence, FLIM measurements were acquired in two detection ranges. By means of this method, it was possible to disentangle the two factors which affect its fluorescence, being polarity and solvent dipolar relaxation. Overall, the diluted phase was observed to be more polar and with a higher dipolar relaxation with respect to the concentrated phase.

This method will allow for a qualitative exploration of water dynamics in highly crowded environments, without the risk of experimental artefacts arising from changes in medium polarity. Furthermore, it is our future interest to investigate the LLPS

process of other globular proteins, characterized by different conformations and structures to study the behaviour of ACDAN in different experimental conditions, with a lower protein affinity. This could potentially make ACDAN even more sensitive to subtle changes in water. This comprehensive investigation contributes to a deeper understanding of the molecular mechanisms underlying LLPS in protein solutions, by elucidating the roles of crowding agents and water dynamics. Understanding the significance of water ordering is crucial as it provides another piece to the puzzle of LLPS. Additionally, this enables easy tuning of LLPS for potential biomedical applications, as biosensing.

3.4 SAMPLE PREPARATION AND PARAMETERS USED FOR MEASUREMENTS

3.4.1 SAMPLE PREPARATION

Stock solutions of 50 mg/ml BSA and 500 mg/ml PEG 4000 (purchased by Sigma-Aldrich) were prepared in 100 mM acetate buffer (pH 4.6). Upon 1:10 dilution of the BSA stock, BSA concentration was measured by UV – Vis spectroscopy by means of a Jasco – V770 spectrophotometer using the molar extinction coefficient $\epsilon = 0.667$ ml cm^{-1} mg^{-1} at 280 nm. Sample is prepared mixing BSA and PEG at room temperature to reach the same desired concentration: 25 mg/ml BSA and PEG concentration may vary between 60 mg/ml and 76 mg/ml. Sample is always prepared by adding the buffer, PEG 4000 and BSA in this order. Before adding BSA to the mixture, PEG and buffer are mixed until the solution is homogeneous.

For the chaotropic and kosmotropic experiments, 50% (v/v) glycerol and 20% (v/v) EtOH stock solution were prepared in the same acetate buffer and then added to the sample at the desired concentration (EtOH final concentration ranges between 1% - 4% (v/v) and glycerol final concentration ranges between 2% - 8% (v/v)).

For ACDAN experiments in bulk, ACDAN is added to a final concentration of 30 μm. The concentrated and the diluted phases are obtained from a sample containing 25 mg/ml BSA, 76 mg/ml PEG 4000, 30 μm ACDAN in 100 mM acetate buffer (pH 4.6). The two phases were physically separated by centrifugation of this sample ($10^4 \times$g for 10 min at 20°C). The homogeneous phase consists of a sample containing 25 mg/ml BSA, 76 mg/ml PEG 4000, 30 μm ACDAN in 100 mM acetate buffer (pH 4.6).

3.4.2 SCATTERING MEASUREMENTS

Scattering measurements were acquired using a Jasco-FP-8500 spectrofluorometer equipped with a Jasco ETC-815 peltier as temperature controller. The acquisition range is 630 nm – 670 nm and the excitation wavelength is 650 nm to monitor Rayleigh scattering. A 1 cm path length quartz cuvette. The response time was set to 1 s, data interval to 0.1 nm, scan speed to 100 nm/min, and excitation and emission bandwidths to 2.5 nm. Spectra were acquired at each decree Celsius during a temperature ramp of 15°C/hour.

3.4.3 ACDAN FLUORESCENCE MEASUREMENTS IN BULK

Fluorescence spectra in bulk were acquired using a Jasco-FP-8500 spectrofluorometer equipped with a Jasco ETC-815 peltier as temperature controller. ACDAN fluorescence spectra were acquired in 1 cm path length quartz cuvettes. The response time was set to 1 s, data interval to 0.5 nm, scan speed to 100 nm/min, and excitation and emission bandwidths to 2.5 nm. The acquisition range is 380 nm – 650 nm and the excitation wavelength is 390 nm. Spectra were acquired at each decree Celsius during a temperature ramp of 15°C/hour.

3.4.4 2PM MEASUREMENTS

The experiments were performed using a Leica TCS SP5 confocal laser scanning microscope, with a 63×/1.40-0.60 oil objective, and a scanning frequency of 400 Hz (Leica Microsystems, Germany). ACDAN fluorescence was excited at 780 nm (Spectra-Physics Mai-Tai Ti:Sa ultra-fast laser). All the images were acquired at a resolution of 1024 × 1024 pixels and the detection range was 450 – 600 nm. The fluorescence spectra were permed acquiring 256 × 256 pixels and the detection range was 400 – 650 nm. The fluorescence spectra were acquired in the same range with a 15 nm bandwidth and 5 nm step size. The analysis of the microscopy data was performed by the open-source software ImageJ Fiji (https://imagej.net/software/fiji/).

3.4.5 FLIM DATA ANALYSED BY PHASOR APPROACH

FLIM measurements were acquired in the time domain by means of a Leica TCS SP5 confocal laser scanning microscope coupled with picoHarp 300 TCSPC module (Picoquant, Germany). 256 × 256 pixels FLIM images were collected with a 63×/1.4 oil objective and scanning frequency 400 Hz. ACDAN fluorescence was excited at 780 nm (Spectra-Physics Mai-Tai Ti:Sa) in two channels: 430 – 460 nm

(blue channel) and 550 – 580 nm (green channel) FLIM analysis was performed by the SimFCS4 software developed at the Laboratory of Fluorescence Dynamics, University of California at Irvine (http://www.lfd.uci.edu). The fluorescence lifetime of Alexa 405 (τ = 3.6 ns, single exponential) was used to calibrate FLIM data in the blue channel. The fluorescence lifetime of fluorescein (τ = 4 ns, single exponential) was used to calibrate FLIM data in the green channel.

CHAPTER 4

Liquid-Liquid Phase Separation mediated by surfaces in microscale aqueous compartments

---

In this chapter results on the supramolecular self-assembly of Human Insulin (HI) within sub-microliter aqueous compartments cast on a glass coverslip are shown. This process leads to the formation of spherical HI microparticles, which are formed from fixed nucleation points at the water-glass surface around which HI molecules condensate. This peculiar supramolecular assembly process leads to the formation of hybrid structures with a solid dense core and a liquid-like corona. The first part of the study focuses on the analysis of the morphology of these newly formed microparticles. In the second deals with the formation kinetics of the microparticles, exploring the nucleation mechanism. Finally, in the third part the effect of the compartment size is investigated, showing how this is a crucial factor regulating the entire process. This study has revealed a new process of supramolecular association of insulin that cannot be observed at volumes above the microliter scale. To achieve this, an experimental setup was developed that allows for the creation of stable aqueous compartments in a hemispherical shape injected into an oil droplet over a glass coverslip. The experimental approach design allows for quantitative fluorescence microscopy experiments, providing the capability to track the evolution of the process in real-time, define the physical state of the particles, and determine the molecular structure with pixel resolution.

4.1 INTRODUCTION

In the presented study HI is used as a model protein to study. This choice is motivated by the extensive number of articles in the literature that have investigated a plethora of different aggregation mechanisms, particularly in the field of amyloid formation. HI is a peptide hormone composed of two polypeptide chains, an A chain with 21 amino acids and a B chain with 30 amino acids, linked by disul-

fide bonds. It adopts a secondary structure characterized by an α-helix in the A chain and a β-sheet conformation in the B chain. HI monomers can organize into dimers, tetramers, and hexamers depending on solution conditions at room temperature. Under the conditions of this experiment, HI remains in monomeric form. This makes it less stable and more prone to self-assembly.

It is known that HI forms amyloid aggregates at acidic pH, high salt concentrations, and high temperatures (above 60°C). The study of HI aggregation process was widely conducted in bulk with typical volumes from tens or hundreds of microliters up to millilitres at temperatures well [87, 121, 165]. Under these conditions, the formation of amyloid fibrils and superstructures like spherulites has been extensively investigated. After aggregation, HI samples are extremely heterogeneous with variations on the nano, micro, and mesoscales. For this reason, recent studies on HI aggregation have employed optical microscopy techniques, such as confocal laser scanning fluorescence microscopy, Fluorescence lifetime imaging microscopy (FLIM) and Fourier Transform Infrared (FTIR) microscopy to highlight structural and morphological spatial heterogeneity of the aggregates at different space scale level [28]. As reported in the introduction insulin may form amyloid structures that self-assemble in higher-order assemblies at a macroscopic or mesoscopic scale They may occur in various forms and sizes, including elongated fibrils, homogeneous spherical microparticles (particulates), and core-shell superstructures with a dense, amorphous core surrounded by a fibril-like corona (spherulites). Notably, it was reported by numerous studies that insulin aggregation can be promoted by the presence of solid hydrophobic surfaces [128, 129, 130, 131]. Surfaces are reported to promote monomer conformational changes supporting the aggregation rate at interfaces. In particular, this effect was found to be obtained when the solid surface is hydrophobic.

In this study, we demonstrate a process driven by Liquid-Liquid Phase Separation (LLPS), coupled with a liquid-to-solid phase transition, leading to the spontaneous formation of amyloid-like self-assemblies at room temperature. The chosen experimental conditions allow for the observation of the supramolecular assembly process within aqueous compartments ranging from nanolitres to hundreds of nanolitres. Monodisperse spherical particles with amyloid properties form at the solution-glass interface through homogeneous nucleation, originating from a spatially heterogeneous distribution of similar nuclei. These structures exhibit a solid core and a liquid-like corona, displaying characteristics that lie between protein particulates and spherulites.

Using quantitative fluorescence microscopy techniques, we elucidated the dif-

ferent phases of these unique supramolecular assemblies. Employing Thioflavin T (ThT), a standard fluorescent marker in amyloid research, we investigated the formation and growth of aggregates within sub-microliter compartments. Analysis of ThT fluorescence lifetime using the phasor approach revealed distinct structural characteristics of the newly formed species. Coupled with FRAP experiments, this method allowed us to thoroughly describe the entire process, highlighting homogeneous primary nucleation as a fundamental step in the formation. This study emphasizes the impact of surface-to-volume ratio on LLPS-driven processes within microscale compartments at interfaces, revealing a supramolecular assembly phenomenon that remains undetected in large-scale samples.

4.2 Experimental results and discussion

4.2.1 Morphology of the insulin microparticles

Figure 4.1 illustrates a three-dimensional schematic side-view representation of the experimental setup. An aqueous solution drop (depicted as a light green hemisphere) was injected into a $100\,\mu$l mineral oil drop (depicted as a grey hemisphere) cast on a microscopy-grade glass coverslip. The aqueous solution has a sub-microliter volume. At the water-oil interface, yellow molecules are drawn to depict Tween-20, a surfactant, used to stabilize the oil-water interface. Human Insulin microparticles (shown as bright green hemispheres) grow on the interface between the glass coverslip and the aqueous drop. The sample comprises 5 mg/ml Human Insulin in a 20% Acetic acid solution (pH 1.85), 0.5 M NaCl, and 0.05% Tween 20.
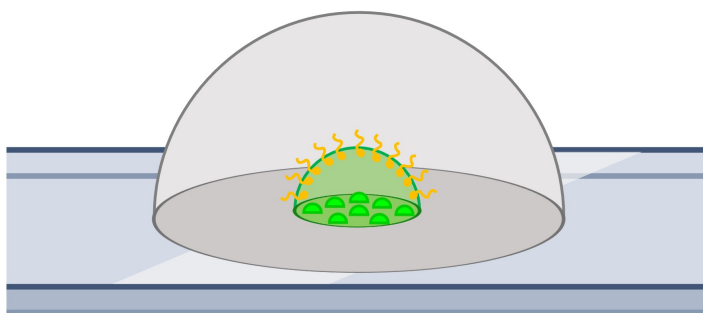

FIGURE 4.1: *Three-dimensional side-view representations (not in scale) of the experimental setup diagram: an aqueous solution drop (depicted as a light green hemisphere) is injected into a mineral oil drop (grey hemisphere) cast on a glass cover slip. Protein microparticles grow at the bottom of the aqueous drop (small bright green hemisphere within the aqueous drop). The interface between the aqueous drop and the oil is stabilized by the surfactant Tween-20, depicted as yellow molecules at the water-oil interface.*

The use of this experimental setup allows to monitor the formation and the

71

growth of Human Insulin microparticles, within sub-microliter volume aqueous drop. By means of quantitative fluorescence microscopy techniques, it was possible to analyse the self-assembly process in real-time and at pixel-size spatial resolution.

As mentioned above, Tween 20 is a non-ionic water-soluble amphiphilic compound. Being an amphiphilic molecule, at a concentration above the critical micelle concentration (0.09 mM in water at 25°C [166]), tween 20 self-assembles into micelle. It was previously reported that tween 20 places at the water-oil interface, resulting in the formation of stable water compartments within the oil, characterized by a well-defined shape, preventing any water-in-oil leakage.

In Figure 4.2 six images of six distinct samples prepared on different days are reported. The images are 1024×1024 pixels two-photon microscopy fluorescence images of the HI microparticles stained by ThT. The excitation wavelength is λ_{exc} = 780 nm, and the detection range is 450 – 600 nm. The microparticles are obtained by incubating 5 mg/ml HI in a 20% acetic acid solution (pH 1.85), 0.5 M NaCl, 0.05% w/v Tween 20, and 40 μM ThT at room temperature for approximately 5 hours. Moreover, these microparticles grow at the bottom of the aqueous drops at the water glass interface. During the whole formation kinetics, the rest of the aqueous drops remain empty and no aggregates form elsewhere. After their formation, the microparticles remain stable for several days, exhibiting the same fluorescence intensity without significant modifications. The aqueous drop shown in Figure 2 presents very similar diameter sizes, ranging from 250 μm (panel f) to 270 μm (panel e). The remaining drops have a diameter of 260 μm. From now on, whenever the size of a drop is mentioned, it will refer to the diameter of the drop.

Figure 4.2 highlights the composition and the reproducibility of the sample. Within each drop, the microparticles are randomly scattered across the surface and the microparticles are homogeneous in size and shape. The microparticles appear to be positive to ThT indicating that they present an amyloid-like structure. Comparing the drops, it is possible to infer that the microparticles present the same spherical shape and similar sizes (few micrometres), having nevertheless some variability. For instance, it is evident how the microparticles in Figure 4.2e) are slightly smaller than the microparticles in Figure 4.2a-b). On the other hand, the microparticles in Figure 4.2f) are slightly larger. Moreover, the number of microparticles is not always the same, showing a similar variability. In particular, it is noticeable how drops with smaller microparticles have a higher number of them and vice versa (panels e and f respectively). Therefore, the number and the size of the microparticles seem to be linked. This aspect will be discussed later in this chapter. Another notable feature is the ring which appears at the edge of some drops, see images c)
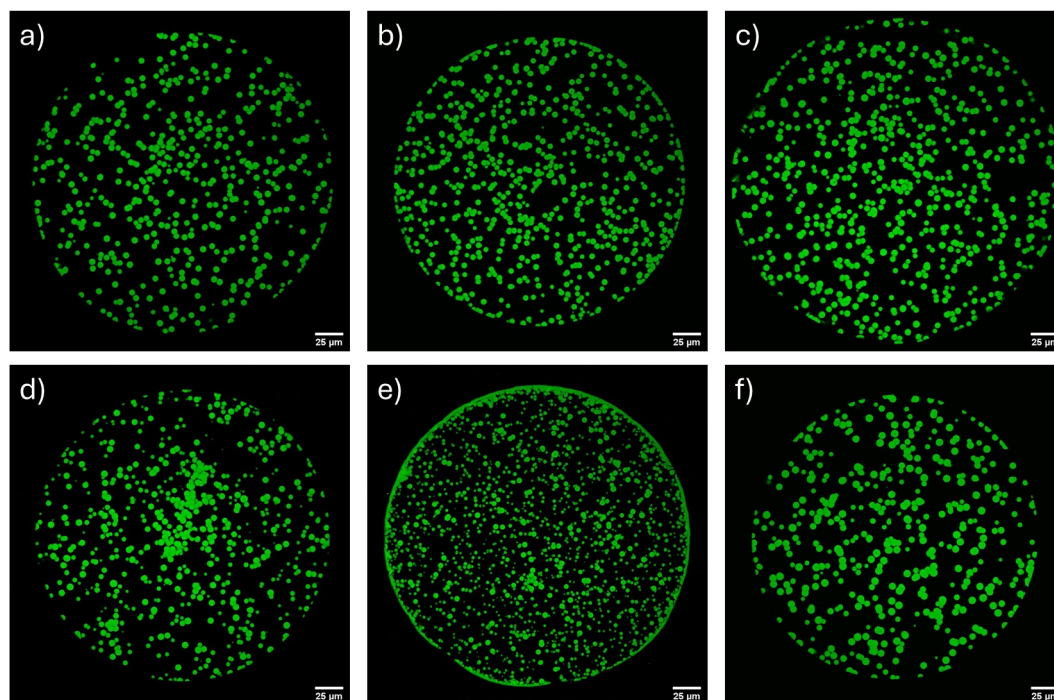
FIGURE 4.2: *a-f) 1024×1024 pixels representative two-photon microscopy fluorescence images of the sample. The HI microparticles form by incubating 5 mg/ml HI in a 20% acetic acid solution (pH 1.85), 0.5 M NaCl, 0.05% w/v Tween 20, and 40 μM ThT at room temperature for approximately 5 hours. The microparticles occur at the bottom of the drop at the water-glass interface. The HI microparticles are positive to ThT staining and present the same spherical morphology. The number and the size of microparticles are similar but they present a variability. The sizes of the drops range from 250 μm to 270 μm. Scale bar is 25 μm.*

and e) as reference. This is due to the agglomeration of microparticles which occurs at the triple interface water-glass-oil, which could favour their formation. The ring effect seems to be related to the number of particles, specifically, it occurs in drops wherein higher number of particles form. This phenomenon could be also affected by the Marangoni flow which is the movement of fluid caused by gradients in surface tension along an interface between two fluids. Marangoni flow was observed to be responsible for the formation of a ring at the edges of water drop in oil [167]. Marangoni flow could therefore cause the movement of insulin molecules or nucleation sites at the triple interface.

To obtain investigate details of HI microparticles, images at higher spatial resolution were acquired. Figure 4.3a-c) are 1024×1024 pixels representative two-photon microscopy fluorescence images of the HI microparticles in different aqueous drops in the same experimental conditions. The images were acquired at increasing spatial resolution. Figure 4.3d) shows the ThT fluorescence intensity profile measured at the yellow dashed line drawn in panel c). Reported data are smoothed to highlight the average trend of the data, increasing the signal-to-noise ratio. Fig-
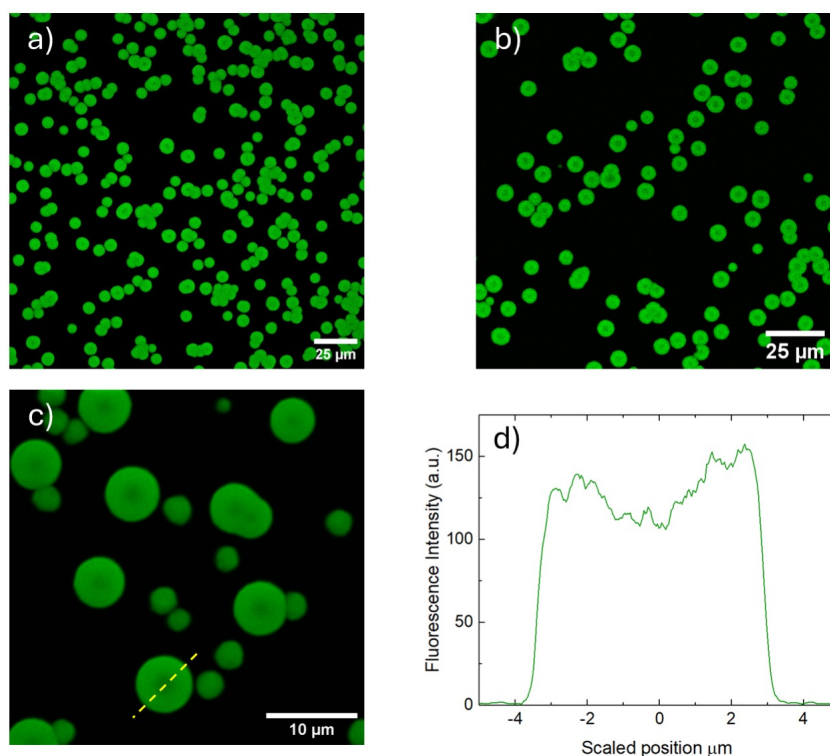
FIGURE 4.3: *a-b) 1024×1024 pixels representative two-photon microscopy fluorescence images of the HI microparticles formed by incubating 5 mg/ml HI in a 20% acetic acid solution (pH 1.85), 0.5 M NaCl, 0.05% w/v Tween 20, and 40 µM ThT at room temperature. ThT fluorescence intensity tends to be lower at the central region of the microparticles. c) Two-photon microscopy fluorescence image of analogous samples in repeated experiments at higher spatial resolutions. The HI microparticles exhibit a darker ThT fluorescence spot at the central region of each microparticle. The longitudinal axis of a microparticle is represented by a yellow dashed line. d) ThT fluorescence intensity profile measured at the yellow line in panel c). Data show the decrease in ThT fluorescence intensity at the central region of the microparticle.*

ure 4.3a-c) reveals that ThT fluorescence intensity is not homogeneous within the single microparticle and in particular tends to be lower at the central region of the microparticles. To quantify the ThT fluorescence reduction within the microparticles, the intensity profile of a microparticle was reported in Figure 4.3d). From the data it is evident how the central region of the microparticle exhibits a fluorescence intensity decrease of about 25% with respect to the edges. Moreover, it was observed that this darker is well localized at the core of these structures because it is not visible if the image is acquired at the equatorial plane of the microparticles (data not shown). The reduction of ThT fluorescence intensity in the central region of the can be ascribed to different factors: the presence of a hollow cavity within the microparticles, restricted accessibility of ThT molecules to the inner regions, or a low affinity of ThT for the core of the microparticles. In a previous study, we observed a similar feature for Insulin spherulites, which exhibit a low ThT fluorescence intensity at the core. By means of the combination of fluorescence microscopy and

Micro-FTIR, we were able to correlate this fluorescence intensity reduction with a lower density of amyloid structure and therefore a high density of native-like protein in the core of these spherulites [28].

Unfortunately, Micro-FTIR is not adequate to analyse this system because this technique has a poor spatial resolution (tens of micrometres) and the sizes of the microparticles are smaller, with an average of about 5 μm. Therefore, to further investigate the fluorescence decrease at the core of the microparticles, it was decided to exploit the Fluorescence Recovery After Photobleaching (FRAP). This technique provides information on the mobility of fluorescent molecules within a sample. Consequently, FRAP also provides information on the physical state of a sample. To perform FRAP experiments, HI molecules covalently labelled with Alexa 647 (from now on HI647) were added to the solution. The concentration of HI647 is 80 nM. The molar ratio between the labelled molecules and the unlabelled molecules results in about 1:10^4. Analogous experiments to the one previously described were conducted, resulting in the formation of the microparticle with a double staining.

Figure 4.4 shows representative CLSM fluorescence images of HI microparticles obtained incubating the same HI solution used for the previous freshly prepared with the addition of HI647. The images were acquired in two channels: the green channel (Figure 4.4a, d) showing the ThT fluorescence signal (λ_{exc} = 470 nm, detection range = 485 – 585 nm) and the red channel (Figure 4.4b, e) showing HI647 fluorescence signal (λ_{exc} = 633 nm, detection range = 650 - 750 nm). In Figure 4.4c, f the merged images of the two channels are reported. The merged images show the fluorescence of ThT and HI647 in the same colour code. Figure 4.4) shows that the same spherical microparticles occur at the water-glass interface on the same time scale.

In Figure 4.4 a, d) the ThT fluorescence images report the same structure already described above. ThT staining allows the detection of spherical microparticles with an average diameter of about 5 μm, which exhibit a lower fluorescence intensity in the central region. Contrarily, the intensity of HI647 fluorescence showed in Figure 4.4b, e) is higher in the central region of the microparticles. It is reasonable to think that the fluorescence intensity of HI647 is proportional to the number of fluorescent molecules. Alexa 647 is a dye which is part of a family of synthetic fluorescent probes, which are very photostable and insensitive to many environmental changes [168, 169]. This observation suggests that HI molecules accumulate within the core of the microparticles. The microparticles have therefore a heterogeneous structure, having a higher density at the core of the microparticles, and decreasing radially
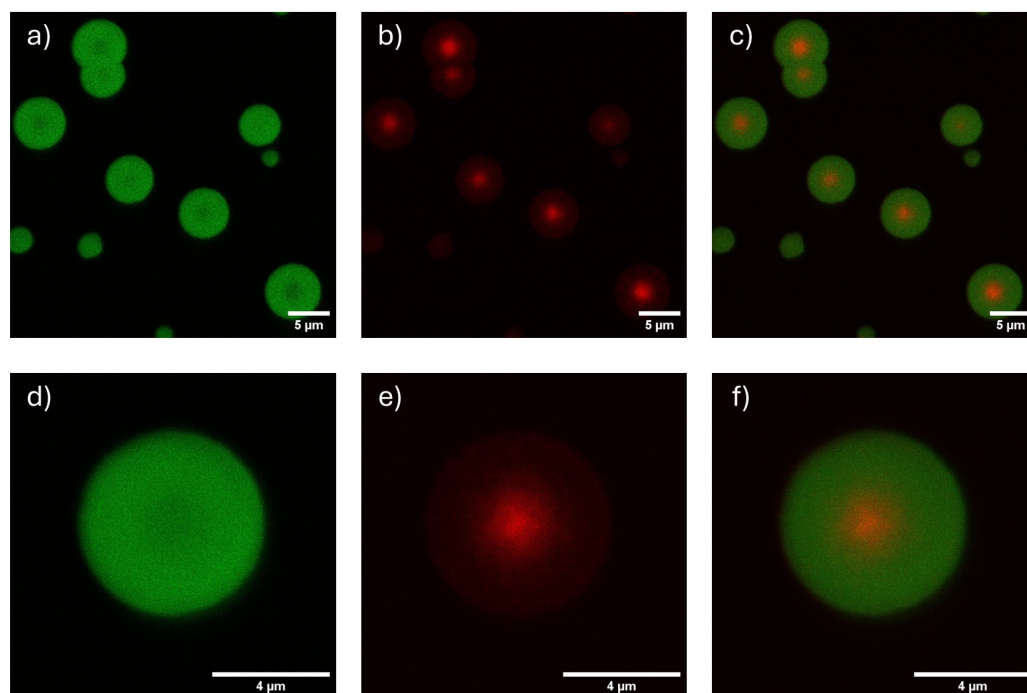
FIGURE 4.4: *(a-f) 1024×1024 pixels representative fluorescence confocal microscopy images of HI microparticles acquired in two channel. The microparticles were obtained incubating overnight at room temperature 5 mg/ml HI and 80 nM HI labelled with Alexa 647 (HI647) in a 20% Acetic acid solution (pH 1.85), 0.5 M NaCl, 0.05% Tween 20 and 40 μM ThT solution in a 300 μm (a-c) and 330 μm (d-f) aqueous drop. The molar ratio between labelled HI molecules HI647 and unlabelled HI molecules is 1:10⁴. a, d) Green channel showing the ThT fluorescence (λ_{exc} = 470 nm, detection range = 485 – 585 nm). b, e) Red channel showing HI647 fluorescence (λ_{exc} = 633 nm, detection range = 650 - 750 nm). c, f) Merged images showing the fluorescence of ThT and HI647 in the same colour code.*

towards the edges. Moreover, from Figure 4.4c, f) it is possible to observe that there is a spatial overlapping of the region where the ThT fluorescence is lowered and the region where high HI647 fluorescence intensity is detected.
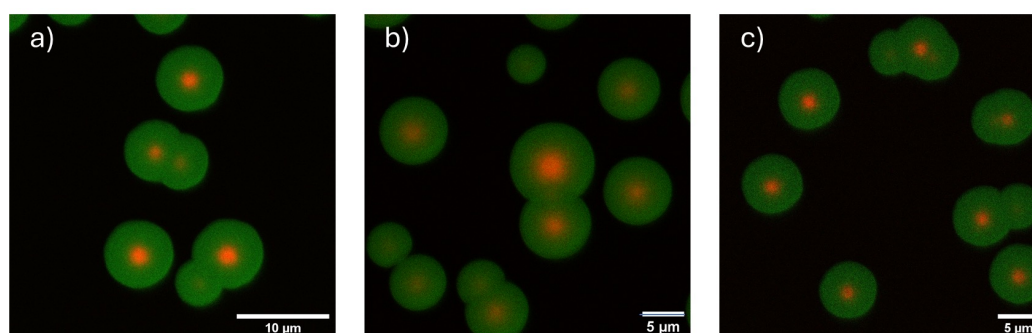

FIGURE 4.5: *(a-c) 1024×1024 pixels representative fluorescence confocal microscopy images of HI microparticles. The microparticles were obtained incubating overnight at room temperature HI and HI647 at the same solution conditions of the experiment described above in a 300 μm aqueous. The images are the merged images acquired in the green (ThT fluorescence, λ_{exc} = 470 nm, detection range = 485 – 585 nm) and red (HI647 fluorescence, λ_{exc} = 633 nm, detection range = 650 – 750 nm) channel.*

This feature is common to each HI microparticles in all the prepared samples, as shown by the Figure 4.5, wherein three representative fluorescence CLSM images are reported, showing the microparticles which occur in three distinct aqueous drops of about 300 μm. The samples are prepared incubating overnight at room temperature HI and HI647 at the same solution condition of the previous experiment. The images are the result of the merging of the green and the red channels images. All the microparticles present a bright red region at their respective core which is the fluorescence signal of the HI647.

FRAP experiments were performed on several HI microparticles in different aqueous drop. Microparticles were photobleached in two regions of interest (ROIs), the core and the edges, to study if the difference in density implies a diverse physical state of the microparticles. Figure 4.6 shows six representatives 256×256 pixels images, acquired by CLSM. The images are acquired in the red channel, displaying the HI647 fluorescence (λ_{exc} = 633 nm, detection range = 650 – 750 nm). In Figure 4.6a-c) the ROI wherein FRAP experiment is performed, is at the core of the microparticle, while in Figure 4.6d-f) the ROI is at the edges of the microparticle. The size of the ROIs ranges from 2 μm and 2.5 μm. The initial state of the microparticle is reported in Figure 4.6a, d). As described above, the HI647 fluorescence intensity decreases going from the core towards the edges of the microparticles. Figure 4.6b, d) shows the microparticles after the photobleaching of the respective ROIs. The photobleaching process was set to last 30 seconds. The ROIs appear as a dark region within the microparticles. FRAP results are reported in Figure 4.6c, f). In Figure 4.6c) the ROI present an increase of fluorescence intensity, but it is still well-visible, while after the same time interval, the ROI at the edges in Figure 4.6f) regained most of the fluorescence intensity measured before the photobleaching. This indicates that the mobility of HI within the microparticles is different depending on the region.

To quantify the results of the FRAP experiments the fluorescence intensity is monitored within the ROIs. Each microparticle was photobleached both at the core and at the edges in ROIs of similar size. Whether the photobleaching process occur first at the core or at the edge of the microparticles, the obtained results are the same. In Figure 4.7 FRAP results on different HI microparticles are reported. The fluorescence intensity recovery is reported as a function of time. Four different plots are reported to highlight the repeatability of the experiments. The fluorescence intensity measured in the core of the microparticles is reported as red squares, and in the edge is reported as green circles. The fluorescence intensity is normalized to the initial fluorescence intensity value within the respective ROI before the bleach-
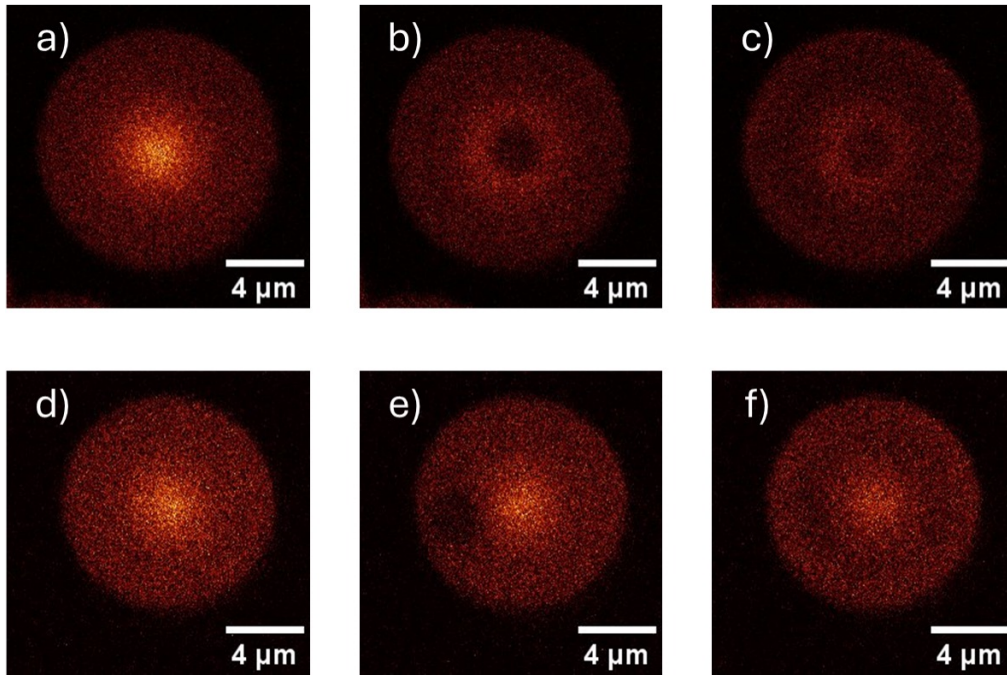
FIGURE 4.6: *FRAP on HI microparticles obtained in the same experimental conditions of the previous experiments. during a FRAP experiment. The images are 256×256 pixels and were acquired in the red channel by fluorescence confocal microscopy (HI647 fluorescence, λ_{exc} = 633 nm, detection range = 650 – 750 nm). The photobleaching process is performed at the core a-c) and at the edge d-e) of the microparticles. a, d) Microparticles before FRAP experiment. b, e) Microparticles after undergoing photobleaching in small ROIs for 30 seconds. The ROIs appear as dark regions within the microparticles because the fluorescence intensity decreased. c, f) After 80 seconds the fluorescence has partially recovered: in c) the ROI where the photobleaching process occurred is still visible, while in f) the ROI is almost invisible.*

ing. The initial value is obtained as the average of three images acquired before the FRAP experiments are performed. The fluorescence intensity recovery reaches an equilibrium after about 80 seconds. As can be observed, after photobleaching, the fluorescence intensity signal measured at the edge of the microparticles (green circles) increases to a plateau within approximately 80 seconds. The signal recovery reaches about 60% of the initial signal, indicating an immobile fraction of about 40%. Conversely, the fluorescence intensity recovery detected in the ROI at the core of the microparticles is below 10%, indicating an immobile fraction of 90% or above.

These observations suggest that the observed HI microparticles consist of a central compact core where proteins are in an immobile, solid state, surrounded by a region with greater mobility where HI molecules can diffuse in a fluid-like matrix. The solid core at the centre of the protein condensates exhibits lower affinity for ThT, indicating a different molecular structure compared to the external part. This is similar to what has been previously reported for HI spherulites formed at high temperatures in bulk experiments. The fluid-like state of the outer region, com-
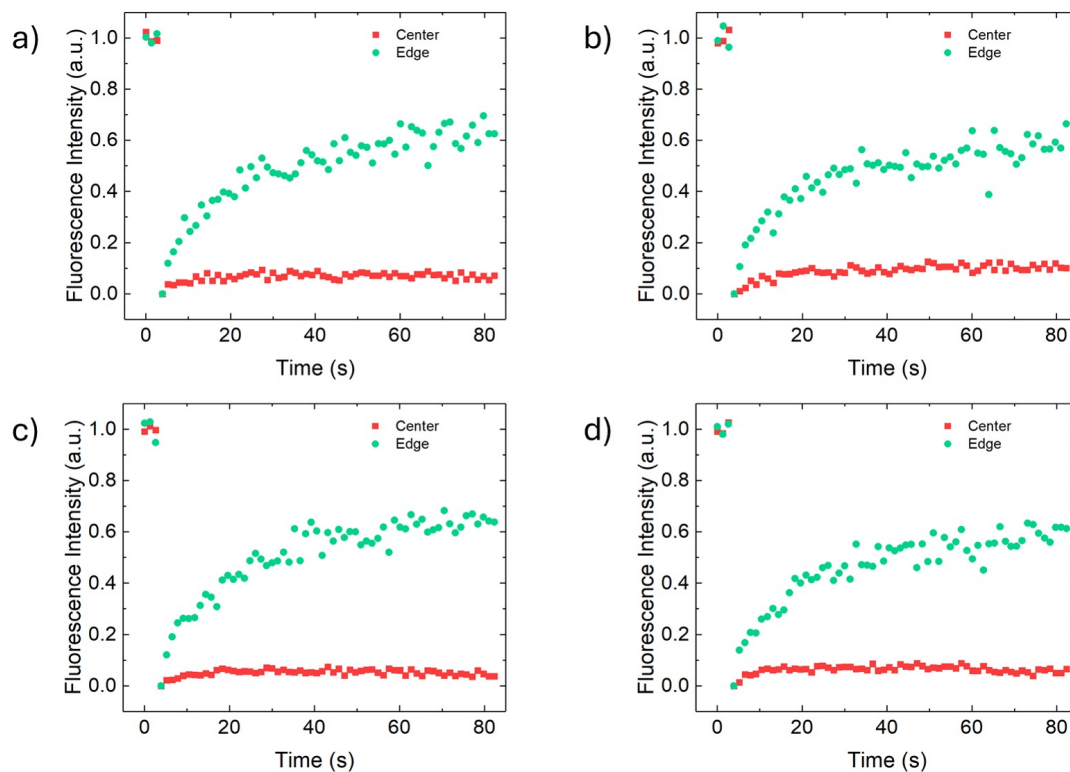
FIGURE 4.7: *FRAP experiments on different HI microparticles. For each microparticle the 'FRAP experiments were performed at two ROIs: the edges, showed in green, and the core showed in red. Fluorescence intensity was monitored within the ROIs. Fluorescence intensity is normalized to its value within the ROIs before the FRAP experiments start. After 80 seconds the fluorescence reached about 60% of its initial value at the edge of the microparticle, while at the core the fluorescence recovery is under 10%.*

bined with the spherical shape of these microparticles, suggests that liquid-liquid phase separation is the underlying mechanism for the formation of these liquid-like condensates with a solid core.

4.2.2 FORMATION AND EVOLUTION OF SUPRAMOLECULAR ASSEMBLIES

It is possible to follow and analyse the formation of the HI microparticles within aqueous drop at pixel size spatial resolution, by collecting images at regular time intervals after the drop deposition. Representative two-photon microscopy images showing the main events of the microparticles' formation process in a 260 μm are reported in Figure 4.8. In the first phase (145 min), no significant ThT fluorescence is detected, indicating the lag phase of the process. After about 170 min from the drop deposition, ThT fluorescence intensity starts to grow from small and fixed points on the water–glass interface that appear almost simultaneously (within 10 – 15 minutes). These fixed points are the nucleation sites from which the HI microparticles grow and they correspond to the solid native-like core of the micropar-

ticles/condensates. Afterwards, ThT fluorescence intensity increases exponentially, and the microparticles increase their size, growing radially. When the equilibrium is reached, the microparticles stop growing and the ThT fluorescence intensity remains constant over time. Within the spatial resolution of the measurements, no diffusion of the nucleation sites or of the mature microparticles is detected.
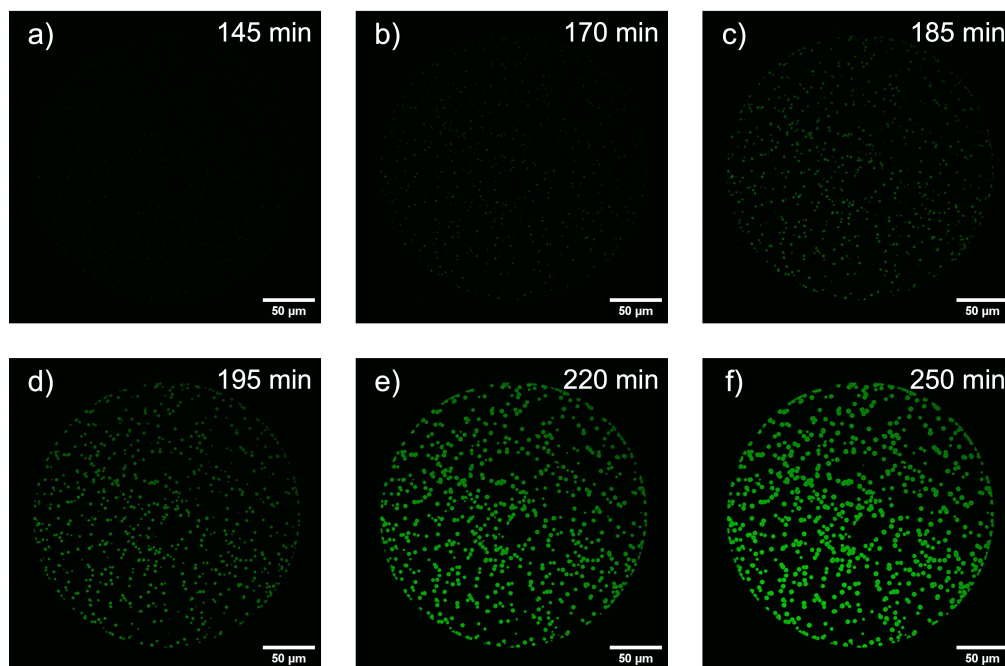

FIGURE 4.8: *Representative two-photon microscopy images of the main events occurring during the formation of the microparticles, obtained incubating 5 mg/ml HI in a 20% Acetic acid solution (pH 1.85), 0.5 M NaCl, 0.05% Tween 20 and 40 μM ThT at room temperature for about 6 hours in a 260 μm aqueous drop. Images at different time points are shown: a) 145 min, b) 170 min, c) 185 min, d)195 min, e) 220 min, and f) 250 min.*

By measuring the ThT fluorescence intensity over time it is possible to acquire quantitative information about the time evolution of the HI self-assembly. Through the use of fluorescence microscopy techniques, the ThT fluorescence kinetics may be monitored in different regions of the sample, including the whole aqueous drop, single microparticles or even within single particles, with a spatial resolution limited only by the pixel size. This approach allows for a detailed examination of how ThT fluorescence evolves at different spatial scales throughout the assembly process.

Figure 4.9 shows ThT fluorescence kinetics measured during the formation of the microparticles shown in Figure 4.2d). ThT fluorescence kinetics is obtained using as ROI the whole drop a) and twenty different HI microparticles, within the same aqueous drop b). The reported kinetics have a sigmoidal profile, which is typical of the nucleated process. This was expected since it was observed in the previous image that the microparticles grow from fixed nucleation points. The ThT

kinetics presents a lag phase which lasts about two hours, followed by a growth phase where ThT fluorescence increases rapidly. Finally, after about four hours the ThT reaches a plateau region which is the equilibrium phase.
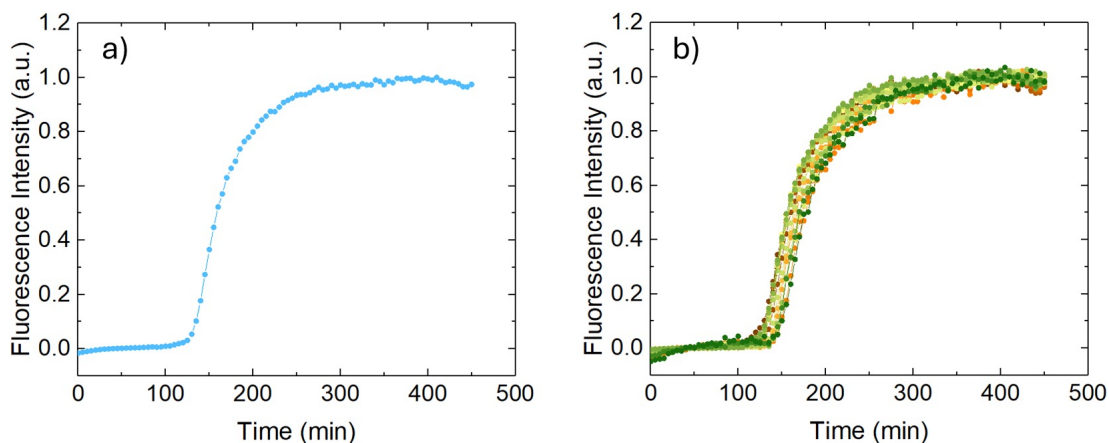

Figure 4.9: *Normalized ThT fluorescence intensity versus time. The kinetics present a sigmoidal profile. The fluorescence data are obtained by the integration of the value of every pixel within the ROI, neglecting the one with a value under 5, to eliminate the contributions of free ThT in solution. ThT fluorescence kinetics is measured taking as ROI a) the whole aqueous drop shown in Figure 4.2d) and b) twenty different microparticles within the same drop.*

ThT fluorescence intensity was measured by integrating the intensity value of every pixel within the ROI. To eliminate the contribution of unbound ThT molecules in solution, all the pixels with an intensity value below than 5 were neglected. ThT fluorescence intensity is normalized to the maximum intensity value reached by the sample at the equilibrium phase. The ThT fluorescence kinetics measured in the single microparticle present the same shape but also slight variabilities of the microparticle kinetics. Specifically, a small difference in the lag phase duration is detectable and it is due to the fact that the nucleation points do not appear perfectly at the same time but within 15 minutes, as mentioned above. As it is evident the ThT fluorescence kinetics measured in the whole drop (a) and the kinetics measured in single microparticles (b) are perfectly overlapped, indicating the ThT fluorescence intensity increase parallels the growth of the microparticles. This denotes an ergodic behaviour of the entire process and suggests that the mechanism underlying the formation of the microparticle is a homogeneous nucleation mechanism.

Figure 4.10a) shows a 1024×1024 pixels two-photon microscopy fluorescence image of HI microparticles in a 260 μm aqueous drop. The image was acquired after an overnight incubation at room temperature. Magnified areas of the same sample are reported in Figure 4.10b-c). The ROI where ThT fluorescence spectrum was measured over time are highlighted by red circles. The ThT fluorescence kinetics are reported in Figure 4.10d) for the whole drop, in panel e) for the single

microparticles, and in panel f) a spot within the microparticle. Fluorescence intensity is normalized to its final value after it reaches the equilibrium. Similarly to the kinetics reported in Figure 4.9, ThT kinetics have a sigmoidal profile, featuring a lag phase of about two and a half hours. Afterwards, a growth phase which lasts for 100 minutes, followed by the equilibrium phase.
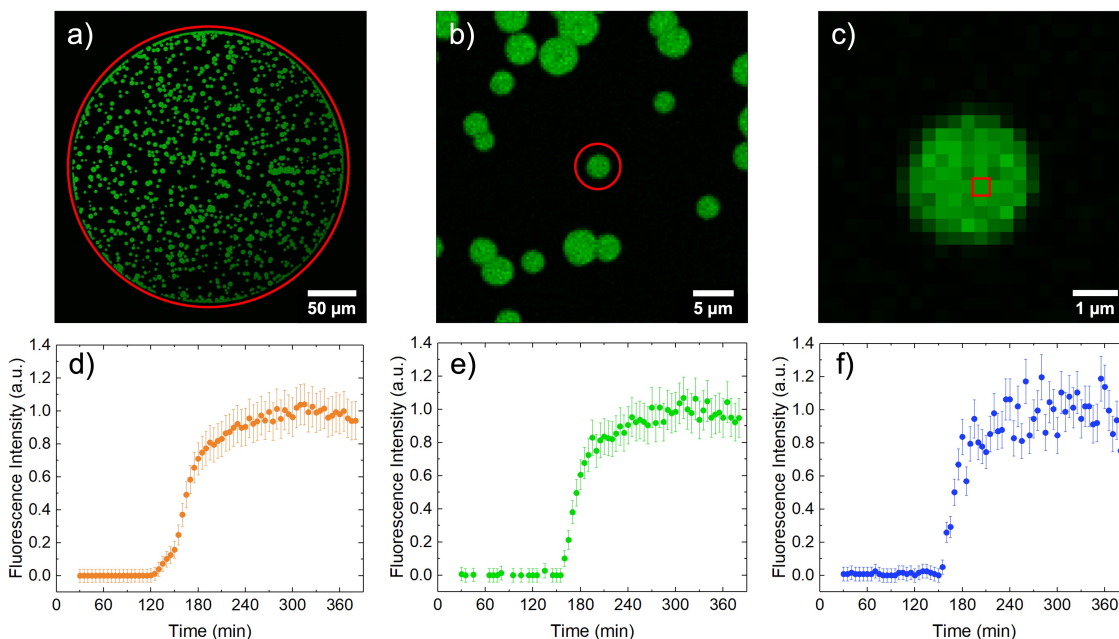

FIGURE 4.10: *(a) 1024×1024 pixels two-photon microscopy fluorescence image of HI microparticles within a 260 μm aqueous drop stained by ThT (λ_{exc} = 780 nm, detection range = 450 - 600 nm). Scale bar is 50 μm. The HI microparticles are obtained as usual, incubating overnight at room temperature a 5 mg/ml HI solution consisting of 20% Acetic acid (pH 1.85), 0.5 M NaCl, 0.05% Tween 20 and 40 μM ThT. The sample is incubated on a glass coverslip positioned on the microscope stage during time-lapse measurements. Image stacks are acquired at regular time intervals and ThT fluorescence intensity is monitored in single ROIs with different sizes highlighted in red. b - c) Magnification of details in the image in panel (a) The ROI is a single microparticle in panel b) and a small region within the microparticle in panel c). d - f) Normalized ThT fluorescence intensity versus time, obtained by integrating in each frame the values of every pixel of the ROI, neglecting the one with a value under 5, to eliminate the contributions of free ThT in solution. The kinetics has a sigmoidal profile with a lag phase, growth phase and plateau phase.*

Also in this case, the kinetics measured for a single microparticle is very similar to the ensemble kinetics and interestingly even the kinetics measured within the microparticle resembles very much both the ensemble and the single microparticle kinetics. As expected by reducing the area of the ROIs the signal-to-noise ratio decreases as well. Combining the observations obtained until now, it is reasonable to speculate that the surface catalyses the formation of the microparticles. The nucleation points in fact occur at the bottom of the aqueous drop, specifically at the water–glass interface. These nucleation points then trigger the formation and the growth of a new liquid-like dense phase. This results in a spatial heterogeneity of

the sample. Interestingly this is not accompanied by a spatial heterogeneity of the aggregation kinetics, which instead presents a high degree of homogeneity, dictated by the fact that within the same aqueous drop, all the fluorescence kinetics resemble each other independently on the ROI wherein it is measured. Moreover, the HI microparticles exhibit similar size and shape and same structural features (solid native-like core and fluid-like edges). All these results suggest that homogeneous mechanisms are involved.

Interestingly, at acidic pH, high ionic strength and high temperature HI aggregation is known to be regulated by heterogeneous nucleation mechanism [32, 39, 40, 126]. In these experimental condition in fact the aggregation kinetics, monitored by ThT staining, has a sigmoidal profile and in particular the growth phase follow an exponential law instead of a quadratic law which indicates a homogeneous nucleation mechanism. From a microscopic point of view, this is due to the fact that the presence of fibril auto-catalyses the process resulting in an exponential increase of the aggregates number. Moreover, HI aggregation kinetics exhibits a variability. The degree of the variability is controlled by HI concentration, as reported by Foderà et al. [40] in 2008, being higher at lower concentrations. HI is also well-known for the polymorphism that it exhibits. In fact, the result of the HI aggregation at these experimental conditions is also heterogeneous in terms of the formed species, amyloid fibrils and spherulites.

4.2.3 Effects of aqueous compartment size on supramolecular assembly

Given that these structures do not form in bulk, it is reasonable to assume that the size of the aqueous droplet influences the supramolecular self-assembly process in some way. To explore this effect, it was decided to compare the ThT fluorescence kinetics which occur in aqueous drops of different sizes. The results of the experiment are shown in Figure 4.11.

Figure 4.11a) shows five representative ThT fluorescence kinetic in as many aqueous drops whose size ranges from 130 μm (reported in blue) to 1500 μm (reported in yellow). The ThT fluorescence is normalized to the intensity value at the plateau. All the ThT fluorescence kinetics present a sigmoidal profile. It is easy to note that the formation of the microparticles is faster in small aqueous drops. In Figure 4.11b) the same kinetics are reported. The fluorescence intensity values are reported as a function of scaled time for the lag phase duration. The kinetics profile reveals a correlation between the aqueous drop size and the microparticle formation kinetics duration, this being longer in larger drops and, shorter in smaller drops.

In particular, the most significant difference lies in the duration of the lag phases, which is very short in small aqueous droplets and gradually increases as the droplet size increases. ThT fluorescence kinetics measured in drops of similar size present small variabilities in the duration of the lag phase. The duration of the lag phase for 250 μm drop ranges between 90 min and 150 min, therefore the measured variability is about an hour. This variability is significantly smaller than the difference of lag phase duration of the ThT kinetics which occurs between drops of different sizes, being at least double. The reported kinetics were chosen as the kinetics with an average lag phase.

The growth phases of the five kinetics present similar slopes, and as can be observed by Figure 4.11b) are almost superimposable within the experimental error. The only kinetics which deviates from the others is measured in the 130 μm aqueous drop (reported in blue). However, this kinetics has also a lower signal-to-noise ratio, due to the fact that the process in such a small drop is extremely fast. The fact that the slopes of the kinetics are the same suggests that after the formation of a critical nucleus, the process resulting in the growth of the microparticles is similar independently of the aqueous drop size.
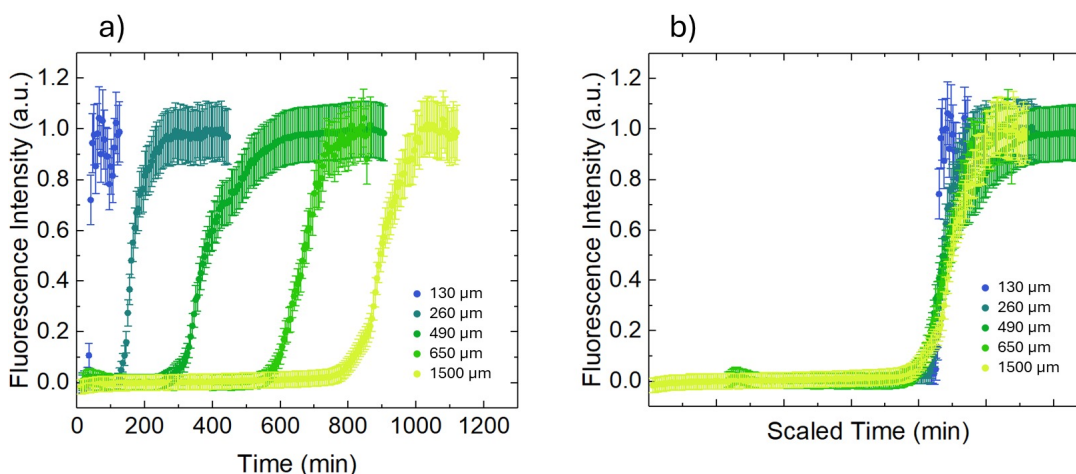

FIGURE 4.11: *a) ThT fluorescence kinetics measured in the whole aqueous drop. The sample is obtained incubating at room temperature 5 mg/ml HI in a 20% Acetic acid solution (pH 1.85) containing 0.5 M NaCl, 0.05% Tween 20 and 40 μM ThT in aqueous drop of different sizes. The drops sizes range from 130 μm to 1500 μm. All the fluorescence kinetics have a sigmoidal profile, and the duration of the lag phase increases in larger drops. b) The same fluorescence kinetics showed in panel a) reported as a function of a scaled time, to overlap the endpoint of the lag phase. The kinetics have superimposable profiles, within the experimental error.*

As already mentioned, the lag phase and growth phase are associated with distinct microscopical processes. All the existing models which interpret the aggregation kinetics in terms of molecular events are created for fibril aggregation, but it is reasonable to speculate that the main mechanisms are the same also for tridimen-

sional superstructures, such as the one analyzed in this study. In an aggregation process which can be described by sigmoidal kinetics, the lag phase is often interpreted as the time during which the nucleation points are formed from monomeric species in solution. This process implies the formation of oligomers and when a critical dimension is reached, they become nuclei from which the aggregation starts. This process is called homogeneous or primary nucleation. The growth phase is associated with the elongation process for fibril aggregation (in this case the radial growth) and the formation of new aggregates from the existing ones (heterogeneous or secondary nucleation) [45]. Recently Arosio et al. [43, 44] suggested that lag phase and growth phase cannot be exclusively ascribed to a single microscopical process. Rather, according to their model, these are a combination of processes which are governed by the rate constant of the reactions. For instance, they suggest that during the lag phase both the primary nucleation and elongation mechanisms occur and therefore the duration of the lag phase is the balance of the two mechanisms. Similar discussion can be done for the growth phase which is a combination of both elongation and secondary nucleation mechanisms, whose combination changes the slope of the kinetics. Nevertheless, it is anyway common consensus that the lag phase is regulated by homogeneous nucleation and the growth phase begins when the heterogeneous nucleation takes over.

FIGURE 4.12: *Aggregation rate, measured as the inverse of the lag phase duration, as a function of the radii of aqueous drops: the duration of the lag phase was measured as the time for which ThT fluorescence intensity reached the 2% of the maximum fluorescence (plateau region). Data were fitted by the function y = A+(B/x). The fit and the associated error are reported in red.*

The kinetics reported in Figure 4.11 only differ by the lag phase duration. This suggests that the size of the aqueous drop mainly affects the homogeneous nucle-

85

ation mechanism. Contrarily the growth phase remains unaltered, denoting that the process at the basis of the growth of the microparticles is not influenced by the size of the aqueous drop. The studied process occurs within small aqueous drops, which can be approximated to a hemisphere. The water–glass interface forms the base of this hemisphere, while the rest of the surface is the water–oil interface, as shown in Figure 4.1. It was observed that the process takes place only at the water–glass interface, which can be adjusted and controlled by changing the size of the drop. This determines to reduce (or increase) the surface area available to the protein. Therefore, the duration of the lag phase in the kinetics is linked to the accessible surface area. To investigate this phenomenon, it was decided to study the duration of the lag phase as a function of the aqueous drop size.
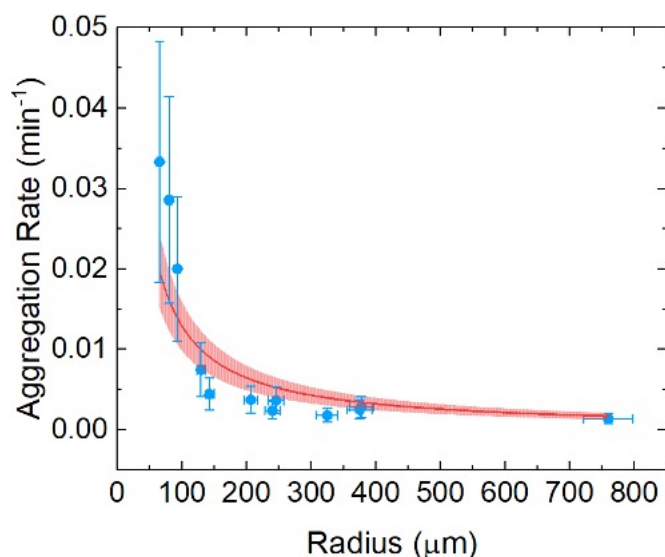
Figure 4.12 shows the aggregation rate, measured as the inverse of the lag phase duration versus the radius of the aqueous drop. The duration of the lag phase was quantified as the time needed for the kinetics to reach 2% of the maximum fluorescence intensity measured at the plateau. The fit performed on the data is reported in red. Data highlight that the aggregation rate decreases with the increase in drop size. In particular, data seem to follow a hyperbolic law. Combining all the information obtained so far, it is possible to infer that the nucleation process occurs at the bottom surface of the hemisphere, which consequently triggers the formation of the new liquid-like phase around the nuclei. Here, experimental data suggest that the observed process is regulated by the attachment of the protein molecules to the interface water – glass interface. This is not unusual since it is known that protein molecules exhibit the tendency to interact with interfaces, increasing the aggregation rate at the surfaces with respect to the bulk. This was associated with a combination of complex mechanisms which may decrease the nucleation energy barrier [170, 171]. In particular, it was reported by Sluzky et al. [128, 131] that HI molecules undergo conformational modifications in the proximity of hydrophobic solid surfaces. Hydrophobic interactions are therefore the main responsible for the attachment of HI to the interface. The experimental data here reported suggesting that the supramolecular self-assembly observed is driven by a sort of attachment nucleation process of the HI molecules to the water–glass interface at the bottom of the aqueous drop [172]. This results in the formation of the nuclei at the interfaces around which HI molecules condensate forming the microparticles.

To explain the observed behaviour, it is possible to consider that the formation of nuclei on the surface is likely influenced by the probability (P) of proteins diffusing within the aqueous drop and colliding with the surface. Simplifying the model, it is reasonable to assume HI molecules are evenly distributed within the hemispherical

drop and freely diffuse with an average free path λ. Under these conditions, the probability is inversely related to the radius of the hemisphere. In an oversimplified model, where particles travel freely for a distance λ before colliding with other particles, the probability that a particle within a distance $y < \lambda$ from the aqueous drop surface will hit the surface can be calculated as the ratio of two volumes: the volume of a spherical cap (V_c) with height $\lambda - y$ and radius λ (representing the region where the particle ends up after crossing the surface), and the volume of a sphere (V_s) with radius λ (representing the region where the particle could end up after travelling a distance λ in any direction). We denote this ratio as $P_c(y)$.

Moreover, the probability (P_L) of finding a particle within a layer of thickness dy at a distance $y \ll r$ from the surface of the aqueous drop can be determined by the ratio of the volume of the layer (V_L) to the total volume of the hemisphere (V_H).

$$P_L = \frac{V_L}{V_H} = \frac{\pi r^2 dy}{\frac{2\pi r^3}{3}} = \frac{3}{2}\frac{dy}{r} \tag{4.1}$$

Integrating the product $P_L P_c(y)$ over the interval $[0, \lambda]$ the final result is finally obtained:

$$P = \int_0^\lambda P_c(y)P_L = \int_0^\lambda \frac{3}{2r}P_c(y)dy \tag{4.2}$$

$$P = \frac{9\lambda}{16r} \propto \frac{1}{r} \tag{4.3}$$

As expected from the data reported in Figure 4.12, probability P has an inversely proportional relation with the radiusr of the drop. The fit reported in Figure 4.12 is a hyperbolic function which has a good agreement with the data. This supports the idea that the observed phenomenon is nucleated by an attachment nucleation mechanism, which is favoured in smaller drops, characterized by a high surface-to-volume ratio. Moreover, the whole phenomenon is regulated by the free diffusion of HI molecules in drop volume.

As already mentioned in the description of Figure 4.2, within aqueous drop of similar size the number and the size of microparticles may vary among distinct drops. To investigate this phenomenon and its causes and implications, two aqueous drops with similar size were compared. In Figure 4.13a-b) two 1024×1024 pixels two-photon microscopy fluorescence images of HI microparticles in two 260 μm drops are reported. The microparticles are obtained at usual experimental conditions: incubation overnight at room temperature of 5 mg/ml HI in a 20% Acetic

acid solution (pH 1.85), containing 0.5 M NaCl, 0.05% Tween 20 and 40 μM ThT. In Figure 4.13c) it is reported the size distribution of the microparticles shown in panels a) and b) in red and green respectively. The size of the microparticles is measured when the equilibrium of the kinetics is reached and the size of the microparticles remains constant over time. The average diameter of the red distribution is 3.3± 1.1 μm and the average diameter of the green distribution is 5.1 ± 1.0 μm. The error associated with the average measurements is the standard deviation of the histogram. Figure 4.13d) shows the ThT fluorescence kinetics measured in the two drops, following the same colour code of the histogram. The images shown in Figure 4.13a-b) are two representative fluorescence images of two distinct drops of the same size. The microparticles which occur in the aqueous drop reported in panel a) are smaller and more numerous with respect to the microparticles which are formed in the drop shown in panel b). To quantify these differences the size distribution of the microparticles within each drop was performed (shown in Figure 4.13c). The microparticles in panel a) are almost 2 μm smaller than the microparticles of panel b). Moreover, the counts (i.e., the number of microparticles) of the red histogram are about double the counts of the green distribution. Interestingly both fluorescence kinetics measured within the aqueous drop present the same sigmoidal profile and similar lag phase. As already mentioned, the lag phase duration of ThT fluorescence kinetics in two similar size drops may show a small variability. This is due to the intrinsic stochasticity of the attachment nucleation mechanism. The lag phase is more influenced by the drop size than the intrinsic stochasticity of the process.

The number of microparticles corresponds to the number of nucleation points which are heterogeneously distributed at the water–glass surface at the bottom of the aqueous drops. The higher number of microparticles may therefore be due to a higher amount of nucleation sites present in the sample from which the microparticles originate. This could be due to external conditions in the form of impurities on the glass surface. To test this hypothesis a pattern was imprinted to the glass surface. Figure 4.14 shows a representative two-photon microscopy fluorescence images of HI microparticles obtained after an overnight incubation at room temperature of the 250 μm aqueous drop (5 mg/ml HI in a 20% Acetic acid solution (pH 1.85), containing 0.5 M NaCl, 0.05% Tween 20 and 40 μM ThT). Differently from all the other samples reported so far, the microparticles grow on a preferential direction dictated by a pattern imprinted onto the glass surface. This denotes that the nucleation points can be externally induced to the surface, still maintaining the overall process the same unchanged, highlighting the generality of the overall
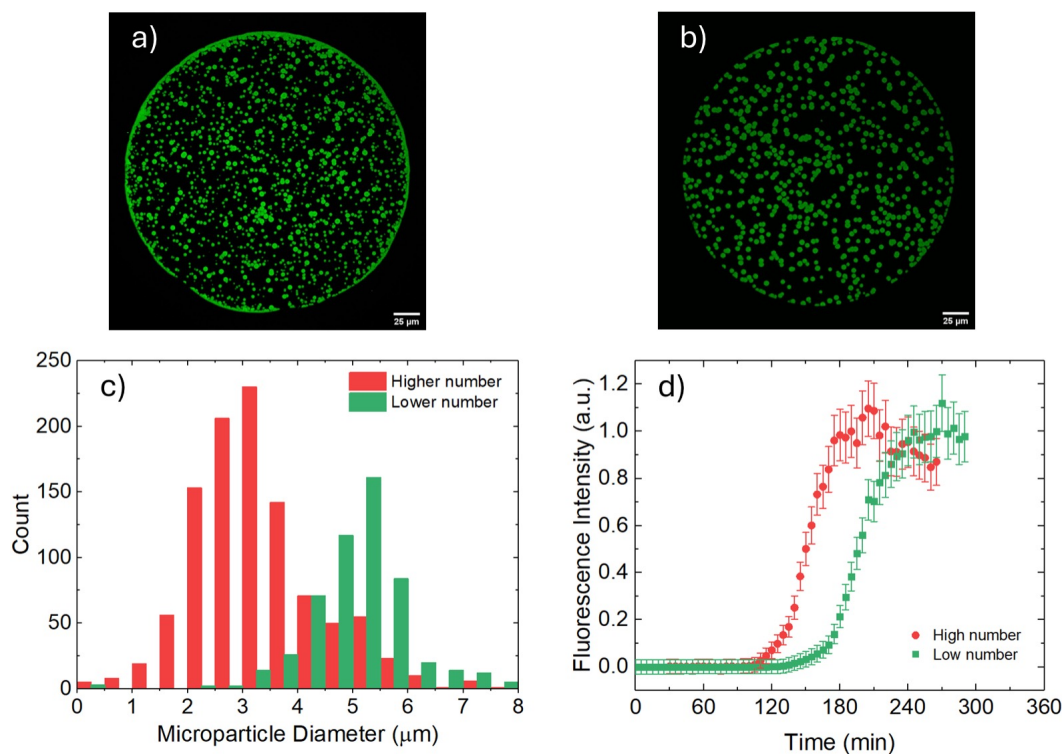
Figure 4.13: *(a-b) 1024×1024 pixels two-photon microscopy fluorescence images of HI microparticles incubating overnight at room temperature 5 mg/ml HI in a 20% Acetic acid solution (pH 1.85), containing 0.5 M NaCl, 0.05% Tween 20 and 40 μM ThT in 260±10 μm drops (λ_{exc} = 780 nm, detection range = 450 - 600 nm). Scale bar is 25 μm. c) Size distributions of microparticles shown in panels a) and b) in red and green respectively. The measured average diameter results 3.3 ± 1.1 μm (red distribution) and 5.1 ± 1.0 μm (green distribution). The errors were estimated as the standard deviation of the histograms. Histograms bin size is 0.5 μm. d) ThT fluorescence kinetics which occur in the drop shown in panels a) and b) in red and green respectively.*

process.

The fact that the number and size of microparticles are dependent parameters could indicate that the same fraction of HI molecules is sequestered within the condensate regardless of the number of nucleation sites, leading to particles of the same spherical morphology, denoting that the aggregation process is independent of their number, as indicated by the fact that the growth phase of all the ThT kinetics are superimposable.

It was explained as the sizes of the aqueous drops influence the self-assembly process affecting the time during which the HI molecules hit the bottom surfaces and attach to hit, therefore affecting nucleation (and aggregation) rate. This translates into a variation of the lag phase of ThT fluorescence kinetics. Now it will be discussed how the size of the drops also affects other aspects of the process, starting with microparticle size and then finishing with the structure of these HI self-assemblies. In Figure 4.15 the size distributions of HI microparticles measured at the equilibrium phase of the kinetics are reported. Figure 4.15a) shows the size dis-
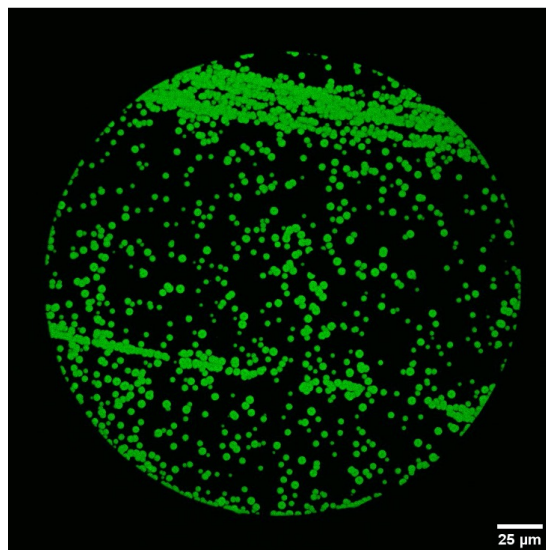
FIGURE 4.14: *1024×1024 pixels two-photon microscopy fluorescence images of HI microparticles obtained incubating overnight at room temperature 5 mg/ml HI in a 20% Acetic acid solution (pH 1.85), containing 0.5 M NaCl, 0.05% Tween 20 and 40 μM ThT in 250 μm drops (λ_{exc} = 780 nm, detection range = 450 - 600 nm). Scale bar is 25 μm. The microparticles grow on preferential directions due to a pattern imprinted on the glass surface.*

tributions of the microparticles, which form in three representative distinct aqueous drops of same size (270 ± 10 μm). As described above, depending on the number of nucleation sites, the number of microparticles may vary among drop of same size and this results in variation of the size of the microparticles. As can be seen from the histograms microparticles are characterized by monodisperse size distributions characterized by different average diameters namely 2.9 ± 1.1 μm (green distribution), 5.0 ± 0.9 μm (yellow distribution) and 6.4 ± 1.5 μm (red distribution).

In Figure 4.15b) it is reported the size distributions of the microparticles which occur in three representative distinct aqueous drops with an average diameter of about 1.8 ± 0.1 mm. The size distributions in panel b) are centred at 8 ± 2 μm (green distribution), 10 ± 2 μm (yellow distribution) and (9.9 ± 1.5) μm (red distribution), so also, in this case, a certain variability in the size of the particles is observed, and in average the measured average diameters of the particles are significantly larger than the ones formed in the smaller drops in panel 4.6a). Two black dotted lines are drawn in correspondence with the centres of the lower diameter distributions (green) for both samples, to better visualize the difference in size. To highlight that the difference in size induced by the drop size is higher than the one intrinsic in drop of similar size, it was decided to report for each drop size, the data of the sample which showed higher size variability.

Similar to what was observed in Figure 4.13, the measured average size of microparticles reduces, when the number of the microparticles increases. This relation
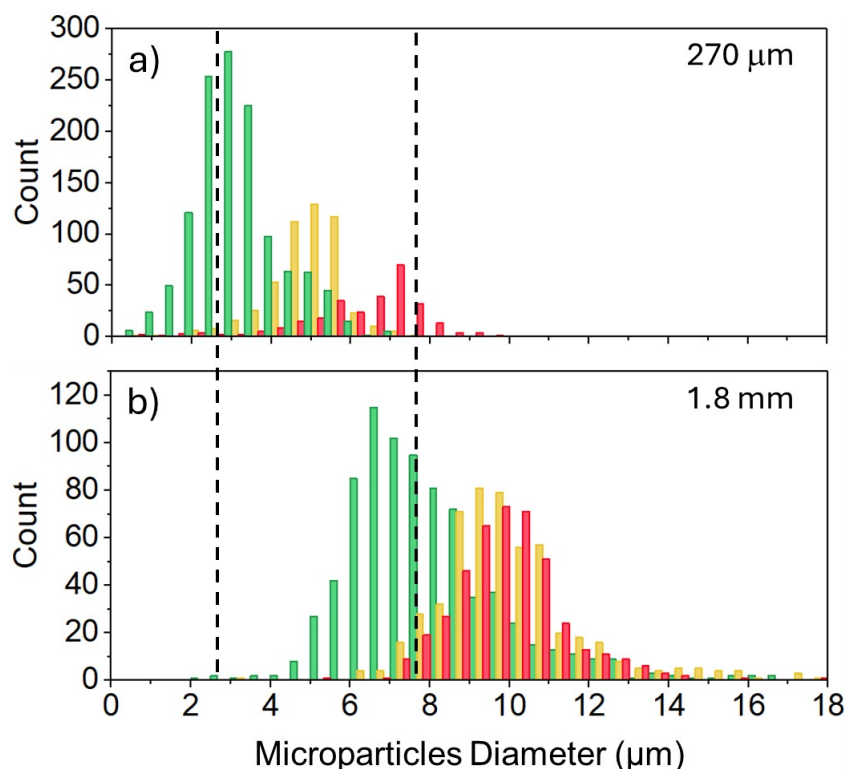
Figure 4.15: *a) Size distributions of microparticles formed by incubating a 5 mg/ml HI in a 20% Acetic acid solution (pH 1.85), 0.5 M NaCl, 0.05% Tween 20 and 40 µM ThT at room temperature overnight in three distinct aqueous drops with average size of 270 ± 10 µm. Histograms bin size is 0.5 µm. The measured average diameter results 2.9 ± 1.1 µm (green distribution), 5.0 ± 0.9 µm yellow distribution and 6.4 ± 1.5 µm (red distribution). b) Size distributions of particles formed in the same solution condition obtained in three different aqueous compartments with an average diameter of 1.8 mm. Histograms bin size is 0.5 µm. The average measured diameter is 8 ± 2 µm (green distribution), 10 ± 2 µm (yellow distribution) and 9.9 ± 1.5 µm (red distribution). Black dotted vertical lines are used as a guide for the eye allowing to qualitatively observe the different sizes of the particles incubated in aqueous drops with different sizes.*

is respected when comparing size distributions of drops of the same size, as it is shown in Figure 4.15a) (and was previously shown in Figure 4.13). For instance, taking into account the green and the red histograms, it is evident that the red distributions, which have an average size of 6.4 ± 1.5 *µm*, present a counts number significantly lower than the one of the green distributions which have an average of 2.9 ± 1.1 *µm*. This relation holds true also when considering two size distributions of two different size drops: the green distribution in Figure 4.15a) is composed by a more counts than the green distribution in Figure 4.15a) (average size is 8 ± 2 *µm*). Therefore, as the experiments are conducted at constant protein concentration, data further support the idea that the supramolecular association of HI, in these conditions, ends when the same fraction of HI molecules is recruited in the microparticles regardless of their number.

In Figure 4.16 it is reported the fraction of occupied area by the microparticles
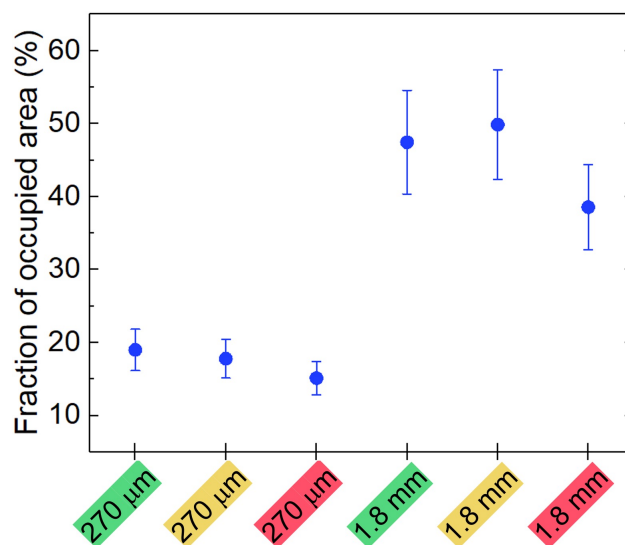
FIGURE 4.16: *Ratio between the number of pixels where ThT fluorescence is detected with respect to the total number of pixels. The measure is performed at the equilibrium phase of the ThT fluorescence kinetics. This measures the ratio between the surface occupied by the microparticles and the total accessible area. The ratios were calculated for the same aqueous drops for which the size distributions were analysed in Figure 4.15: the sample name on the x axis presents the same colour code of the histograms. The measured ratio is constant at about 17% of the total number of pixels for the 270 μm drops and 45% for the 1.8 mm drop. The same fraction of the glass coverslip is occupied by the microparticles, independently of their number/size.*

for each sample, analysed to obtain the size distribution shown in Figure 4.15. The sample names are reported on the *x* axis and are reported using the same colour code of the size distributions. The fraction of occupied area is defined as the ratio between the number of pixels where the fluorescent signal is detected and the total number of pixels in the total accessible area to the nuclei formation, from which the microparticles grow. This is therefore an estimation of the fraction of the surface occupied by microparticles with respect to the total attachment-available surface. It is immediately evident that this parameter is constant for aqueous drop of the same size resulting in an average value of 17% of the total attachment-available surface for the 270 μm diameter drop and 45% for the 1.8 mm diameter drop. This further indicates that the same fraction of HI molecules participate in the protein condensation process and therefore in the growth of microparticles, regardless of the number and size of the final particles in aqueous drops of the same size.

In larger drops, the fraction of occupied area is higher with respect to smaller drops, which is dictated by surface-to-volume ratio of the drops. Indeed, at constant protein concentration, the number of molecules depends on the sample volume (r^3), while the available attached surface depends on (r^2). Since the observed association process occurs at the surface, and the inner volume of the aqueous drop serves as a reservoir for molecules, the number of molecules that can be recruited in the

condensation process is linearly dependent on the radius.

$$\frac{N}{\Sigma} \propto C \, r \qquad (4.4)$$

where N is the number of molecules, Σ is the accessible surface, C is the concentration and r is the radius of the drop. So, comparing surfaces with the same extension, in a larger drop the number of molecules available for the growth of the particles is higher, resulting in larger microparticles and in a higher fraction of the occupied surface.

At the beginning of this section, it was discussed the possibility of whether the aqueous drop size, affects the morphology and the structure of the microparticles, besides the nucleation process. Until now the morphological aspect was investigated. Now the structural aspect will be finally examined. To recapitulate, the presented experiments allowed us to isolate a supramolecular assembly phenomenon involving HI proteins at the solution-glass interface. It was found that the proteins associate into dense spherical condensates, which are positive to ThT, featuring a solid core and a fluid-like corona. The process starts with the formation of small clusters or aggregates of HI molecules at the solution-glass interface, acting as nuclei and initiating phase separation. Following the primary nucleation at the interface, proteins gradually separate from the surrounding solution, leading to the radial growth of microscale coacervates. Unlike what is typically observed in LLPS, the newly formed condensates are not dynamic and remain stable in fixed positions around the solid nuclei, as shown in Figure 4.8. This observation excludes the formation of other microscale species in the sample. The evolution of this process leads to hybrid structures, suggesting a liquid-solid state transition and the formation of intermolecular β-structures typical of amyloid.

To obtain information on inter-molecular amyloid β-structure and the spatial heterogeneity of the microparticles, by exploiting the spectroscopic properties of ThT [28], ThT is known for its strong affinity for amyloid fibrils, driven by specific interactions with intermolecular β-sheet-rich regions. The ThT fluorescence is influenced by binding site characteristics, such as charge, the presence of specific residues, or the spacing between the β-strands [74, 173]. Consequently, ThT fluorescence signals show significant variations in quantum yield and fluorescence lifetime depending on the structural diversity of the amyloid fibrils it interacts with. This variability in the ThT signal allows for the exploration of amyloid aggregates polymorphism and intrinsic heterogeneity.

As mentioned above, we have previously demonstrated a strong correlation between the molecular organization of the amyloid and amyloid-like structure and the

ThT fluorescence lifetime by means of Fluorescence lifetime imaging microscopy (FLIM), analysing by the means of the phasor approach [28]. FLIM allows to acquired images where the contrast is provided by fluorescence lifetime, rather than its intensity. The phasor approach was developed by Digman et al. [107] and allow for a graphical representation of the data providing a fit-free analysis. This is a great advantage because data do not need to be superimposed by an a priori model, rather the model is provided by data itself (see methodology chapter). through FLIM-Phasor analysis of ThT-stained samples is possible to achieve the mapping of structural details at a submicron scale. This technique enables a detailed examination of the molecular architecture within the samples, providing insights into the packing density of β-structures (ThT-phasor [24, 28, 86, 87, 88, 174, 175]). This technique was extensively used to analyse the molecular structure of three-dimensional amyloid superstructure, to probe the heterogeneity within aggregation samples and even to explore the evolution of a supramolecular assembly from condensates to a solid, amyloid phase.
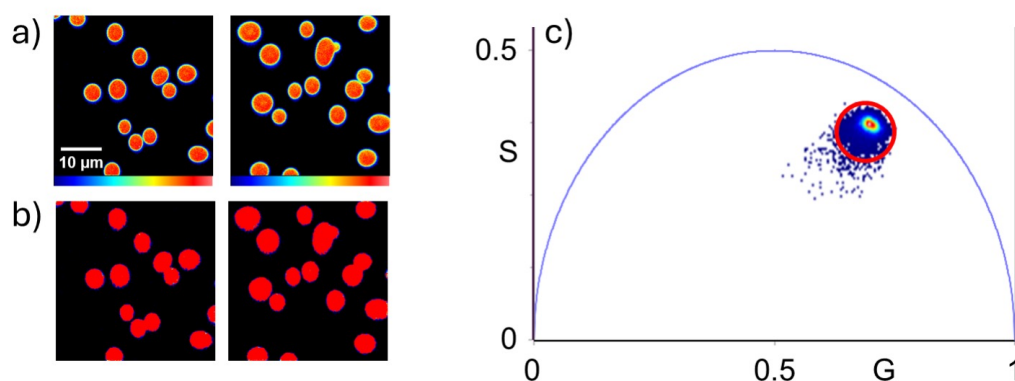

FIGURE 4.17: *Phasor analysis of FLIM measurements on microparticles formed by incubating a 5 mg/ml HI in a 20% Acetic acid solution (pH 1.85), 0.5 M NaCl, 0.05% Tween 20 and 40 μM ThT at room temperature. a) 256×256 pixels fluorescent intensity images of HI particles incubated in a 220 μm aqueous drop for about 3.5 hours at room temperature. Scale bar 10 μm. b) Phasor maps of the previous intensity images: the pixels are coloured in red according to the red cursor which selects the single lifetime distribution in the phasor plot (c). c) Phasor plot which shows a single lifetime distribution.*

Figure 4.17a) shows 256×256 pixels representative fluorescence intensity images of microparticles sample obtained incubating the HI solution at room temperature for about 3.5 hours in a 220 μm aqueous drop (scale bar is 10 μm). In Figure 4.17b) the phasor maps obtained from the phasor analysis are reported. In Figure 4.17c) it is reported the phasor plot where it is shown a single lifetime distribution (cloud of points) selected by a red cursor. HI microparticles, shown in Figure 4.17a), have a spherical shape and a size of about 5 μm. At this spatial resolution

and because of the colour code used, it is difficult to observe the low ThT intensity region at the core of the microparticles, but looking closely it is present, in particular in some microparticles in the right image. The phasor analysis reveals that all ThT molecules experience the same environment in all the microparticles within the sample. This is indicated by the fact that a single lifetime distribution is visible in the phasor plot. This distribution is positioned within the universal circle (the blue semi-circumference) denoting that the ThT fluorescence lifetime is multi-component lifetime decay [107]. This observation is in line with the literature which associated two components to ThT lifetime [84]. Moreover, the distribution lies in a region where ThT lifetime distribution was already found in phasor analysis [24, 28, 86, 87, 88, 174, 175]. By selecting the lifetime distribution by a red cursor in the phasor plot, the pixel of the image, which corresponds to the one selected, are marked by the same colour. This new image is the phasor map which allows to obtain a spatial distribution of the lifetime. Here all the microparticles within the images are coloured in red indicating a structural homogeneity of the sample.

Images at higher spatial resolution were acquired to confirm that the low intensity region at the core of the microparticles (see Figure 4.5 as reference) reflect a structural heterogeneity of the amyloid structure as suggested by FRAP experiments (Figure 4.7). Moreover, to investigate whether the size of the aqueous drops influences the structure of the microparticles, these were imaged in two drops of different sizes. Figure 4.18a-b) shows images of individual particles formed in a 190 μm (a) and 830 μm (b) aqueous drop. The microparticles were imaged at the equilibrium phase of the kinetics to study the stationary state. The microparticles present different sizes as expected, the first being smaller, and in all the microparticles lower fluorescence intensity is detectable at the central region. Figure 4.18c-d) shows the phasor maps obtained by the phasor analysis. In Figure 4.18e) the phasor plot is reported, showing two distinct fluorescence lifetime distributions. The shorter lifetime distribution is selected by a green cursor and the longer lifetime distribution is selected by a magenta cursor. The phasor maps shown in panel c) highlight how all the microparticles (which occurred in the 190 μm), are uniformly coloured in green, indicating also in this case a structural homogeneity of the sample. Different is the case for the phasor maps of the microparticles which occurred in the 830 μm drop, shown in Figure 4.18d): the phasor maps are mainly coloured in magenta but the core of the microparticle, in correspondence with the lower ThT intensity, it is coloured in green, indicating a shorter ThT fluorescence lifetime. The shorter lifetime indicates a less amyloid structure in line with the FRAP results and low fluorescence intensity measured. This result suggests structural differences between
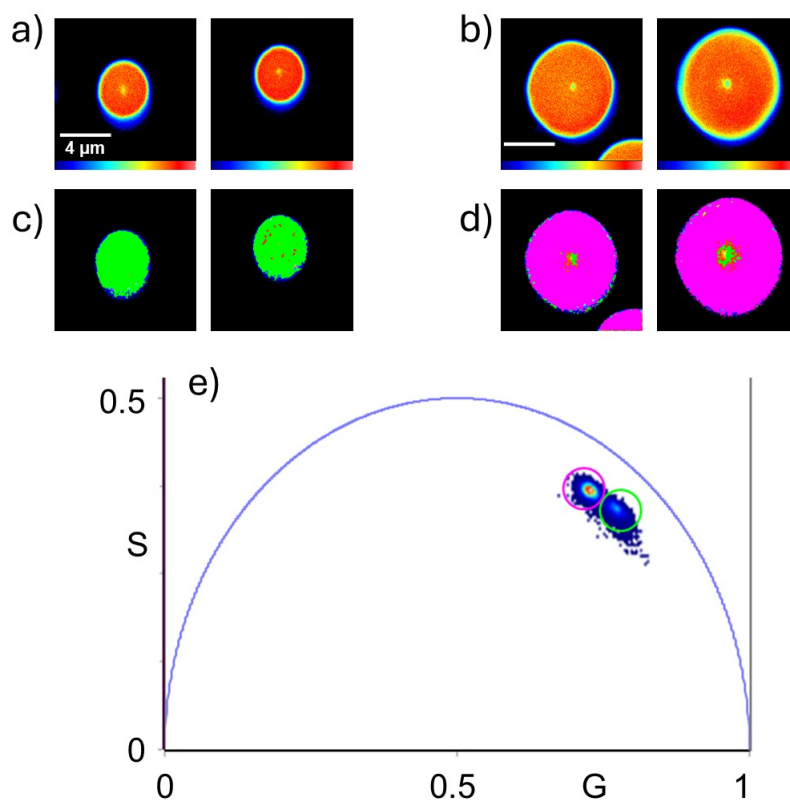
FIGURE 4.18: *Phasor analysis of FLIM measurements on aggregates formed by incubating a 5 mg/ml HI in a 20% Acetic acid solution (pH 1.85), 0.5 M NaCl, 0.05% Tween 20 and 40 μM ThT at room temperature. a-b) 256×256 pixels fluorescent intensity images of single HI aggregates incubated overnight in a 190 μm drop (a) and 830 μm drop (b). Scale bar 4 μm. c-d) Phasor maps corresponding to the respective intensity images. e) Phasor plot showing two different and well-defined lifetime distributions. Shorter lifetime distribution, selected by a green cursor, is associated with the aggregates grown in the smaller drop (c). Longer lifetime distribution, selected by a pink cursor, is associated with the aggregates grown in the larger drop (d). The cores of the aggregates in panels d) are coloured in green, indicating a shorter lifetime and a different molecular structure with respect to the surrounding regions, in line with what was shown by the FRAP experiments.*

the observed particles at the level of ThT binding sites. Moreover, it is reasonable to speculate that the cores of the smaller microparticles were not visible (Figure 4.18c) because the core is composed of too few pixels with a too low fluorescence intensity to be able to create a visible third lifetime distribution in the phasor plot. Another information to keep in mind is that the spatial resolution is also limited by the cursor size.

In line with observations in other amyloid-related systems, the lifetime distribution clusters form a straight line in the phasor plot, connecting two points on the universal circle corresponding to $\tau_1 = 0.6$ ns and $\tau_2 = 2.5$ ns. This pattern indicates that the Thioflavin T (ThT) lifetime in both samples can be described by double exponential decays with two primary components: τ_1 and τ_2. The rapid decay component (τ_1) is linked to less specific binding sites where Thioflavin T (ThT)

fluorescence is due to increased environmental viscosity. In contrast, the slower decay component (τ_2) corresponds to more specific interactions between ThT and intermolecular β-structures, which impose greater constraints and reduce flexibility within the ThT-binding site, thereby increasing its quantum yield and lifetime.

A quantitative analysis of the Fluorescence lifetime imaging microscopy (FLIM) data, employing a double exponential model, is performed using the two principal lifetime components according to the equation:

$$I(t) = A_1 e^{\frac{-t}{\tau_1}} + A_2 e^{\frac{-t}{\tau_2}} \tag{4.5}$$

where A_1 and A_2 are the amplitude of the single exponential decays τ_1 and τ_2 . In the phasor plot, the distance between each point of the cloud and the other single-exponential phasor is related to the fraction F_1 and F_2 of each component which are proportional to A_1 and A_2.
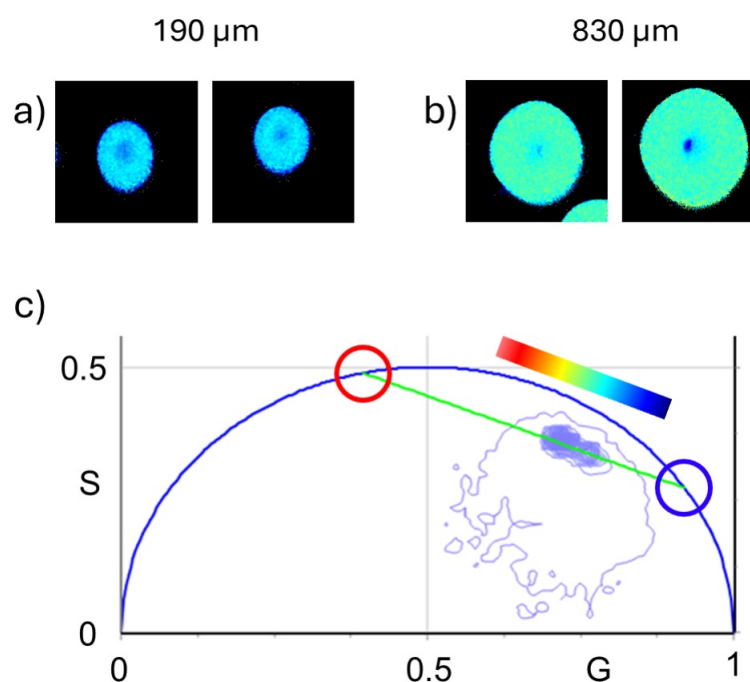
Figure 4.19: *Phasor analysis of FLIM measurements on particles formed by incubating a 5 mg/ml HI in a 20% Acetic acid solution (pH 1.85), 0.5 M NaCl, 0.05% Tween 20 and 40 μM ThT at room temperature. a-b) 256×256 pixels fluorescent intensity images of single HI particles incubated overnight in a 190 μm (a) and 830 μm (b) aqueous drop. Scale bar 4 μm. c-d) Lifetime fraction maps of the previous intensity image. e) Phasor plot showing an elongated lifetime distribution that lies on a straight line between the two lifetime components, highlighted by the red (longer lifetime) and the blue (shorter lifetime) cursors on the universal circle. The colour code is shown above the phasor plot, going from red to blue continuously. The colours of the phasor maps (panel c-d) follow the colour code above the phasor plot.*

In Figure 4.19a-b) shows the fraction maps of the same intensity maps shown

in Figure 4.18a-b) respectively. The images are coloured by the same colour code obtained from the analysis of the corresponding phasor plot in Figure 4.7h).

The analysis maps the fractions F_1 and F_2 in false colour, using a scale from blue (representing the pure fast component with a short lifetime of $\tau_1 = 0.6$ ns) to red (representing the pure slow component with a long lifetime of $\tau_2 = 2.5$ ns). This colour-coded representation visually distinguishes and highlights the relative proportions of these two fluorescence components across the analyzed samples. In smaller condensates incubated in the 190 μm aqueous drop, the shorter lifetime component is dominant with $F_1 = 0.71$, while in larger condensates incubated in the 830 μm aqueous drop, the longer lifetime component is more prevalent with $F_1 = 0.62$. Both samples show a dominance of the shorter lifetime component, aligning with FRAP measurements.

This indicates that the fluid-like environment surrounding ThT is characterized by binding sites with relatively low specificity, suggesting a coacervation nature or a low presence of β-structures within the observed area. Additionally, the analysis implies that particles formed in the 190 μm aqueous drop have a less densely packed β-sheet structure or lower viscosity compared to those grown in the larger aqueous drop, where more densely packed intermolecular β-structures are present.

It is important to note that the use of a continuous colour map in the analysis allows for greater detail in the lifetime map, as it is not limited by the radius of the cursors. This enables us to distinguish that in the core of the particles, ThT decays are characterized by a shorter fluorescent lifetime (dark blue) compared to the edge, confirming a lower affinity of this region for ThT. By examining the phasor plot and comparing the results with previously reported literature, we can conclude that the microscale particles observed at the solution-glass interface share structural characteristics with naturally occurring amyloid superstructures. These particles are similar in shape and size to other particulates and display a core-shell structure, which we hypothesize arises from primary nucleation, similar to spherulites. However, they exhibit relatively weak or sparse intermolecular amyloid β-structures.

4.3   CONCLUSIONS

In this Chapter the supramolecular assembly of HI within sub-microliter aqueous compartments was investigated. This process leads to the formation of spherical HI microparticles at the water-glass interface. This highlights the effect of small volume and presence of interface to the aggregation of HI. In fact, at the same solution condition aggregation of HI was never reported.

The first section of this study focuses on the analysis of the morphologies of these structures. They appear spherical with a micrometre size. By means of FRAP measurements, the physical state of the microparticle was investigated. These newly formed supramolecular assemblies present a solid core and a fluid-like corona. These features make them a middle way between spherulites, which present a similar conformation, and particulates, which share their small size. The presence of their fluid-like edges suggests the possible LLPS-driven origin of the microparticles. Their formation and growth were explored in the second section of this study. The microparticles were observed to grow from fixed nucleation points on the water-glass interface. Around this point, the HI molecules/oligomers condense and grow until an equilibrium is reached with the species in solution. The aggregation kinetics of the microparticles were studied by monitoring the fluorescence of Thioflavin T, a gold-standard fluorescent dye in amyloid studies. The ThT fluorescence kinetics were reported to be the same whether if measured in the whole drop, in a single microparticle or in a single region within the microparticle. This suggests that HI in these experimental conditions does not undergo a heterogeneous nucleation mechanism, contrary to what is always observed in bulk measurements in literature.

Finally, the third section of the Chapter focuses on the impact of the size of the aqueous compartment on the overall process. This can be summarized in nucleation effects, morphology effects, and structural effects. The nucleation effect is referred to the fact that the lag phase of the ThT fluorescence kinetics measured in larger drops are longer, being dependent on the size of the compartments, without varying the speed of growth of the microparticles. This suggests that only the primary nucleation on the glass interface is affected by the size of the compartment, while the condensation process, responsible for the growth of the microparticle is unaltered. This was rationalized by means of a simplified mathematical model. The nucleation is therefore driven by the free diffusion of HI molecules within the aqueous compartment. The size of the compartments also affects the size of the microparticles, being larger in larger drops due to the higher number of HI molecules in solution which can condensate around the solid nuclei. Finally, the molecular structure of the microparticles is also affected by the compartment size. It was observed that the drops which occur in smaller compartments present a less amyloid-like structure with respect to ones which occur in the larger compartments. These observations show that proteins, when exposed to a range of environmental conditions, exhibit the ability to form common molecular structures. This suggests a set of universal rules guiding protein folding and aggregation, regardless of external conditions. These consistent principles highlight the inherent stability of these biological pro-

cesses. Recognizing these shared behaviours offers valuable clues to understanding the basic mechanisms behind protein self-assembly.

4.4 SAMPLE PREPARATION AND PARAMETERS USED FOR MEASUREMENTS

4.4.1 SAMPLE PREPARATION

Human Insulin (HI) was dissolved in a solution containing Acetic Acid 20% and NaCl 0.5 M (pH = 1.85). When completely dissolved, the solution of HI was filtered by a 0.2 μm filter and then diluted to a final concentration of 5 mg/ml. Protein concentration was measured by UV – Vis spectroscopy by means of a Jasco – V770 spectrophotometer using the molar extinction coefficient $\epsilon = 1$ at 276 nm for 1.0 mg/ml. ThT and Tween-20 to a final concentration of 40 μM and 0.05% w/v, respectively, were added to the solution. The stock concentration of ThT and Tween-20 are about two orders of magnitude higher (3.36 mM ThT and 5% w/v Tween-20) with respect to the final concentration, to minimize the dilution effect and to make it negligible. For the experiment with HI labelled with Alexa 647 (HI647), it was added at the last step, at a final concentration of 80 nM.

To create sub-microliter scale aqueous compartments a drop of a freshly prepared protein solution was injected in a 100 μl drop of mineral oil deposited on a glass coverslip using a standard pipette. A glass Hamilton syringe of 1 μl was used to inject the sample solution into the mineral oil drop. Before using the syringe, it was thoroughly rinsed with acetone and then with acetic acid. The initial five drops of the solution dispensed from the syringe were discarded. This procedure is employed to cleanse the syringe, removing undesired contaminants and any potential residues of acetone that might interfere with the aggregation process. Small aqueous droplets, with variable size, are immersed in the oil at the interface with the glass coverslip. Protein microparticles' formation was observed within the microliter compartments either during measurements at the microscope stage or when the sample was incubated in the dark at lab temperature (23°C). All the experiments were repeated at least three times.

4.4.2 2PM AND CLSM MEASUREMENTS

The experiments were performed using a Leica TCS SP5 confocal laser scanning microscope, with a 63×/1.40-0.60 and 40×/1.25-0.75 oil objective, and a scanning

frequency 400 Hz (Leica Microsystems, Germany). All the images were acquired at a resolution of 1024 × 1024 pixels. ThT fluorescence was excited at 780 nm (Spectra-Physics Mai-Tai Ti:Sa ultra-fast laser) and the detection range was 450 – 600 nm for images acquired in two-photon microscopy mode. Kinetics measurements were acquired using two-photon excitation. For images acquired by confocal microscopy, the ThT fluorescence was excited at 470 nm (Leica Supercontinuum White Light Laser (WLL)) with a detection range was 485 – 585 nm, and the HI647 fluorescence was excited at 633 nm (WLL) with a detection range is 650 – 750 nm. The analysis of the microscopy data was performed by the open-source software ImageJ Fiji (https://imagej.net/software/fiji/).

4.4.3 FLIM data analysed by phasor approach

Fluorescence lifetime imaging microscopy (FLIM) were acquired in the time domain by means of a Leica TCS SP5 confocal laser scanning microscope coupled with picoHarp 300 TCSPC module (Picoquant, Germany). 256 × 256 pixels FLIM images were collected with a 63×/1.4 oil objective and scanning frequency 400 Hz, exciting ThT fluorescence at 470 nm (WLL) and collecting it in the detection range 485 – 585 nm (laser repetition rate is 80 MHz).

FLIM analysis was performed by the SimFCS4 software developed at the Laboratory of Fluorescence Dynamics, University of California at Irvine (http://www.lfd.uci.edu). FLIM calibration of the system was performed by measuring the fluorescence lifetime of Fluorescein in a basic aqueous solution that is known to be a single exponential of 4.0 ns.

4.4.4 FRAP measurements

FRAP experiments were performed using FRAP wizard of the Leica TCS SP5 confocal laser scanning microscope control software and WLL as an excitation/bleaching source. The 256 × 256 pixels images were acquired with a 63×/1.4 oil objective, and scanning frequency 400 Hz, on the samples that present a fraction of HI647 (80 nM). HI647 fluorescence was excited at 633 nm (Leica "white light" laser) and collected photons in the range 650 – 750 nm. Bleaching was performed for 20 frames (1.306 exposure time per frame) with high laser power in a circular region of interest with a radius of about 1 – 1.2 μm. The analysis of the microscopy data was performed by the open-source software ImageJ Fiji (https://imagej.net/software/fiji/).

CHAPTER 5

Conclusions

The aim of this thesis is to analyse the formation of spherical microscale supramolecular assemblies from globular proteins and to investigate how their properties and association mechanisms are affected by the surrounding environment. Various unrelated proteins have been shown to form spherical microparticles with amyloid-like properties. These gel-like aggregates typically have diameters of hundreds of nanometres [22, 23, 24] and contain large amounts of non-native intermolecular β-structures [22, 24]. The ability to form these particulates is suggested to be a generic property of all polypeptide chains, occurring upon partial unfolding of protein native conformations. This process is mainly driven by weak interactions such as hydrophobic forces and hydrogen bonding, leading to the formation of aggregates with nearly identical properties regardless of the originating protein. Protein LLPS results in protein coacervates whose size, morphology, and dynamics are determined by the interplay between the driving force for demixing, interfacial tension, and material mobility. Increasing evidence suggests that LLPS can be also considered an intrinsic property of proteins/polypeptides. This phenomenon is favoured when a protein has sufficient concentration and appropriate interaction strength, resulting from a complex interplay between entropic and enthalpic interactions. Weak multivalent interactions sustain the higher-order molecular arrangement within protein spherical condensates and preserve their liquid-like properties.

The experimental results reported in this thesis focus on the molecular mechanisms involved in the analysed phenomena, providing insights into the general features of LLPS and the aggregation process.

In Chapter 3 the LLPS process of BSA in the presence of PEG as molecular crowding agent is described. Protein LLPS was induced by subjecting the sample to a decreasing temperature ramp. This process results in the formation of small spherical BSA coacervates, with few micrometres diameter. The newly formed coacervates exhibit liquid behaviour and are highly dynamic. Results indicated that the transition temperature below which LLPS occurs could be modulated by changing solution conditions by adding a chaotropic (ethanol) or a kosmotropic (glycerol) agent. In particular, it was highlighted that reducing the amount of order in the

structures formed by water molecules leads to an increase in the transition temperature promoting the protein-protein interactions with respect to the protein-water interaction. Vice versa, a more ordered aqueous phase disfavoured protein-protein interactions resulting in a decrease of the transition temperature of the process. The observed changes are consistent with expectations. Ethanol is known to induce a reduction, while glycerol leads to an increase in the hydration shell of the protein, consequently affecting its thickness and overall stability [157, 161]. This, in turn, translates to a higher or lower propensity of the protein molecules to self-assemble, respectively. This highlights the crucial role of water in the stability, structure, and dynamic of proteins, as changes in the aqueous environment impact protein thermodynamics assisting in the hydrophobic collapse during protein association, and mediating hydrogen bonding. These effects can also be attributed to changes in the dielectric constant of the medium, polarity, and viscosity, which all influence protein behaviour. Variations in these properties can alter the interaction forces between protein molecules, thereby affecting their folding, stability, and overall functionality.

To gain further information we decided to exploit the spectroscopic properties of ACDAN. This dye is emerging as a tool [92, 93, 94, 96, 97, 163] to assess the changes of structure of water structure in the sample during the LLPS transition. In recent work, it was used in cellular environment both in vitro [92] and in vivo [94]. Simpler studies in model systems to the best of our knowledge allowing a more detailed understanding of its solvatochromic properties are not reported yet. ACDAN dye fluorescence was used to follow occurring events during the temperature scan giving insight on the role of solvent order. Moreover, the contributions of the different phases were analysed revealing in line with expectations that water order is increased in the concentrated phase. Interestingly it was observed that even if the volume fraction of the concentrated is very small (about 5% of the total volume), its contribution is the highest suggesting that LLPS is per se entropically unfavourable. The presented experiments reveal the quite complex behaviour of this dye and highlight experimental details to be taken into account during the experiments, specifically, data reveal that protein hydrophobic cavities may sequestrate dye molecules affecting observed fluorescence signal changes. In line with previous studies on other DAN dyes like LAURDAN, we decided to analyse ACDAN fluorescence lifetime by means of phasor approach. Based on the analysis of the system, we developed a model to interpret changes in fluorescence lifetime. This model allows us to disentangle the potential contributions of polarity effects, specifically the number of water molecules surrounding the dye, and the effects of solvent

relaxation. This clarified that the primary factor influencing LLPS is solvent relaxation and the consequent changes in its structure, rather than the minor variations in polarity observed during the process.

In Chapter 4, a study on the formation of spherical Human Insulin microparticles in sub-microliter scale aqueous compartments is reported. An experimental setup was optimised to analyse protein association phenomena using quantitative fluorescence microscopy methods in water droplets with hemispherical shapes deposited on a glass coverslip. Within aqueous droplets, it was possible to elucidate the formation of round amyloid-like structures at room temperature catalysed by the surface upon which they are cast at room temperature. Interestingly these insulin supramolecular assemblies are characterised by a solid core surrounded by a fluid-like corona. Their formation is driven by a liquid-liquid phase separation process and initiated by nucleation occurring at the interface between the aqueous compartment and the glass. The analysis of this peculiar assembly phenomena allowed revealing the effect of sample reduced volume and reduced diffusion effects which are neglectable in experiments performed in large volume samples above the microliter scale. Indeed, at the same solution conditions significant aggregation is not observed. The experimental setup which allows performing fluorescence imaging, FRAP and FLIM experiments allow determining the physical state of the particles and details of molecular structures Interestingly these microparticles share some feature with both the particulates (size and amyloid-like structure) and spherulites (heterogeneous core-corona structure). The insulin microparticles grow from fixed nuclei at the glass interface forming the solid core. Then the protein molecules condensate around these nucleation points heterogeneously distributed at the glass surface. The observed process was also rationalised by means of a simplified mathematical model, which indicates how the nucleation is driven by the free diffusion of HI molecules within the aqueous compartment. It was observed how the process slowed down in larger aqueous compartments. Interestingly according to the recent model [32, 41, 43, 44, 45**?**] this only affect the primary nucleation since the major observable difference is associated to the duration of the lag phase of the kinetics measured in aqueous drop with different sizes. The drop size also affects the size and structure of the microparticles. Larger microparticles form in larger drops due to the higher volume and therefore to the higher number of molecules in solution (measurements are performed at constant concentration). Microparticles which occur in smaller drops are small and present a less affine binding sites for ThT indicating a more native-like structure, and a lower viscosity and rigidity of the molecular environment experienced by the fluorophore.

The observed protein microparticles display amyloid-like properties and interestingly share similarities with amyloid superstructures formed in diverse conditions. These structures have a size and shape that closely match protein particulates, characterized by a dense solid core surrounded by a fluid-like corona, similar to the structure of protein spherulites. This demonstrates that proteins have the ability to form common molecular structures even when exposed to different environmental conditions. This highlights the existence of general principles that govern these processes.

In the Appendix A preliminary results from X-ray Photon Correlation Spectroscopy (XPCS) data acquired at ESRF, in Grenoble are reported. Data are aimed at analysing the experiment feasibility replicating a recently published work by Girelli et al. [176] on the LLPS of γ globulin in presence of PEG and under thermal treatment in similar conditions to what was reported in Chapter 3. The preliminary results are qualitatively in line with the one reported by Girelli et al. [176]. Once the experimental setup's reliability is verified, our aim is to investigate the LLPS process outlined in Chapter 3. We anticipate that this process will exhibit a dynamic behaviour distinct from the one described in this appendix, potentially offering insights into various LLPS processes.

In conclusion, in the presented study the importance of environmental conditions has been highlighted. In particular, physico-chemical conditions such as temperature, excluded volume and molecular crowding, the presence of co-solutes, the presence of surfaces, and the reduction of reaction volume have been reported and investigated. It has been shown how all these conditions can significantly impact intermolecular interactions and, consequently, influence LLPS processes and protein aggregation.

Aggregation and LLPS are inherently complex phenomena, given that the key players involved are equally intricate. In this study, we aimed to highlight the similarities between these two processes, which ultimately result in similar forms of molecular association (both morphologically and structurally) under appropriate experimental conditions, despite being vastly different. As previously noted, this is believed to be due to the fact that similar interactions govern both processes, albeit to varying extents. Having a clear understanding of these interactions allows us to harness these protein associations for a wide range of purposes, from drug delivery systems [24, 177] to biosensing applications [153].

An experimental approach based on the findings reported in this thesis could enable the study of cellular processes and cell compartmentalization using simpler model systems, gradually increasing their complexity to mimic cellular environ-

ments as closely as possible. This would allow us to tune and manipulate all system properties according to the experimental conditions required.

Appendices

Preliminary results of X-ray Photon Correlation Spectroscopy measurements

The following work is the result of experiments conducted at the European Synchrotron Radiation Facility (ESRF) in Grenoble, France, during a six-month international research period undertaken as part of my Ph.D. The research was carried out under the supervision of Dr. Marco Cammarata and in collaboration with Dr. Giorgio Schirò. The experiments reported below were performed at the ID10 beamline, which is a high brilliance beamline, specialized in coherent Small-Angle X-ray Scattering (SAXS) and X-ray Photon Correlation Spectroscopy (XPCS). After an introduction on XPCS, preliminary results of the performed experiments will be reported.

A.1 INTRODUCTION

X-ray Photon Correlation Spectroscopy (XPCS) is a coherent X-ray scattering technique used to characterize dynamics of condensed and soft matter in bulk in a spatial scale ranging from nanometres to micrometres and in a temporal scale which ranges between microseconds to hours [178, 179, 180, 181]. Consequently, XPCS is perfectly suited for investigating slow nanoscale dynamics within the bulk. It can access length scales that visible-light probes cannot reach, and time scales beyond the capability of inelastic X-ray or neutron scattering techniques, which are typically inaccessible with most scanning probes [178, 179]. An additional advantage of XPCS is its ability to probe samples characterized by a high number of scatters and therefore opaque solution.

XPCS is based on the same principle as the more commonly known Dynamic Light Scattering technique, but it uses coherent X-rays instead of visible light. Figure A.1 shows a schematic representation of a XPCS experiment.

At a given time, the X-ray beam hits the sample, resulting in the formation of diffraction patterns. These are acquired by the detector over time. Each diffraction pattern image is a frame and it corresponds to an image of the sample in the reciprocal space measured over the scattering vector $\mathbf{q}$. The unique pattern of peak
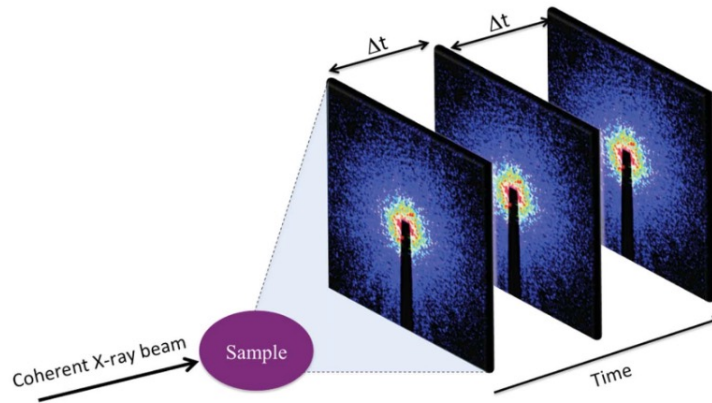
FIGURE A.1: *Schematic experimental procedure for XPCS measurement. A coherent X-ray source beam hits the sample. The detector acquires various diffraction patterns (frames) over time in the reciprocal space. The diffraction patterns have a spherical symmetry, and the speckles are the intensity fluctuation. Δt is the time between the acquisition of two consecutive frames. Figure adapted from [178].*

positions and intensities acts as a fingerprint of the chemical species. If the sample is spatially homogeneous the diffraction patterns have a spherical symmetry as the one shown in Figure A.1. The azimuthal integration of the signal is the average of the signal in function of the radius, and it gives out the standard SAXS measurement.
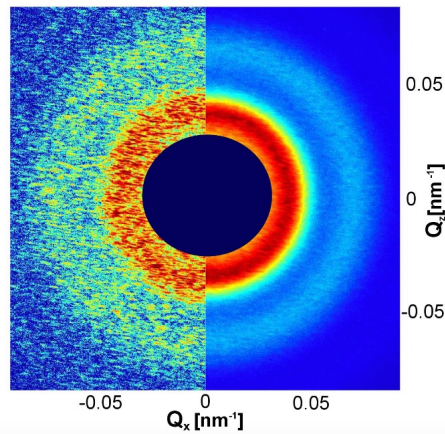

FIGURE A.2: *X-ray diffraction pattern from a colloidal sample. On the left, it is shown the diffraction pattern which occurs from a single coherent impulse. The evident intensity fluctuations are the speckles. On the right, the diffraction pattern from a sum of 50 coherent impulses which are equivalent to an uncoherent beam. The speckles are not visible. The circular shadow at the centre of the image is the beam stop. Figure adapted from [180].*

When a scattering experiment is conducted under coherent conditions, the resulting scattering pattern displays random interferences known as speckles, which are the intensity fluctuations shown in the left side of Figure A.2. The speckles are not visible in the diffraction patterns which occur from an incoherent beam (see

right side of Figure A.2. These are the most important features in a XPCS measurement since the information about the dynamics of the system is obtained by analysing how the speckles change over time [178, 179, 180, 181]. Also, the linear size of the speckles is proportional to the distance of the detector from the sample, and on the radiation wavelength, and it is inversely proportional to the width of the beam which impinges on the sample. XPCS quantifies the fluctuations of the speckle intensity in function of time by calculating the intensity autocorrelation function $g_2(\mathbf{q}, \tau)$:

$$g_2(\mathbf{q}, \tau) = \frac{\langle I(\mathbf{q}, t)I(\mathbf{q}, t + \tau)\rangle_T}{\langle l(\mathbf{q}, t)\rangle_T^2} \tag{A.1}$$

where τ is the delay between two consecutive frames (denoted as Δt in Figure A.1) and $\langle \ldots \rangle_T$ is the ensemble average over all the acquisition time T in a given pixel, or region of pixels on the detector area. $I(\mathbf{q}, t)$ and $I(\mathbf{q}, t + \tau)$ are the intensities in each pixel of the frames, taken at times t and $t + \tau$, respectively, averaged over all the t, while keeping the delay time τ constant. The $g_2(\mathbf{q}, \tau)$ can also be written as:

$$g_2(\mathbf{q}, \tau) = 1 + \beta(\mathbf{q})|f(\mathbf{q}, t)|^2 \tag{A.2}$$

The factor $\beta(\mathbf{q})$ is the speckle contrast expected for a static sample and $f(\mathbf{q}, t)$ is the intermediate scattering function which reflects the time dependence of the electronic density correlation within the sample. In general, it is exponential decay with a characteristic relaxation time constant. If the spatial arrangement of scatterers within the sample varies over time, the resulting speckle pattern will also undergo changes. By measuring the intensity fluctuations of these speckles, the underlying dynamics of the sample can be uncovered.

Many XPCS studies are focused on the analysis of equilibrium fluctuation dynamics. Recently this technique was also used to investigate the non-equilibrium dynamics of evolving processes such as phase transitions.

To achieve this, an excellent tool for quantitative data analysis is the Two-Times Correlation (TTC) function.

$$C(t_1, t_2, \mathbf{q}) = \frac{\langle I(\mathbf{q}, t_1)I(\mathbf{q}, t_2)\rangle}{\langle I(\mathbf{q}, t_1)\rangle\langle I(\mathbf{q}, t_2)\rangle} \tag{A.3}$$

where $\langle...\rangle$ is an average over pixels corresponding to a specific $\mathbf{q}$ range in which the correlation is expected to be equivalent.

From the TTC function, a TTC map can be obtained, providing a graphical visualization of the data. In Figure A.3 a representative of a TTC map is reported. The shown TTC is obtained for LLPS of a lysozyme solution induced by pressure.
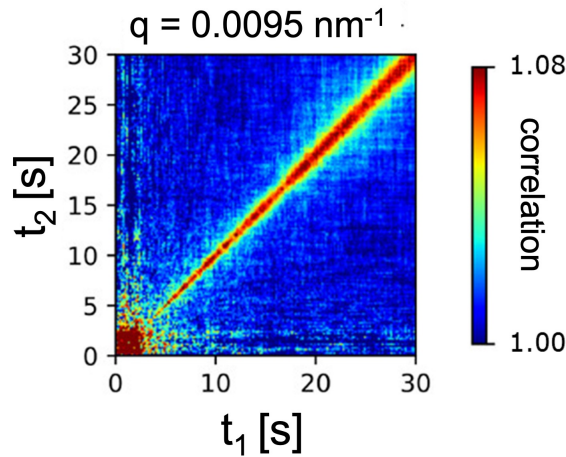
113

FIGURE A.3: *A representative Two-Times Correlation (TTC) maps of LLPS process undergone by a lysozyme solution during a pressure jump. The TTC is measured at a single* **q**. *Figure adapted from [52].*

The red colour indicates a high autocorrelation value and the blue low autocorrelation value. The TTC is symmetrical with respect to the red diagonal. The thickness of the red diagonal is an indication of the correlation time, which becomes larger with time. This denotes the slowdown of the fluctuation and therefore of the system dynamics. The broadening of the TTC is a unique fingerprint of the dynamical slowdown of the process [179, 182].

Some studies have begun to explore the possibility of investigating the changing dynamics of proteins during LLPS phenomena by means of XPCS. The spatial and temporal window it covers is indeed ideal for studying LLPS processes [52, 176, 181, 182].

Our work at ESRF in Grenoble has focused on replicating an experiment whose results were recently published by Girelli et al. [176], in order to demonstrate our ability to reproduce those findings. It's worth noting that the original experiment conducted by Girelli et al. [176] took place at the PETRA III synchrotron.

A.2 EXPERIMENTAL RESULTS AND DISCUSSION

The work by Girelli et al. [176] stands out being among the first studies which successfully employed XPCS to investigate LLPS. They have demonstrated that a combination of experimental conditions (scanning techniques, large source beams, and a long distance between sample and detector) significantly reduces the X-ray dose, thus preventing sample degradation and allowing for the measurement to be performed. In particular, they investigated the thermal-induced LLPS of γ globulin

in presence of PEG 1000 as molecular crowder. This paper is based on another work by Da Vela et al. [53] who investigated the LLPS in the same sample by means of Ultra Small Angle X-ray Scattering (USAXS) and Very Small Angle Neutron Scattering (VSANS).
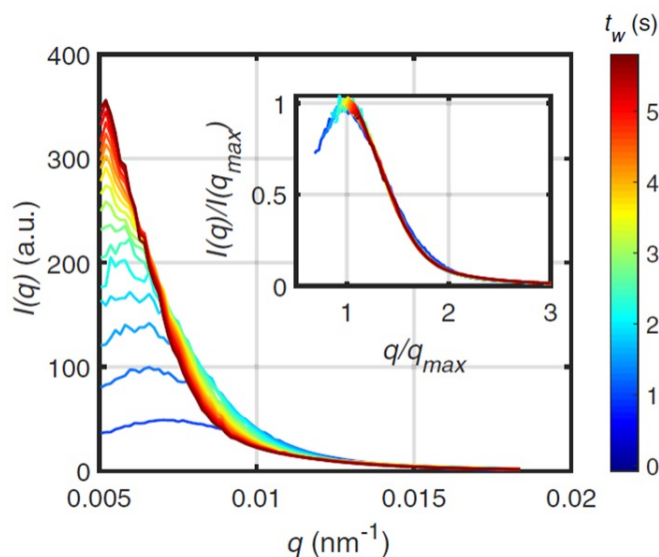

FIGURE A.4: *Scattering intensity as a function of the scattering* **q**, *for quench temperature $T_q = 10°C$. The scattering intensity increases as a function of time. The inset shows the same data in a different scale to show the shift of the peak towards smaller values of* **q**. *Figure adapted from Girelli et al. [176].*

Here, published data from Girelli et al. [176] will be briefly discussed, as a reference to the preliminary results from the data acquired in ESRF.

The sample consists of 110 mg/ml γ globulin, 90 mg/ml PEG 1000 and 150 mM NaCl. The solution is prepared in 20 mM HEPES at pH 7.0. The sample thus prepared undergoes LLPS above room temperature. To avoid the deposition of the sample during the measurements, the sample was incubated at room temperature for 24 hours. This allows the dense phase to sediment on the bottom of the vial and to separate it from the diluted phase. The dense phase is collected in a quartz capillary (1.5 mm in diameter) and the XPCS measurements were performed on the dense phase. Aside from the size of the capillary and centrifugation time or speed, which are not specified in Girelli's paper, the same procedure was followed. The measurements were performed rapidly decreasing the temperature of the sample to inducing LLPS. The effect of the quench temperature T_q (the final temperature of the temperature scan) was analysed as well.

Figure A.4 shows the scattering intensity as a function of the scattering vector **q** for the $T_q = 10°C$, and the inset shows the data rescaled. After the T_q, scattering intensity increases as a function of time and the peak shifts towards smaller values of

115

q. Since in general proteins have a higher cross section for X-ray elastic scattering the increase of the intensity scattering intensity indicates the presence of concentration fluctuation of protein molecules in the solution denoting the beginning of the LLPS process. The shifting of the peak to smaller values indicates the growth of this protein-rich domain.
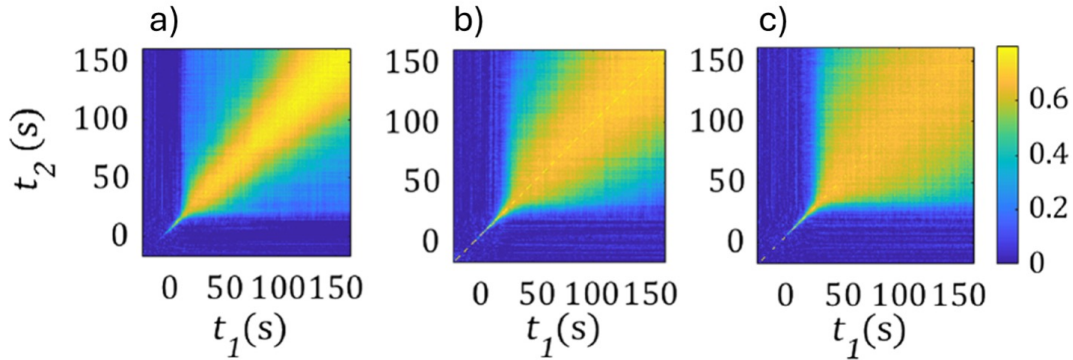

FIGURE A.5: *TTC maps measured at q = 0.005 nm^{-1} for three different quench temperatures: a) 15°C, b) 8°C, c) 4°C. Blue indicates a low correlation and yellow indicates a high correlation. Figure adapted from Girelli et al. [176].*

Figure A.5 shows the TTC maps measured $q = 0.005$ nm^{-1} for three different quench temperature: a) 15°C, b) 8°C, c) 4°C. In these TTC maps is possible to observe two distinct stages of the protein dynamics during LLPS process. From 0 s to about 40 s only a thin line is visible in the TTC maps, indicating a fast dynamic. After this first stage slight slowdown of the system can be observed as the line begins to thicken and this process culminates in a pronounced slowdown that is accompanied by the appearance of this square-like feature due to the increase of the background value. This process appears to be dependent on the quench temperature, being more prominent for lower temperatures. This is due to an arrested dynamics which indicates that when the system is deeply quenched, it is in a gel-like state, causing the arrested dynamics.

Preliminary data acquired at the ESRF will be now reported. Results are qualitatively in line with what was shown until now, both by Girelli et al. [176] and Da Vela et al. [53].

Figure A.6 shows the scattering intensity of the sample reported as a function of the scattering vector **q** for two quench temperatures: a) T$_q$ = 5°C and b) T$_q$ = 0°C. The scattering intensity increases as a function of time for both the quench temperature. Interestingly, differently to what was reported by Girelli et al. [176], the scattering intensity reaches higher values for lower quench temperature. This indicates that at lower quench temperatures, the protein concentration within the protein-rich domain is higher and therefore the condensates which are forming are
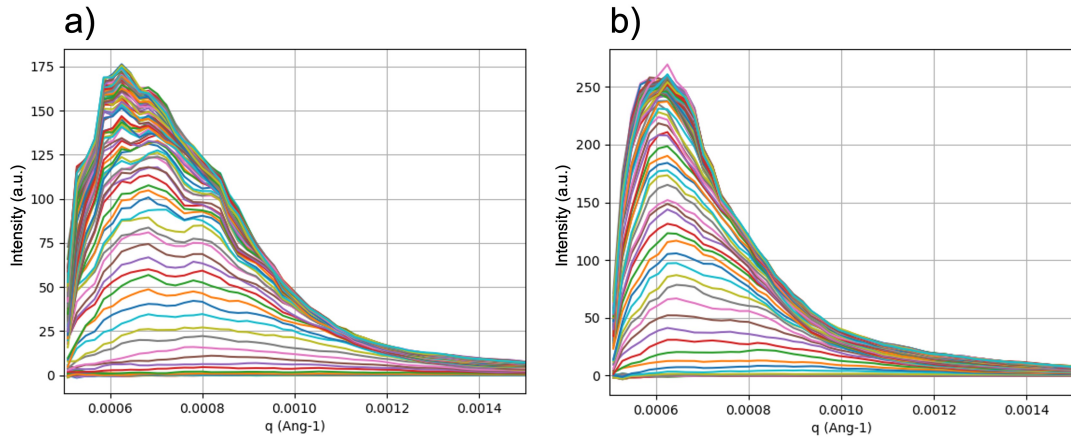
Figure A.6: *Scattering intensity reported as a function of the scattering* **q**, *for two quench tempera-ture: a)* $T_q = 5°C$ *and b)* $T_q = 0°C$. *The scattering intensity increases as a function of time.*

denser. Moreover, in this case, no shift of the scattering data is visible. This is prob-ably due to the fact that the experimental setup does not allow for high resolution at low **q**, because of the short distance between the sample and the detector, which is about 7 meters.
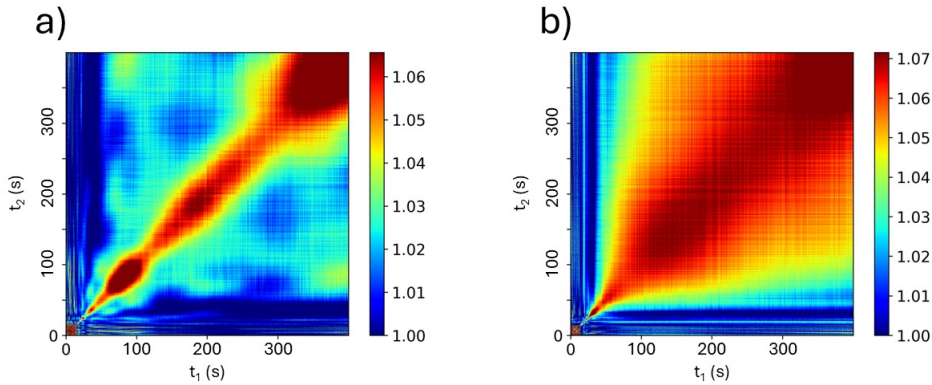
Figure A.7: *TTC maps measured at* $q = 0.01$ nm^{-1} *for two quench temperatures: a)* $5°C$ *and b)* $0°C$. *Blue indicates a low correlation and red indicates a high correlation. At* $5°C$ *the phase separation occurs showing a faster dynamic than the one observed at* $0°C$.

Figure A.7 shows the TTC maps measured at $q = 0.01$ nm^{-1} for a) 5°C and b) 0°C quench temperature. The results are in line with what was observed by [176]. After about 10 seconds from the start of the experiment, a thin line appears in the TTC maps, indicating a slight slowdown of protein dynamics and the beginning of LLPS process. The arrested dynamic of the system occurs at about 50 seconds from the beginning of the experiment, as evident from the square-like feature presented in the TTC maps reported. In line with the results reported by [176], the arrested dynamics obtained for 5°C quench temperature (Figure A.7a) is less pronounced than the one obtained for 0°C quench temperature (Figure A.7b).

117

Differently to the data reported by Girelli et al. [176], the solution does not undergo LLPS for temperatures above 5°C. This may be due to differences in the sample preparation or to a slower temperature-quenching system (temperature rate is about 60°C/min). However, from a qualitative point of view, the built experimental setup allows for replication of the data.

A.3 CONCLUSIONS

The presented chapter shows some preliminary data acquired at the ESRF (European Synchrotron Radiation Facility). The use of XPCS for investigating LLPS is a novel approach to analyse this phenomenon, allowing to study the protein dynamic during LLPS. XPCS is ideal to explore LLPS processes due to its spatio-temporal scale of acquisition. Moreover, it can investigate opaque samples with a high number of scatterers that are difficult to probe by optical measurements.

Data published by Girelli et al. [176] about the thermal-induced LLPS of γ globulin solution were replicated in order to assess if the experimental setup built at the ESRF ID10 beamline yields good results. Our preliminary results from ESRF align qualitatively with those reported by Girelli et al. [176]. By means of the TTC function, the same specific protein arrested dynamics were observed during the LLPS transition. It was also observed that protein dynamic and the overall process depends on the quench temperature set to the system.

Some differences were also noted. Specifically, our data indicated higher scattering intensities at lower quench temperatures, suggesting that the protein concentration within the dense phase increases as the temperature decreases. However, we did not observe a shift in the scattering peak, likely due to the limitations of our experimental setup.

XPCS has the potential to elucidate the intricacies of protein dynamics in crowded environments and during phase transitions. This technique offers the exciting possibility of time-resolved imaging of functionally significant processes. These include protein aggregation, self-assembly, and LLPS processes. XPCS may provide valuable insights into these complex biological processes.

Bibliography

[1] B. Alberts, A. Johnson, J. Lewis, P. Walter, M. Raff, and K. Roberts. *Molecular Biology of the Cell 4th Edition: International Student Edition*. Routledge, 2002. ISBN 9780815332886. URL `https://books.google.it/books?id=ozigkQEACAAJ`.

[2] Alexei V. Finkelstein and Oleg B. Ptitsyn. Copyright. In *Protein Physics (Second Edition)*. Academic Press, Amsterdam, second edition edition, 2016. ISBN 978-0-12-809676-5. doi: https://doi.org/10.1016/B978-0-12-809676-5.

[3] Matthew Fisher. Lehninger principles of biochemistry, 3rd edition; by david l. nelson and michael m. cox. *The Chemical Educator*, 6(1):69–70, Feb 2001. ISSN 1430-4171. doi: 10.1007/s00897000455a. URL `https://doi.org/10.1007/s00897000455a`.

[4] Ken A. Dill. Dominant forces in protein folding. *Biochemistry*, 29(31): 7133–7155, 1990. doi: 10.1021/bi00483a001. URL `https://doi.org/10.1021/bi00483a001`. PMID: 2207096.

[5] David Chandler. Interfaces and the driving force of hydrophobic assembly. *Nature*, 437(7059):640–647, Sep 2005. ISSN 1476-4687. doi: 10.1038/nature04162. URL `https://doi.org/10.1038/nature04162`.

[6] George Némethy, Izchak Z. Steinberg, and Harold A. Scheraga. Influence of water structure and of hydrophobic interactions on the strength of side-chain hydrogen bonds in proteins. *Biopolymers*, 1(1):43–69, 1963. doi: https://doi.org/10.1002/bip.360010107. URL `https://onlinelibrary.wiley.com/doi/abs/10.1002/bip.360010107`.

[7] David Balchin, Manajit Hayer-Hartl, and F. Ulrich Hartl. In vivo aspects of protein folding and quality control. *Science*, 353(6294):aac4354, 2016. doi: 10.1126/science.aac4354. URL `https://www.science.org/doi/abs/10.1126/science.aac4354`.

[8] Jozef Adamcik and Raffaele Mezzenga. Amyloid polymorphism in the protein folding and aggregation energy landscape. *Angewandte Chemie International Edition*, 57(28):8370–8382, 2018. doi: https://doi.org/10.1002/anie.201713416. URL `https://onlinelibrary.wiley.com/doi/abs/10.1002/anie.201713416`.

[9] Yujin E Kim, Mark S Hipp, Andreas Bracher, Manajit Hayer-Hartl, and F Ulrich Hartl. Molecular chaperone functions in protein folding and proteostasis. *Annu. Rev. Biochem.*, 82(1):323–355, June 2013.

[10] D. Thirumalai and G. Reddy. Are native proteins metastable? *Nature Chemistry*, 3(12):910–911, Dec 2011. ISSN 1755-4349. doi: 10.1038/nchem. 1207. URL `https://doi.org/10.1038/nchem.1207`.

[11] Andrew J. Baldwin, Tuomas P. J. Knowles, Gian Gaetano Tartaglia, Anthony W. Fitzpatrick, Glyn L. Devlin, Sarah Lucy Shammas, Christopher A. Waudby, Maria F. Mossuto, Sarah Meehan, Sally L. Gras, John Christodoulou, Spencer J. Anthony-Cahill, Paul D. Barker, Michele Vendruscolo, and Christopher M. Dobson. Metastability of native proteins and the phenomenon of amyloid formation. *Journal of the American Chemical Society*, 133(36):14160–14163, 2011. doi: 10.1021/ja2017703. URL `https://doi.org/10.1021/ja2017703`. PMID: 21650202.

[12] Rebecca Nelson, Michael R. Sawaya, Melinda Balbirnie, Anders Ø. Madsen, Christian Riekel, Robert Grothe, and David Eisenberg. Structure of the cross-β spine of amyloid-like fibrils. *Nature*, 435(7043):773–778, Jun 2005. ISSN 1476-4687. doi: 10.1038/nature03680. URL `https://doi.org/10.1038/nature03680`.

[13] Michael R. Sawaya, Shilpa Sambashivan, Rebecca Nelson, Magdalena I. Ivanova, Stuart A. Sievers, Marcin I. Apostol, Michael J. Thompson, Melinda Balbirnie, Jed J. W. Wiltzius, Heather T. McFarlane, Anders Ø. Madsen, Christian Riekel, and David Eisenberg. Atomic structures of amyloid cross-β spines reveal varied steric zippers. *Nature*, 447(7143):453–457, May 2007. ISSN 1476-4687. doi: 10.1038/nature05695. URL `https://doi.org/10.1038/nature05695`.

[14] Catharine Shipps, H. Ray Kelly, Peter J. Dahl, Sophia M. Yi, Dennis Vu, David Boyer, Calina Glynn, Michael R. Sawaya, David Eisenberg, Victor S. Batista, and Nikhil S. Malvankar. Intrinsic electronic conductivity of individual atomically resolved amyloid crystals reveals micrometer-long hole hopping via tyrosines. *Proceedings of the National Academy of Sciences*, 118(2):e2014139118, 2021. doi: 10.1073/pnas.2014139118. URL `https://www.pnas.org/doi/abs/10.1073/pnas.2014139118`.

[15] C. Bortolini, N. C. Jones, S. V. Hoffmann, C. Wang, F. Besenbacher, and M. Dong. Mechanical properties of amyloid-like fibrils defined by secondary

structures. *Nanoscale*, 7:7745–7752, 2015. doi: 10.1039/C4NR05109B. URL `http://dx.doi.org/10.1039/C4NR05109B`.

[16] Yajuan Wang, Yanting Shen, Guangyan Qi, Ya Li, Xiuzhi Susan Sun, Dan Qiu, and Yonghui Li. Formation and physicochemical properties of amyloid fibrils from soy protein. *International Journal of Biological Macromolecules*, 149:609–616, 2020. ISSN 0141-8130. doi: https://doi.org/10.1016/j.ijbiomac.2020.01.258. URL `https://www.sciencedirect.com/science/article/pii/S0141813019367947`.

[17] Maria Giovanna Di Carlo, Valeria Vetri, Gianpiero Buscarino, Maurizio Leone, Bente Vestergaard, and Vito Foderà. Trifluoroethanol modulates α-synuclein amyloid-like aggregate formation, stability and dissolution. *Biophysical Chemistry*, 216:23–30, 2016. ISSN 0301-4622. doi: https://doi.org/10.1016/j.bpc.2016.06.003. URL `https://www.sciencedirect.com/science/article/pii/S0301462216300679`.

[18] Vito Foderà, Alessio Zaccone, Marco Lattuada, and Athene M. Donald. Electrostatics controls the formation of amyloid superstructures in protein aggregation. *Phys. Rev. Lett.*, 111:108105, Sep 2013. doi: 10.1103/PhysRevLett.111.108105. URL `https://link.aps.org/doi/10.1103/PhysRevLett.111.108105`.

[19] Valeria Vetri and Vito Foderà. The route to protein aggregate superstructures: Particulates and amyloid-like spherulites. *FEBS Letters*, 589 (19PartA):2448–2463, 2015. doi: https://doi.org/10.1016/j.febslet.2015.07.006. URL `https://febs.onlinelibrary.wiley.com/doi/abs/10.1016/j.febslet.2015.07.006`.

[20] Sara Anselmo, Giuseppe Sancataldo, Vito Foderà, and Valeria Vetri. α-casein micelles-membranes interaction: Flower-like lipid protein coaggregates formation. *Biochim. Biophys. Acta Gen. Subj.*, 1866(10):130196, October 2022.

[21] Valeria Vetri, Federica Piccirilli, Johannes Krausser, Gianpiero Buscarino, Urszula Łapińska, Bente Vestergaard, Alessio Zaccone, and Vito Foderà. Ethanol controls the self-assembly and mesoscopic properties of human insulin amyloid spherulites. *The Journal of Physical Chemistry B*, 122(12): 3101–3112, 2018. doi: 10.1021/acs.jpcb.8b01779. URL `https://doi.org/10.1021/acs.jpcb.8b01779`. PMID: 29488762.

[22] Mark R H Krebs, Glyn L Devlin, and A M Donald. Protein particulates: Another generic form of protein aggregation? *Biophys. J.*, 92(4):1336–1342, February 2007.

[23] Vito Foderà, Valeria Vetri, Thea S. Wind, Wim Noppe, Claus Cornett, Athene M. Donald, Ludmilla A. Morozova-Roche, and Bente Vestergaard. Observation of the early structural changes leading to the formation of protein superstructures. *The Journal of Physical Chemistry Letters*, 5(18):3254–3258, 2014. doi: 10.1021/jz501614e. URL https://doi.org/10.1021/jz501614e. PMID: 26276341.

[24] Dirk Fennema Galparsoro, Xin Zhou, Anas Jaaloul, Federica Piccirilli, Valeria Vetri, and Vito Foderà. Conformational transitions upon maturation rule surface and ph-responsiveness of α-lactalbumin microparticulates. *ACS Applied Bio Materials*, 4(2):1876–1887, 2021. doi: 10.1021/acsabm.0c01541. URL https://doi.org/10.1021/acsabm.0c01541. PMID: 35014457.

[25] S M Vaiana, M B Palma-Vittorelli, and M U Palma. Time scale of protein aggregation dictated by liquid-liquid demixing. *Proteins*, 51(1):147–153, April 2003.

[26] Simon Alberti, Amy Gladfelter, and Tanja Mittag. Considerations and challenges in studying liquid-liquid phase separation and biomolecular condensates. *Cell*, 176(3):419–434, 2019. ISSN 0092-8674. doi: https://doi.org/10.1016/j.cell.2018.12.035. URL https://www.sciencedirect.com/science/article/pii/S0092867418316490.

[27] Andreas Barth. Infrared spectroscopy of proteins. *Biochimica et Biophysica Acta (BBA) - Bioenergetics*, 1767(9):1073–1101, 2007. ISSN 0005-2728. doi: https://doi.org/10.1016/j.bbabio.2007.06.004. URL https://www.sciencedirect.com/science/article/pii/S0005272807001375.

[28] Giuseppe De Luca, Dirk Fennema Galparsoro, Giuseppe Sancataldo, Maurizio Leone, Vito Foderà, and Valeria Vetri. Probing ensemble polymorphism and single aggregate structural heterogeneity in insulin amyloid self-assembly. *Journal of Colloid and Interface Science*, 574:229–240, 2020. ISSN 0021-9797. doi: https://doi.org/10.1016/j.jcis.2020.03.107. URL https://www.sciencedirect.com/science/article/pii/S0021979720304082.

[29] Vito Foderà, Stefano Pagliara, Oliver Otto, Ulrich F. Keyser, and Athene M. Donald. Microfluidics reveals a flow-induced large-scale polymorphism of protein aggregates. *The Journal of Physical Chemistry Letters*, 3(19):2803–2807, 2012. doi: 10.1021/jz301375d. URL `https://doi.org/10.1021/jz301375d`.

[30] Michael I. Smith, Vito Foderà, James S. Sharp, Clive J. Roberts, and Athene M. Donald. Factors affecting the formation of insulin amyloid spherulites. *Colloids and Surfaces B: Biointerfaces*, 89:216–222, 2012. ISSN 0927-7765. doi: https://doi.org/10.1016/j.colsurfb.2011.09.018. URL `https://www.sciencedirect.com/science/article/pii/S0927776511005418`.

[31] Min Zhang, Henrik D. Pinholt, Xin Zhou, Søren S.-R. Bohr, Luca Banetta, Alessio Zaccone, Vito Foderà, and Nikos S. Hatzakis. Direct observation of heterogeneous formation of amyloid spherulites in real-time by super-resolution microscopy. *Communications Biology*, 5(1):850, Aug 2022. ISSN 2399-3642. doi: 10.1038/s42003-022-03810-1. URL `https://doi.org/10.1038/s42003-022-03810-1`.

[32] Fabio Librizzi and Christian Rischel. The kinetic behavior of insulin fibrillation is determined by heterogeneous nucleation pathways. *Protein Science*, 14(12):3129–3134, 2005. doi: https://doi.org/10.1110/ps.051692305. URL `https://onlinelibrary.wiley.com/doi/abs/10.1110/ps.051692305`.

[33] Mattias Törnquist, Thomas C. T. Michaels, Kalyani Sanagavarapu, Xiaoting Yang, Georg Meisl, Samuel I. A. Cohen, Tuomas P. J. Knowles, and Sara Linse. Secondary nucleation in amyloid formation. *Chem. Commun.*, 54:8667–8684, 2018. doi: 10.1039/C8CC02204F. URL `http://dx.doi.org/10.1039/C8CC02204F`.

[34] Fumio Oosawa and Michiki Kasai. A theory of linear and helical aggregations of macromolecules. *Journal of Molecular Biology*, 4(1):10–21, 1962. ISSN 0022-2836. doi: https://doi.org/10.1016/S0022-2836(62)80112-0. URL `https://www.sciencedirect.com/science/article/pii/S0022283662801120`.

[35] H Flyvbjerg, E Jobs, and S Leibler. Kinetics of self-assembling microtubules: an "inverse problem" in biochemistry. *Proceedings of the National Academy*

of Sciences, 93(12):5975–5979, 1996. doi: 10.1073/pnas.93.12.5975. URL `https://www.pnas.org/doi/abs/10.1073/pnas.93.12.5975`.

[36] Amy M. Ruschak and Andrew D. Miranker. Fiber-dependent amyloid formation as catalysis of an existing reaction pathway. *Proceedings of the National Academy of Sciences*, 104(30):12341–12346, 2007. doi: 10.1073/pnas. 0703306104. URL `https://www.pnas.org/doi/abs/10.1073/pnas. 0703306104`.

[37] Frank A. Ferrone, James Hofrichter, and William A. Eaton. Kinetics of sickle hemoglobin polymerization: Ii. a double nucleation mechanism. *Journal of Molecular Biology*, 183(4):611–631, 1985. ISSN 0022-2836. doi: https://doi.org/10.1016/0022-2836(85)90175-5. URL `https://www. sciencedirect.com/science/article/pii/0022283685901755`.

[38] Sean R Collins, Adam Douglass, Ronald D Vale, and Jonathan S Weissman. Mechanism of prion propagation: Amyloid growth occurs by monomer addition. *PLOS Biology*, 2(10):null, 09 2004. doi: 10.1371/journal.pbio.0020321. URL `https://doi.org/10.1371/journal.pbio.0020321`.

[39] Vito Foderà, Sebastiano Cataldo, Fabio Librizzi, Bruno Pignataro, Paola Spiccia, and Maurizio Leone. Self-organization pathways and spatial heterogeneity in insulin amyloid fibril formation. *The Journal of Physical Chemistry B*, 113(31):10830–10837, 2009. doi: 10.1021/jp810972y. URL `https://doi.org/10.1021/jp810972y`. PMID: 19588943.

[40] Vito Foderà, Fabio Librizzi, Minna Groenning, Marco van de Weert, and Maurizio Leone. Secondary nucleation and accessible surface in insulin amyloid fibril formation. *The Journal of Physical Chemistry B*, 112(12):3853–3858, 2008. doi: 10.1021/jp710131u. URL `https://doi.org/10.1021/ jp710131u`. PMID: 18311965.

[41] Paolo Arosio, Thomas C T Michaels, Sara Linse, Cecilia Månsson, Cecilia Emanuelsson, Jenny Presto, Jan Johansson, Michele Vendruscolo, Christopher M Dobson, and Tuomas P J Knowles. Kinetic analysis reveals the diversity of microscopic mechanisms through which molecular chaperones suppress amyloid formation. *Nat. Commun.*, 7(1), March 2016.

[42] Fabio Librizzi and Christian Rischel. The kinetic behavior of insulin fibrillation is determined by heterogeneous nucleation pathways. *Protein Science*, 14(12):3129–3134, 2005. doi: https://doi.org/10.1110/ps.

051692305. URL `https://onlinelibrary.wiley.com/doi/abs/10.1110/ps.051692305`.

[43] Paolo Arosio, Michele Vendruscolo, Christopher M Dobson, and Tuomas P J Knowles. Chemical kinetics for drug discovery to combat protein aggregation diseases. *Trends Pharmacol. Sci.*, 35(3):127–135, March 2014.

[44] Paolo Arosio, Tuomas P. J. Knowles, and Sara Linse. On the lag phase in amyloid fibril formation. *Phys. Chem. Chem. Phys.*, 17:7606–7618, 2015. doi: 10.1039/C4CP05563B. URL `http://dx.doi.org/10.1039/C4CP05563B`.

[45] Samuel I A Cohen, Michele Vendruscolo, Christopher M Dobson, and Tuomas P J Knowles. From macroscopic measurements to microscopic mechanisms of protein aggregation. *J. Mol. Biol.*, 421(2-3):160–171, August 2012.

[46] Edward M Courchaine, Alice Lu, and Karla M Neugebauer. Droplet organelles? *The EMBO Journal*, 35(15):1603–1612, 2016. doi: https://doi.org/10.15252/embj.201593517. URL `https://www.embopress.org/doi/abs/10.15252/embj.201593517`.

[47] Caterina Alfano, Yann Fichou, Klaus Huber, Matthias Weiss, Evan Spruijt, Simon Ebbinghaus, Giuseppe De Luca, Maria Agnese Morando, Valeria Vetri, Piero Andrea Temussi, and Annalisa Pastore. Molecular crowding: The history and development of a scientific paradigm. *Chemical Reviews*, 124(6):3186–3219, 2024. doi: 10.1021/acs.chemrev.3c00615. URL `https://doi.org/10.1021/acs.chemrev.3c00615`. PMID: 38466779.

[48] Salman F. Banani, Hyun O. Lee, Anthony A. Hyman, and Michael K. Rosen. Biomolecular condensates: organizers of cellular biochemistry. *Nature Reviews Molecular Cell Biology*, 18(5):285–298, May 2017. ISSN 1471-0080. doi: 10.1038/nrm.2017.7. URL `https://doi.org/10.1038/nrm.2017.7`.

[49] Edward Gomes and James Shorter. The molecular language of membraneless organelles. *J. Biol. Chem.*, 294(18):7115–7127, May 2019.

[50] Manisha Poudyal, Komal Patel, Laxmikant Gadhe, Ajay Singh Sawner, Pradeep Kadu, Debalina Datta, Semanti Mukherjee, Soumik Ray, Ambuja Navalkar, Siddhartha Maiti, Debdeep Chatterjee, Jyoti Devi, Riya Bera, Nitisha Gahlot, Jennifer Joseph, Ranjith Padinhateeri, and Samir K. Maji. Intermolecular interactions underlie protein/peptide phase separation irrespective

of sequence and structure at crowded milieu. *Nature Communications*, 14
(1):6199, Oct 2023. ISSN 2041-1723. doi: 10.1038/s41467-023-41864-9.
URL https://doi.org/10.1038/s41467-023-41864-9.

[51] Ying Wang, Aleksey Lomakin, Sonoko Kanai, Rainer Alex, and George B.
Benedek. Liquid–liquid phase separation in oligomeric peptide solu-
tions. *Langmuir*, 33(31):7715–7721, 2017. doi: 10.1021/acs.langmuir.
7b01693. URL https://doi.org/10.1021/acs.langmuir.7b01693.
PMID: 28689408.

[52] M. Moron, A. Al-Masoodi, C. Lovato, M. Reiser, L. Randolph, G. Surmeier,
J. Bolle, F. Westermeier, M. Sprung, R. Winter, M. Paulus, and C. Gutt.
Gelation dynamics upon pressure-induced liquid–liquid phase separation in
a water–lysozyme solution. *The Journal of Physical Chemistry B*, 126(22):
4160–4167, 2022. doi: 10.1021/acs.jpcb.2c01947. URL https://doi.
org/10.1021/acs.jpcb.2c01947. PMID: 35594491.

[53] Stefano Da Vela, Michal K. Braun, Andreas Dörr, Alessandro Greco, Jo-
hannes Möller, Zhendong Fu, Fajun Zhang, and Frank Schreiber. Kinetics of
liquid–liquid phase separation in protein solutions exhibiting lcst phase be-
havior studied by time-resolved usaxs and vsans. *Soft Matter*, 12:9334–9341,
2016. doi: 10.1039/C6SM01837H. URL http://dx.doi.org/10.1039/
C6SM01837H.

[54] Simone Pezzotti, Benedikt König, Sashary Ramos, Gerhard Schwaab, and
Martina Havenith. Liquid–liquid phase separation? ask the water! *The Jour-
nal of Physical Chemistry Letters*, 14(6):1556–1563, 2023. doi: 10.1021/
acs.jpclett.2c02697. URL https://doi.org/10.1021/acs.jpclett.
2c02697. PMID: 36745512.

[55] Sara S. Ribeiro, Nirnay Samanta, Simon Ebbinghaus, and João C. Marcos.
The synergic effect of water and biomolecules in intracellular phase sepa-
ration. *Nature Reviews Chemistry*, 3(9):552–561, Sep 2019. ISSN 2397-
3358. doi: 10.1038/s41570-019-0120-4. URL https://doi.org/10.
1038/s41570-019-0120-4.

[56] Nicholas B. Rego, Erte Xi, and Amish J. Patel. Identifying hydropho-
bic protein patches to inform protein interaction interfaces. *Proceedings
of the National Academy of Sciences*, 118(6):e2018234118, 2021. doi:
10.1073/pnas.2018234118. URL https://www.pnas.org/doi/abs/10.
1073/pnas.2018234118.

[57] Ellen M. Adams, Simone Pezzotti, Jonas Ahlers, Maximilian Rüttermann, Maxim Levin, Adi Goldenzweig, Yoav Peleg, Sarel J. Fleishman, Irit Sagi, and Martina Havenith. Local mutations can serve as a game changer for global protein solvent interaction. *JACS Au*, 1(7):1076–1085, 2021. doi: 10.1021/jacsau.1c00155. URL https://doi.org/10.1021/jacsau.1c00155. PMID: 34337607.

[58] P.J. Flory. *Principles of Polymer Chemistry*. Baker lectures 1948. Cornell University Press, 1953. ISBN 9780801401343. URL https://books.google.it/books?id=CQ0EbEkT5R0C.

[59] Jacob P. Brady, Patrick J. Farber, Ashok Sekhar, Yi-Hsuan Lin, Rui Huang, Alaji Bah, Timothy J. Nott, Hue Sun Chan, Andrew J. Baldwin, Julie D. Forman-Kay, and Lewis E. Kay. Structural and hydrodynamic properties of an intrinsically disordered region of a germ cell-specific protein on phase separation. *Proceedings of the National Academy of Sciences*, 114 (39):E8194–E8203, 2017. doi: 10.1073/pnas.1706197114. URL https://www.pnas.org/doi/abs/10.1073/pnas.1706197114.

[60] Timothy J. Nott, Evangelia Petsalaki, Patrick Farber, Dylan Jervis, Eden Fussner, Anne Plochowietz, Timothy D. Craggs, David P. Bazett-Jones, Tony Pawson, Julie D. Forman-Kay, and Andrew J. Baldwin. Phase transition of a disordered nuage protein generates environmentally responsive membraneless organelles. *Molecular Cell*, 57(5):936–947, 2015. ISSN 1097-2765. doi: https://doi.org/10.1016/j.molcel.2015.01.013. URL https://www.sciencedirect.com/science/article/pii/S1097276515000143.

[61] Amandine Molliex, Jamshid Temirov, Jihun, Maura Coughlin, Anderson P. Kanagaraj, Hong Joo Kim, Tanja Mittag, and J. Paul Taylor. Phase separation by low complexity domains promotes stress granule assembly and drives pathological fibrillization. *Cell*, 163(1):123–133, 2015. ISSN 0092-8674. doi: https://doi.org/10.1016/j.cell.2015.09.015. URL https://www.sciencedirect.com/science/article/pii/S0092867415011769.

[62] Alain A. M. André and Evan Spruijt. Liquid–liquid phase separation in crowded environments. *International Journal of Molecular Sciences*, 21 (16), 2020. ISSN 1422-0067. doi: 10.3390/ijms21165908. URL https://www.mdpi.com/1422-0067/21/16/5908.

[63] Shanta Biswas, Alison L. Hecht, Sadie A. Noble, Qingqiu Huang, Richard E. Gillilan, and Amy Y. Xu. Understanding the impacts of molecular

and macromolecular crowding agents on protein–polymer complex coac-
ervates. *Biomacromolecules*, 24(11):4771–4782, 2023. doi: 10.1021/
acs.biomac.3c00545. URL `https://doi.org/10.1021/acs.biomac.`
`3c00545`. PMID: 37815312.

[64] Sohee Park, Ryan Barnes, Yanxian Lin, Byoung-jin Jeon, Saeed Najafi,
Kris T. Delaney, Glenn H. Fredrickson, Joan-Emma Shea, Dong Soo Hwang,
and Songi Han. Dehydration entropy drives liquid-liquid phase separation by
molecular crowding. *Communications Chemistry*, 3(1):83, Jun 2020. ISSN
2399-3669. doi: 10.1038/s42004-020-0328-8. URL `https://doi.org/`
`10.1038/s42004-020-0328-8`.

[65] Allen P. Minton. Excluded volume as a determinant of macromolecular
structure and reactivity. *Biopolymers*, 20(10):2093–2120, 1981. doi: https:
//doi.org/10.1002/bip.1981.360201006. URL `https://onlinelibrary.`
`wiley.com/doi/abs/10.1002/bip.1981.360201006`.

[66] Apratim Dhar, Antonios Samiotakis, Simon Ebbinghaus, Lea Nienhaus, Di-
rar Homouz, Martin Gruebele, and Margaret S. Cheung. Structure, func-
tion, and folding of phosphoglycerate kinase are strongly perturbed by
macromolecular crowding. *Proceedings of the National Academy of Sci-
ences*, 107(41):17586–17591, 2010. doi: 10.1073/pnas.1006760107. URL
`https://www.pnas.org/doi/abs/10.1073/pnas.1006760107`.

[67] Kenji Sasahara, Peter McPhie, and Allen P. Minton. Effect of dextran on
protein stability and conformation attributed to macromolecular crowding.
Journal of Molecular Biology, 326(4):1227–1237, 2003. ISSN 0022-2836.
doi: https://doi.org/10.1016/S0022-2836(02)01443-2. URL `https://www.`
`sciencedirect.com/science/article/pii/S0022283602014432`.

[68] D.M. Lawler. Spectrophotometry | turbidimetry and nephelometry. In Paul
Worsfold, Alan Townshend, and Colin Poole, editors, *Encyclopedia of An-
alytical Science (Second Edition)*, pages 343–351. Elsevier, Oxford, sec-
ond edition edition, 2005. ISBN 978-0-12-369397-6. doi: https://doi.org/
10.1016/B0-12-369397-7/00718-4. URL `https://www.sciencedirect.`
`com/science/article/pii/B0123693977007184`.

[69] Gerald. Oster. The scattering of light and its applications to chemistry.
Chemical Reviews, 43(2):319–365, 1948. doi: 10.1021/cr60135a005. URL
`https://doi.org/10.1021/cr60135a005`. PMID: 18887959.

[70] Sara Anselmo, Giuseppe De Luca, Vittorio Ferrara, Bruno Pignataro, Giuseppe Sancataldo, and Valeria Vetri. Insight into mechanisms of creatinine optical sensing using fluorescein-gold complex. *Methods Appl. Fluoresc.*, 10(4):045003, October 2022.

[71] Fábio Henrique dos Santos Rodrigues, Gonzalo Garcia Delgado, Thyerre Santana da Costa, and Ljubica Tasic. Applications of fluorescence spectroscopy in protein conformational changes and intermolecular contacts. *BBA Advances*, 3:100091, 2023. ISSN 2667-1603. doi: https://doi.org/10. 1016/j.bbadva.2023.100091. URL `https://www.sciencedirect.com/ science/article/pii/S2667160323000200`.

[72] Joseph Lakowicz. *Principles of Fluorescence Spectroscopy*, volume 1. 01 2006. ISBN 978-0-387-31278-1. doi: 10.1007/978-0-387-46312-4.

[73] Valeria Vetri, Claudio Canale, Annalisa Relini, Fabio Librizzi, Valeria Militello, Alessandra Gliozzi, and Maurizio Leone. Amyloid fibrils formation and amorphous aggregation in concanavalin a. *Biophys. Chem.*, 125(1): 184–190, January 2007.

[74] Matthew Biancalana and Shohei Koide. Molecular mechanism of Thioflavin-T binding to amyloid fibrils. *Biochim. Biophys. Acta Proteins Proteom.*, 1804 (7):1405–1412, July 2010.

[75] Christian Beyschau Andersen, Hisashi Yagi, Mauro Manno, Vincenzo Martorana, Tadato Ban, Gunna Christiansen, Daniel Erik Otzen, Yuji Goto, and Christian Rischel. Branching in amyloid fibril growth. *Biophys. J.*, 96(4): 1529–1536, February 2009.

[76] Vitali I. Stsiapura, Alexander A. Maskevich, Valery A. Kuzmitsky, Konstantin K. Turoverov, and Irina M. Kuznetsova. Computational study of thioflavin t torsional relaxation in the excited state. *The Journal of Physical Chemistry A*, 111(22):4829–4835, 2007. doi: 10.1021/jp070590o. URL `https://doi.org/10.1021/jp070590o`. PMID: 17497763.

[77] Vitali I. Stsiapura, Alexander A. Maskevich, Valery A. Kuzmitsky, Vladimir N. Uversky, Irina M. Kuznetsova, and Konstantin K. Turoverov. Thioflavin t as a molecular rotor: Fluorescent properties of thioflavin t in solvents with different viscosity. *The Journal of Physical Chemistry B*, 112(49):15893–15902, 2008. doi: 10.1021/jp805822c. URL `https: //doi.org/10.1021/jp805822c`. PMID: 19367903.

[78] Mantas Ziaunys, Andrius Sakalauskas, and Vytautas Smirnovas. Identifying insulin fibril conformational differences by thioflavin-t binding characteristics. *Biomacromolecules*, 21(12):4989–4997, 2020. doi: 10.1021/acs.biomac.0c01178. URL `https://doi.org/10.1021/acs.biomac.0c01178`. PMID: 33201685.

[79] Chun Wu, Zhixiang Wang, Hongxing Lei, Yong Duan, Michael T. Bowers, and Joan-Emma Shea. The binding of thioflavin t and its neutral analog bta-1 to protofibrils of the alzheimer's disease aβ16–22 peptide probed by molecular dynamics simulations. *Journal of Molecular Biology*, 384(3):718–729, 2008. ISSN 0022-2836. doi: https://doi.org/10.1016/j.jmb.2008.09.062. URL `https://www.sciencedirect.com/science/article/pii/S0022283608012205`.

[80] David J. Lindberg, Moa S. Wranne, Mélina Gilbert Gatty, Fredrik Westerlund, and Elin K. Esbjörner. Steady-state and time-resolved thioflavin-t fluorescence can report on morphological differences in amyloid fibrils formed by aβ(1-40) and aβ(1-42). *Biochemical and Biophysical Research Communications*, 458(2):418–423, 2015. ISSN 0006-291X. doi: https://doi.org/10.1016/j.bbrc.2015.01.132. URL `https://www.sciencedirect.com/science/article/pii/S0006291X15001795`.

[81] Hironobu Naiki, Keiichi Higuchi, Masanori Hosokawa, and Toshio Takeda. Fluorometric determination of amyloid fibrils in vitro using the fluorescent dye, thioflavine T. *Anal. Biochem.*, 177(2):244–249, March 1989.

[82] Harry Levine III. Thioflavine t interaction with synthetic alzheimer's disease β-amyloid peptides: Detection of amyloid aggregation in solution. *Protein Science*, 2(3):404–410, 1993. doi: https://doi.org/10.1002/pro.5560020312. URL `https://onlinelibrary.wiley.com/doi/abs/10.1002/pro.5560020312`.

[83] Prabhat K. Singh, Manoj Kumbhakar, Haridas Pal, and Sukhendu Nath. Ultrafast bond twisting dynamics in amyloid fibril sensor. *The Journal of Physical Chemistry B*, 114(7):2541–2546, 2010. doi: 10.1021/jp911544r. URL `https://doi.org/10.1021/jp911544r`. PMID: 20095597.

[84] Prabhat K. Singh, Aruna K. Mora, and Sukhendu Nath. Ultrafast fluorescence spectroscopy reveals a dominant weakly-emissive population of fibril bound thioflavin-t. *Chem. Commun.*, 51:14042–14045, 2015. doi: 10.1039/C5CC04256A. URL `http://dx.doi.org/10.1039/C5CC04256A`.

[85] Arshdeep Sidhu, Jonathan Vaneyck, Christian Blum, Ine Segers-Nolten, and Vinod Subramaniam. Polymorph-specific distribution of binding sites determines thioflavin-t fluorescence intensity in α-synuclein fibrils. *Amyloid*, 25 (3):189–196, 2018. doi: 10.1080/13506129.2018.1517736. URL `https://doi.org/10.1080/13506129.2018.1517736`. PMID: 30486688.

[86] Sara Anselmo, Giuseppe Sancataldo, and Valeria Vetri. Deciphering amyloid fibril molecular maturation through flim-phasor analysis of thioflavin t. *Biophysical Reports*, 4(1):100145, 2024. ISSN 2667-0747. doi: https://doi.org/10.1016/j.bpr.2024.100145. URL `https://www.sciencedirect.com/science/article/pii/S2667074724000041`.

[87] Xin Zhou, Dirk Fennema Galparsoro, Anders Ostergaard Madsen, Valeria Vetri, Marco van de Weert, Hanne Morck Nielsen, and Vito Foderà. Polysorbate 80 controls morphology, structure and stability of human insulin amyloid-like spherulites. *Journal of Colloid and Interface Science*, 606: 1928–1939, 2022. ISSN 0021-9797. doi: https://doi.org/10.1016/j.jcis.2021.09.132. URL `https://www.sciencedirect.com/science/article/pii/S0021979721015915`.

[88] Maria Agnese Morando, Francesca Venturella, Martina Sollazzo, Elisa Monaca, Raffaele Sabbatella, Valeria Vetri, Rosa Passantino, Annalisa Pastore, and Caterina Alfano. Solution structure of recombinant pvfp-5β reveals insights into mussel adhesion. *Communications Biology*, 5(1):739, Jul 2022. ISSN 2399-3642. doi: 10.1038/s42003-022-03699-w. URL `https://doi.org/10.1038/s42003-022-03699-w`.

[89] Gregorio Weber and Fay J. Farris. Synthesis and spectral properties of a hydrophobic fluorescent probe: 6-propionyl-2-(dimethylamino)naphthalene. *Biochemistry*, 18(14):3075–3078, 1979. doi: 10.1021/bi00581a025. URL `https://doi.org/10.1021/bi00581a025`. PMID: 465454.

[90] German Gunther, Leonel Malacrida, David M. Jameson, Enrico Gratton, and Susana A. Sánchez. Laurdan since weber: The quest for visualizing membrane heterogeneity. *Accounts of Chemical Research*, 54(4):976–987, 2021. doi: 10.1021/acs.accounts.0c00687. URL `https://doi.org/10.1021/acs.accounts.0c00687`. PMID: 33513300.

[91] J. Zeng and P.L. Chong. Effect of ethanol-induced lipid interdigitation on the membrane solubility of prodan, acdan, and laurdan. *Biophysical*

Journal, 68(2):567–573, 1995. ISSN 0006-3495. doi: https://doi.org/ 10.1016/S0006-3495(95)80218-3. URL `https://www.sciencedirect. com/science/article/pii/S0006349595802183`.

[92] Henrik Seir Thoke, Asger Tobiesen, Jonathan Brewer, Per Lyngs Hansen, Roberto P. Stock, Lars F. Olsen, and Luis A. Bagatolli. Tight coupling of metabolic oscillations and intracellular water dynamics in saccharomyces cerevisiae. *PLOS ONE*, 10(2):1–16, 02 2015. doi: 10.1371/journal.pone. 0117308. URL `https://doi.org/10.1371/journal.pone.0117308`.

[93] Agustín Mangiarotti, Macarena Siri, Nicky W. Tam, Ziliang Zhao, Leonel Malacrida, and Rumiana Dimova. Biomolecular condensates modulate membrane lipid packing and hydration. *Nature Communications*, 14(1):6081, Sep 2023. ISSN 2041-1723. doi: 10.1038/s41467-023-41709-5. URL `https://doi.org/10.1038/s41467-023-41709-5`.

[94] Irene Vorontsova, Alexander Vallmitjana, Belén Torrado, Thomas F. Schilling, James E. Hall, Enrico Gratton, and Leonel Malacrida. In vivo macromolecular crowding is differentially modulated by aquaporin 0 in zebrafish lens: Insights from a nanoenvironment sensor and spectral imaging. *Science Advances*, 8(7):eabj4833, 2022. doi: 10.1126/sciadv.abj4833. URL `https://www.science.org/doi/abs/10.1126/sciadv.abj4833`.

[95] T Parasassi, G De Stasio, A d'Ubaldo, and E Gratton. Phase fluctuation in phospholipid membranes revealed by laurdan fluorescence. *Biophys. J.*, 57 (6):1179–1186, June 1990.

[96] Filippo Begarani, Francesca D'Autilia, Giovanni Signore, Ambra Del Grosso, Marco Cecchini, Enrico Gratton, Fabio Beltram, and Francesco Cardarelli. Capturing metabolism-dependent solvent dynamics in the lumen of a trafficking lysosome. *ACS Nano*, (acsna8b07682), January 2019.

[97] Santiago Otaiza-González, Manuel Cabadas, German Robert, Roberto P Stock, Leonel Malacrida, Ramiro Lascano, and Luis A Bagatolli. The innards of the cell: studies of water dipolar relaxation using the ACDAN fluorescent probe. *Methods Appl. Fluoresc.*, 10(4):044010, October 2022.

[98] Stefania Perticaroli, Georg Ehlers, Christopher B. Stanley, Eugene Mamontov, Hugh O'Neill, Qiu Zhang, Xiaolin Cheng, Dean A. A. Myles, John

Katsaras, and Jonathan D. Nickels. Description of hydration water in protein (green fluorescent protein) solution. *Journal of the American Chemical Society*, 139(3):1098–1105, 2017. doi: 10.1021/jacs.6b08845. URL `https://doi.org/10.1021/jacs.6b08845`. PMID: 27783480.

[99] Pan Tan, Yihao Liang, Qin Xu, Eugene Mamontov, Jinglai Li, Xiangjun Xing, and Liang Hong. Gradual crossover from subdiffusion to normal diffusion: A many-body effect in protein surface water. *Phys. Rev. Lett.*, 120: 248101, Jun 2018. doi: 10.1103/PhysRevLett.120.248101. URL `https://link.aps.org/doi/10.1103/PhysRevLett.120.248101`.

[100] A. Diaspro, M. Faretta, and P. Sapuppo. *Confocal Microscopy*. Leica Microsystems, 2008.

[101] James Pawley. *Handbook of biological confocal microscopy*, volume 236. Springer Science & Business Media, 2006.

[102] Douglas B. Murphy and Michael W. Davidson. *Fluorescence Microscopy*, chapter 11, pages 199–231. John Wiley & Sons, Ltd, 2012. ISBN 9781118382905. doi: 10.1002/9781118382905.ch11.

[103] Niklas Lorén, Joel Hagman, Jenny K Jonasson, Hendrik Deschout, Diana Bernin, Francesca Cella-Zanacchi, Alberto Diaspro, James G McNally, Marcel Ameloot, Nick Smisdom, Magnus Nydén, Anne-Marie Hermansson, Mats Rudemo, and Kevin Braeckmans. Fluorescence recovery after photobleaching in material and life sciences: putting theory into practice. *Q. Rev. Biophys.*, 48(3):323–387, August 2015.

[104] Warren Zipfel, Rebecca Williams, and Watt Webb. Nonlinear magic: multiphoton microscopy in the biosciences. *Nature biotechnology*, 21:1369–77, 2003. doi: 10.1038/nbt899.

[105] Monica Monici. Cell and tissue autofluorescence research and diagnostic application. *Biotechnology annual review*, 11:227–56, 2005. doi: 10.1016/S1387-2656(05)11007-2.

[106] S. Liao, Y. Sun, and U. Coskun. Flim analysis using the phasor plots. Technical report, Iss, Inc., 2015.

[107] Michelle A Digman, Valeria R Caiolfa, Moreno Zamai, and Enrico Gratton. The phasor approach to fluorescence lifetime imaging analysis. *Biophys. J.*, 94(2):L14–L16, January 2008.

[108] Yuansheng Sun and Shih-Chu Liao. The ultimate phasor plot and beyond. 2016. URL https://api.semanticscholar.org/CorpusID: 173176370.

[109] Suman Ranjit, Leonel Malacrida, David M. Jameson, and Enrico Gratton. Fit-free analysis of fluorescence lifetime imaging data using the phasor approach. *Nature Protocols*, 13(9):1979–2004, Sep 2018. ISSN 1750-2799. doi: 10.1038/s41596-018-0026-5. URL https://doi.org/10.1038/s41596-018-0026-5.

[110] Gabriele Bonaventura, Maria Luisa Barcellona, Ottavia Golfetto, Jamison L. Nourse, Lisa A. Flanagan, and Enrico Gratton. Laurdan monitors different lipids content in eukaryotic membrane during embryonic neural development. *Cell Biochemistry and Biophysics*, 70(2):785–794, Nov 2014. ISSN 1559-0283. doi: 10.1007/s12013-014-9982-8. URL https://doi.org/10.1007/s12013-014-9982-8.

[111] Tamara Topală, Andreea Bodoki, Luminiţa Oprean, and Radu Oprean. Bovine serum albumin interactions with metal complexes. *Med. Pharm. Rep.*, 87(4):215–219, November 2014.

[112] T. Peters. *All About Albumin: Biochemistry, Genetics, and Medical Applications*. Elsevier Science, 1995. ISBN 9780080527048. URL https://books.google.it/books?id=i1DC3KlTAB8C.

[113] Rosario Oliva, Sudeshna Banerjee, Hasan Cinar, Christiane Ehrt, and Roland Winter. Alteration of protein binding affinities by aqueous two-phase systems revealed by pressure perturbation. *Scientific Reports*, 10(1):8074, May 2020. ISSN 2045-2322. doi: 10.1038/s41598-020-65053-6. URL https://doi.org/10.1038/s41598-020-65053-6.

[114] Rui Lu, Wen-Wei Li, Abraham Katzir, Yosef Raichlin, Han-Qing Yu, and Boris Mizaikoff. Probing the secondary structure of bovine serum albumin during heat-induced denaturation using mid-infrared fiberoptic sensors. *Analyst*, 140:765–770, 2015. doi: 10.1039/C4AN01495B. URL http://dx.doi.org/10.1039/C4AN01495B.

[115] Mohammad Shahid and Har Mohindra Chawla. Dansylated adenine as a molecular probe for exploring hydrophobic pocket of bovine serum albumin (bsa) and its utility for mercury ion recognition. *Journal of Luminescence*, 188:460–464, 2017. ISSN 0022-2313. doi: https://doi.org/10.1016/j.

jlumin.2017.05.005. URL https://www.sciencedirect.com/science/article/pii/S0022231316318300.

[116] Andrea Testa, Mirco Dindo, Aleksander A Rebane, Babak Nasouri, Robert W Style, Ramin Golestanian, Eric R Dufresne, and Paola Laurino. Sustained enzymatic activity and flow in crowded protein droplets. *Nat. Commun.*, 12(1), November 2021.

[117] Hurija Džudžević Čančar, Matic Belak Vivod, Vojko Vlachy, and Miha Lukšič. Phase stability of aqueous mixtures of bovine serum albumin with low molecular mass salts in presence of polyethylene glycol. *Journal of Molecular Liquids*, 349:118477, 2022. ISSN 0167-7322. doi: https://doi.org/10.1016/j.molliq.2022.118477. URL https://www.sciencedirect.com/science/article/pii/S0167732222000125.

[118] Fajun Zhang, Sophie Weggler, Michael J. Ziller, Luca Ianeselli, Benjamin S. Heck, Andreas Hildebrandt, Oliver Kohlbacher, Maximilian W. A. Skoda, Robert M. J. Jacobs, and Frank Schreiber. Universality of protein reentrant condensation in solution induced by multivalent metal ions. *Proteins: Structure, Function, and Bioinformatics*, 78(16):3450–3457, 2010. doi: https://doi.org/10.1002/prot.22852. URL https://onlinelibrary.wiley.com/doi/abs/10.1002/prot.22852.

[119] F. Zhang, M. W. A. Skoda, R. M. J. Jacobs, S. Zorn, R. A. Martin, C. M. Martin, G. F. Clark, S. Weggler, A. Hildebrandt, O. Kohlbacher, and F. Schreiber. Reentrant condensation of proteins in solution induced by multivalent counterions. *Phys. Rev. Lett.*, 101:148101, Sep 2008. doi: 10.1103/PhysRevLett.101.148101. URL https://link.aps.org/doi/10.1103/PhysRevLett.101.148101.

[120] Jens Brange and Lotte Langkjœr. *Insulin Structure and Stability*, pages 315–350. Springer US, Boston, MA, 1993. ISBN 978-1-4899-1236-7. doi: 10.1007/978-1-4899-1236-7_11. URL https://doi.org/10.1007/978-1-4899-1236-7_11.

[121] Kristin R. Domike and Athene M. Donald. Thermal dependence of thermally induced protein spherulite formation and growth: Kinetics of β-lactoglobulin and insulin. *Biomacromolecules*, 8(12):3930–3937, 2007. doi: 10.1021/bm7009224. URL https://doi.org/10.1021/bm7009224. PMID: 18039002.

[122] Camilla Thorlaksen, Martin Busch Neergaard, Minna Groenning, and Vito Foderà. *Reproducible Formation of Insulin Superstructures: Amyloid-Like Fibrils, Spherulites, and Particulates*, pages 297–309. Springer US, New York, NY, 2023. ISBN 978-1-0716-2597-2. doi: 10.1007/978-1-0716-2597-2_20. URL https://doi.org/10.1007/978-1-0716-2597-2_20.

[123] Kirsten Gade Malmos, Luis M. Blancas-Mejia, Benedikt Weber, Johannes Buchner, Marina Ramirez-Alvarado, Hironobu Naiki, and Daniel Otzen. Tht 101: a primer on the use of thioflavin t to investigate amyloid formation. *Amyloid*, 24(1):1–16, 2017. doi: 10.1080/13506129.2017.1304905. URL https://doi.org/10.1080/13506129.2017.1304905. PMID: 28393556.

[124] Fabio Librizzi, Vito Foderà, Valeria Vetri, Caterina Lo Presti, and Maurizio Leone. Effects of confinement on insulin amyloid fibrils formation. *Eur. Biophys. J.*, 36(7):711–715, August 2007.

[125] Stefan Grudzielanek, Vytautas Smirnovas, and Roland Winter. Solvation-assisted pressure tuning of insulin fibrillation: From novel aggregation pathways to biotechnological applications. *J. Mol. Biol.*, 356(2):497–509, February 2006.

[126] Mauro Manno, Emanuela Fabiola Craparo, Alessandro Podestà, Donatella Bulone, Rita Carrotta, Vincenzo Martorana, Guido Tiana, and Pier Luigi San Biagio. Kinetics of different processes in human insulin amyloid formation. *Journal of Molecular Biology*, 366(1):258–274, 2007. ISSN 0022-2836. doi: https://doi.org/10.1016/j.jmb.2006.11.008. URL https://www.sciencedirect.com/science/article/pii/S0022283606015373.

[127] Mark R.H. Krebs, Kristin R. Domike, and Athene M. Donald. Protein aggregation: more than just fibrils. *Biochemical Society Transactions*, 37(4): 682–686, 07 2009. ISSN 0300-5127. doi: 10.1042/BST0370682. URL https://doi.org/10.1042/BST0370682.

[128] V Sluzky, J A Tamada, A M Klibanov, and R Langer. Kinetics of insulin aggregation in aqueous solutions upon agitation in the presence of hydrophobic surfaces. *Proceedings of the National Academy of Sciences*, 88(21):9377–9381, 1991. doi: 10.1073/pnas.88.21.9377. URL https://www.pnas.org/doi/abs/10.1073/pnas.88.21.9377.

[129] J. S. Sharp, J. A. Forrest, and R. A. L. Jones. Surface denaturation and amyloid fibril formation of insulin at model lipid-water interfaces. *Biochemistry*, 41(52):15810–15819, 2002. doi: 10.1021/bi020525z. URL `https://doi.org/10.1021/bi020525z`. PMID: 12501210.

[130] Shanghao Li and Roger M. Leblanc. Aggregation of insulin at the interface. *The Journal of Physical Chemistry B*, 118(5):1181–1188, 2014. doi: 10.1021/jp4101202. URL `https://doi.org/10.1021/jp4101202`. PMID: 24328184.

[131] Victoria Sluzky, Alexander M. Klibanov, and Robert Langer. Mechanism of insulin aggregation and stabilization in agitated aqueous solutions. *Biotechnology and Bioengineering*, 40(8):895–903, 1992. doi: https://doi.org/10.1002/bit.260400805. URL `https://analyticalsciencejournals.onlinelibrary.wiley.com/doi/abs/10.1002/bit.260400805`.

[132] Paula Nilsson, Tommy Nylander, and Svend Havelund. Adsorption of insulin on solid surfaces in relation to the surface properties of the monomeric and oligomeric forms. *Journal of Colloid and Interface Science*, 144(1):145–152, 1991. ISSN 0021-9797. doi: https://doi.org/10.1016/0021-9797(91)90244-3. URL `https://www.sciencedirect.com/science/article/pii/0021979791902443`.

[133] Young Min Kwon, Miroslav Baudys, Kristine Knutson, and Sung Wan Kim. In situ study of insulin aggregation induced by water-organic solvent interface. *Pharmaceutical Research*, 18(12):1754–1759, Dec 2001. ISSN 1573-904X. doi: 10.1023/A:1013334916162. URL `https://doi.org/10.1023/A:1013334916162`.

[134] Ying Wang and Onofrio Annunziata. Comparison between protein-polyethylene glycol (peg) interactions and the effect of peg on protein-protein interactions using the liquid-liquid phase transition. *The Journal of Physical Chemistry B*, 111(5):1222–1230, 2007. doi: 10.1021/jp065608u. URL `https://doi.org/10.1021/jp065608u`. PMID: 17266278.

[135] Shinpei Tanaka, Mitsuo Ataka, and Kohzo Ito. Pattern formation and coarsening during metastable phase separation in lysozyme solutions. *Phys. Rev. E*, 65:051804, May 2002. doi: 10.1103/PhysRevE.65.051804. URL `https://link.aps.org/doi/10.1103/PhysRevE.65.051804`.

[136] Noga Kozer and Gideon Schreiber. Effect of crowding on protein–protein association rates: Fundamental differences between low and high mass crowding agents. *Journal of Molecular Biology*, 336(3):763–774, 2004. ISSN 0022-2836. doi: https://doi.org/10.1016/j.jmb.2003.12.008. URL `https://www.sciencedirect.com/science/article/pii/S0022283603015006`.

[137] Saumyak Mukherjee and Lars V. Schäfer. Thermodynamic forces from protein and water govern condensate formation of an intrinsically disordered protein domain. *Nature Communications*, 14(1):5892, Sep 2023. ISSN 2041-1723. doi: 10.1038/s41467-023-41586-y. URL `https://doi.org/10.1038/s41467-023-41586-y`.

[138] Sashary Ramos, Janine Kamps, Simone Pezzotti, Konstanze F. Winklhofer, Jörg Tatzelt, and Martina Havenith. Hydration makes a difference! how to tune protein complexes between liquid–liquid and liquid–solid phase separation. *Phys. Chem. Chem. Phys.*, 25:28063–28069, 2023. doi: 10.1039/D3CP03299J. URL `http://dx.doi.org/10.1039/D3CP03299J`.

[139] Kozo. Hamaguchi and E. Peter. Geiduschek. The effect of electrolytes on the stability of the deoxyribonucleate helix. *Journal of the American Chemical Society*, 84(8):1329–1338, 1962. doi: 10.1021/ja00867a001. URL `https://doi.org/10.1021/ja00867a001`.

[140] I Yu and M Nagaoka. Slowdown of water diffusion around protein in aqueous solution with ectoine. *Chemical Physics Letters*, 388(4):316–321, 2004. ISSN 0009-2614. doi: https://doi.org/10.1016/j.cplett.2004.02.104. URL `https://www.sciencedirect.com/science/article/pii/S0009261404003197`.

[141] Daniela Russo. The impact of kosmotropes and chaotropes on bulk and hydration shell water dynamics in a model peptide solution. *Chemical Physics*, 345(2):200–211, 2008. ISSN 0301-0104. doi: https://doi.org/10.1016/j.chemphys.2007.08.001. URL `https://www.sciencedirect.com/science/article/pii/S0301010407003333`. Neutrons in Biology.

[142] Hussein Chaaban, Jijo J. Vallooran, Marco van de Weert, and Vito Foderà. Ion-mediated morphological diversity in protein amyloid systems. *The Journal of Physical Chemistry Letters*, 13(16):3586–3593, 2022. doi: 10.1021/acs.jpclett.2c00182. URL `https://doi.org/10.1021/acs.jpclett.2c00182`. PMID: 35426676.

[143] Georg Krainer, Timothy J. Welsh, Jerelle A. Joseph, Jorge R. Espinosa, Sina Wittmann, Ella de Csilléry, Akshay Sridhar, Zenon Toprakcioglu, Giedre Gudiškytė, Magdalena A. Czekalska, William E. Arter, Jordina Guillén-Boixet, Titus M. Franzmann, Seema Qamar, Peter St George-Hyslop, Anthony A. Hyman, Rosana Collepardo-Guevara, Simon Alberti, and Tuomas P. J. Knowles. Reentrant liquid condensate phase of proteins is stabilized by hydrophobic and non-ionic interactions. *Nature Communications*, 12(1): 1085, Feb 2021. ISSN 2041-1723. doi: 10.1038/s41467-021-21181-9. URL `https://doi.org/10.1038/s41467-021-21181-9`.

[144] H Uedaira and H Uedaira. Role of hydration of polyhydroxy compounds in biological systems. *Cellular and molecular biology (Noisy-le-Grand, France)*, 47(5):823—829, July 2001. ISSN 0145-5680. URL `http://europepmc.org/abstract/MED/11728096`.

[145] George I. Makhatadze and Peter L. Privalov. Protein interactions with urea and guanidinium chloride: A calorimetric study. *Journal of Molecular Biology*, 226(2):491–505, 1992. ISSN 0022-2836. doi: https://doi.org/10.1016/0022-2836(92)90963-K. URL `https://www.sciencedirect.com/science/article/pii/002228369290963K`.

[146] Andrew M.J. Crowell, Mark J. Wall, and Alan A. Doucette. Maximizing recovery of water-soluble proteins through acetone precipitation. *Analytica Chimica Acta*, 796:48–54, 2013. ISSN 0003-2670. doi: https://doi.org/10.1016/j.aca.2013.08.005. URL `https://www.sciencedirect.com/science/article/pii/S0003267013010532`.

[147] Onofrio Annunziata, Neer Asherie, Aleksey Lomakin, Jayanti Pande, Olutayo Ogun, and George B. Benedek. Effect of polyethylene glycol on the liquid–liquid phase transition in aqueous protein solutions. *Proceedings of the National Academy of Sciences*, 99(22):14165–14170, 2002. doi: 10.1073/pnas.212507199. URL `https://www.pnas.org/doi/abs/10.1073/pnas.212507199`.

[148] Conan J. Fee and James M. Van Alstine. Peg-proteins: Reaction engineering and separation issues. *Chemical Engineering Science*, 61(3):924–939, 2006. ISSN 0009-2509. doi: https://doi.org/10.1016/j.ces.2005.04.040. URL `https://www.sciencedirect.com/science/article/pii/S0009250905003003`. Biomolecular Engineering.

[149] Ying Wang, Ramil F. Latypov, Aleksey Lomakin, Julie A. Meyer, Bruce A. Kerwin, Suresh Vunnum, and George B. Benedek. Quantitative evaluation of colloidal stability of antibody solutions using peg-induced liquid–liquid phase separation. *Molecular Pharmaceutics*, 11(5):1391–1402, 2014. doi: 10.1021/mp400521b. URL `https://doi.org/10.1021/mp400521b`. PMID: 24679215.

[150] Rajiv Bhat and Serge N. Timasheff. Steric exclusion is the principal source of the preferential hydration of proteins in the presence of polyethylene glycols. *Protein Science*, 1(9):1133–1143, 1992. doi: https://doi.org/10.1002/pro.5560010907. URL `https://onlinelibrary.wiley.com/doi/abs/10.1002/pro.5560010907`.

[151] Madeleine R. Fries, Nina F. Conzelmann, Luzie Günter, Olga Matsarskaia, Maximilian W. A. Skoda, Robert M. J. Jacobs, Fajun Zhang, and Frank Schreiber. Bulk phase behavior vs interface adsorption: Specific multivalent cation and anion effects on bsa interactions. *Langmuir*, 37(1):139–150, 2021. doi: 10.1021/acs.langmuir.0c02618. URL `https://doi.org/10.1021/acs.langmuir.0c02618`. PMID: 33393312.

[152] Chinmaya Kumar Patel, Shivendra Singh, Bhawna Saini, and Tushar Kanti Mukherjee. Macromolecular crowding-induced unusual liquid–liquid phase separation of human serum albumin via soft protein–protein interactions. *The Journal of Physical Chemistry Letters*, 13(16):3636–3644, 2022. doi: 10.1021/acs.jpclett.2c00307. URL `https://doi.org/10.1021/acs.jpclett.2c00307`. PMID: 35435684.

[153] Bhawna Saini and Tushar Kanti Mukherjee. Biomolecular condensates regulate enzymatic activity under a crowded milieu: Synchronization of liquid–liquid phase separation and enzymatic transformation. *The Journal of Physical Chemistry B*, 127(1):180–193, 2023. doi: 10.1021/acs.jpcb.2c07684. URL `https://doi.org/10.1021/acs.jpcb.2c07684`. PMID: 36594499.

[154] Beatriz Farruggia, Bibiana Nerli, Hernán Di Nuci, Ruben Rigatusso, and Guillermo Picó. Thermal features of the bovine serum albumin unfolding by polyethylene glycols. *International Journal of Biological Macromolecules*, 26(1):23–33, 1999. ISSN 0141-8130. doi: https://doi.org/10.1016/S0141-8130(99)00061-6. URL `https://www.sciencedirect.com/science/article/pii/S0141813099000616`.

[155] Jing-jing Lai, Huai-yu Yan, Yan Liu, and Yanbin Huang. Effects of peg molecular weight on its interaction with albumin. *Chinese Journal of Polymer Science*, 33(10):1373–1379, Oct 2015. ISSN 1439-6203. doi: 10.1007/s10118-015-1687-y. URL https://doi.org/10.1007/s10118-015-1687-y.

[156] Hiroya Tange, Daisuke Ishibashi, Takehiro Nakagaki, Yuzuru Taguchi, Yuji O Kamatari, Hiroki Ozawa, and Noriyuki Nishida. Liquid–liquid phase separation of full-length prion protein initiates conformational conversion in vitro. *J. Biol. Chem.*, 296(100367):100367, January 2021.

[157] Wojciech Dzwolak, Stefan Grudzielanek, Vytautas Smirnovas, Revanur Ravindra, Chiara Nicolini, Ralf Jansen, Anna Loksztejn, Sylwester Porowski, and Roland Winter. Ethanol-perturbed amyloidogenic self-assembly of insulin: Looking for origins of amyloid strains. *Biochemistry*, 44(25):8948–8958, 2005. doi: 10.1021/bi050281t. URL https://doi.org/10.1021/bi050281t. PMID: 15966720.

[158] R Ghosh, R N Samajdar, Aninda Jiban Bhattacharyya, and B Bagchi. Composition dependent multiple structural transformations of myoglobin in aqueous ethanol solution: A combined experimental and theoretical study. *J. Chem. Phys.*, 143(1), July 2015.

[159] Rutao Liu, Pengfei Qin, Li Wang, Xingchen Zhao, Yihong Liu, and Xiaopeng Hao. Toxic effects of ethanol on bovine serum albumin. *J. Biochem. Mol. Toxicol.*, 24(1):66–71, January 2010.

[160] Fredrik G. Bäcklund and Niclas Solin. Tuning the aqueous self-assembly process of insulin by a hydrophobic additive. *RSC Adv.*, 5:92254–92262, 2015. doi: 10.1039/C5RA16144D. URL http://dx.doi.org/10.1039/C5RA16144D.

[161] Nadeem Javid, Karsten Vogtt, Chris Krywka, Metin Tolan, and Roland Winter. Protein–protein interactions in complex cosolvent solutions. *ChemPhysChem*, 8(5):679–689, 2007. doi: https://doi.org/10.1002/cphc.200600631. URL https://chemistry-europe.onlinelibrary.wiley.com/doi/abs/10.1002/cphc.200600631.

[162] Serge N. Timasheff. Protein-solvent preferential interactions, protein hydration, and the modulation of biochemical reactions by solvent components. *Proceedings of the National Academy of Sciences*, 99(15):9721–9726, 2002.

doi: 10.1073/pnas.122225399. URL `https://www.pnas.org/doi/abs/10.1073/pnas.122225399`.

[163] Ernesto E Ambroggio, Guadalupe S Costa Navarro, Luis Benito Pérez Socas, Luis A Bagatolli, and Andrea V Gamarnik. Dengue and zika virus capsid proteins bind to membranes and self-assemble into liquid droplets with nucleic acids. *J. Biol. Chem.*, 297(3):101059, September 2021.

[164] Francesco Palomba, Lorenzo Scipioni, Enrico Gratton, and Michelle Digman. Water dynamics of a model protein phase separation via fluorescence lifetime and spectral analysis of acdan. *Biophysical Journal*, 118:308a, 02 2020. doi: 10.1016/j.bpj.2019.11.1741.

[165] Xin Zhou, Anders Wilgaard Sinkjær, Min Zhang, Henrik Dahl Pinholt, Hanne Mørck Nielsen, Nikos S Hatzakis, Marco van de Weert, and Vito Foderà. Heterogeneous and surface-catalyzed amyloid aggregation monitored by spatially resolved fluorescence and single molecule microscopy. *J. Phys. Chem. Lett.*, 14(4):912–919, February 2023.

[166] Justyna Łuczak, Anna Latowska, and Jan Hupka. Micelle formation of tween 20 nonionic surfactant in imidazolium ionic liquids. *Colloids and Surfaces A: Physicochemical and Engineering Aspects*, 471:26–37, 2015. ISSN 0927-7757. doi: https://doi.org/10.1016/j.colsurfa.2015.02.008. URL `https://www.sciencedirect.com/science/article/pii/S0927775715001284`.

[167] Giuseppe Arrabito, Felicia Cavaleri, Alessandro Porchetta, Francesco Ricci, Valeria Vetri, Maurizio Leone, and Bruno Pignataro. Printing life-inspired subcellular scale compartments with autonomous molecularly crowded confinement. *Advanced Biosystems*, 3(7):1900023, 2019. doi: https://doi.org/10.1002/adbi.201900023. URL `https://onlinelibrary.wiley.com/doi/abs/10.1002/adbi.201900023`.

[168] Judith E Berlier, Anca Rothe, Gayle Buller, Jolene Bradford, Diane R Gray, Brian J Filanoski, William G Telford, Stephen Yue, Jixiang Liu, Ching-Ying Cheung, Wesley Chang, James D Hirsch, Joseph M Beechem Rosaria P. Haugland, and Richard P Haugland. Quantitative comparison of long-wavelength alexa fluor dyes to cy dyes: Fluorescence of the dyes and their bioconjugates. *J. Histochem. Cytochem.*, 51(12):1699–1712, December 2003.

[169] Nataliya Panchuk-Voloshina, Rosaria P Haugland, Janell Bishop-Stewart, Mahesh K Bhalgat, Paul J Millard, Fei Mao, Wai-Yee Leung, and Richard P Haugland. Alexa dyes, a series of new fluorescent dyes that yield exceptionally bright, photostable conjugates. *J. Histochem. Cytochem.*, 47(9):1179–1188, September 1999.

[170] Atul K. Srivastava, Jay M. Pittman, Jonathan Zerweck, Bharat S. Venkata, Patrick C. Moore, Joseph R. Sachleben, and Stephen C. Meredith. *β*-amyloid aggregation and heterogeneous nucleation. *Protein Science*, 28 (9):1567–1581, 2019. doi: https://doi.org/10.1002/pro.3674. URL `https://onlinelibrary.wiley.com/doi/abs/10.1002/pro.3674`.

[171] Fulvio Grigolato and Paolo Arosio. The role of surfaces on amyloid formation. *Biophys. Chem.*, 270(106533):106533, March 2021.

[172] L. Tumbek and A. Winkler. Attachment limited versus diffusion limited nucleation of organic molecules: Hexaphenyl on sputter-modified mica. *Surface Science*, 606(15):L55–L58, 2012. ISSN 0039-6028. doi: https://doi.org/10.1016/j.susc.2012.03.018. URL `https://www.sciencedirect.com/science/article/pii/S0039602812001136`.

[173] Anna I. Sulatskaya, Andrey V. Lavysh, Alexander A. Maskevich, Irina M. Kuznetsova, and Konstantin K. Turoverov. Thioflavin t fluoresces as excimer in highly concentrated aqueous solutions and as monomer being incorporated in amyloid fibrils. *Scientific Reports*, 7(1):2146, May 2017. ISSN 2045-2322. doi: 10.1038/s41598-017-02237-7. URL `https://doi.org/10.1038/s41598-017-02237-7`.

[174] Sara Anselmo, Tiziana Avola, Kleopatra Kalouta, Salvatore Cataldo, Giuseppe Sancataldo, Nicola Muratore, Vito Foderà, Valeria Vetri, and Alberto Pettignano. Sustainable soy protein microsponges for efficient removal of lead (ii) from aqueous environments. *International Journal of Biological Macromolecules*, 239:124276, 2023. ISSN 0141-8130. doi: https://doi.org/10.1016/j.ijbiomac.2023.124276. URL `https://www.sciencedirect.com/science/article/pii/S0141813023011704`.

[175] Giuseppe Sancataldo, Sara Anselmo, and Valeria Vetri. Phasor-flim analysis of thioflavin t self-quenching in concanavalin amyloid fibrils. *Microscopy Research and Technique*, 83(7):811–816, 2020. doi: https://doi.org/10.1002/jemt.23472. URL `https://analyticalsciencejournals.onlinelibrary.wiley.com/doi/abs/10.1002/jemt.23472`.

[176] Anita Girelli, Hendrik Rahmann, Nafisa Begam, Anastasia Ragulskaya, Mario Reiser, Sivasurender Chandran, Fabian Westermeier, Michael Sprung, Fajun Zhang, Christian Gutt, and Frank Schreiber. Microscopic dynamics of liquid-liquid phase separation and domain coarsening in a protein solution revealed by x-ray photon correlation spectroscopy. *Phys. Rev. Lett.*, 126:138004, Apr 2021. doi: 10.1103/PhysRevLett.126.138004. URL `https://link.aps.org/doi/10.1103/PhysRevLett.126.138004`.

[177] Ying Zou, Hongmei Zheng, Yue Ning, Yang Yang, Qiuyuan Wen, and Songqing Fan. New insights into the important roles of phase seperation in the targeted therapy of lung cancer. *Cell & Bioscience*, 13(1):150, Aug 2023. ISSN 2045-3701. doi: 10.1186/s13578-023-01101-8. URL `https://doi.org/10.1186/s13578-023-01101-8`.

[178] Oleg G. Shpyrko. X-ray photon correlation spectroscopy. *Journal of Synchrotron Radiation*, 21(5):1057–1064, Sep 2014. doi: 10.1107/S1600577514018232. URL `https://doi.org/10.1107/S1600577514018232`.

[179] Anders Madsen, Andrei Fluerasu, and Beatrice Ruta. *Structural Dynamics of Materials Probed by X-Ray Photon Correlation Spectroscopy*, pages 1617–1641. Springer International Publishing, Cham, 2016. ISBN 978-3-319-14394-1. doi: 10.1007/978-3-319-14394-1_29. URL `https://doi.org/10.1007/978-3-319-14394-1_29`.

[180] Sooheyong Lee, W. Roseker, C. Gutt, B. Fischer, H. Conrad, F. Lehmkühler, I. Steinke, D. Zhu, H. Lemke, M. Cammarata, D.M. Fritz, P. Wochner, M. Castro-Colin, S. O. Hruszkewycz, P. H. Fuoss, G. B. Stephenson, G. Grübel, and A. Robert. Single shot speckle and coherence analysis of the hard x-ray free electron laser lcls. *Opt. Express*, 21(21):24647–24664, Oct 2013. doi: 10.1364/OE.21.024647. URL `https://opg.optica.org/oe/abstract.cfm?URI=oe-21-21-24647`.

[181] Marco Cammarata, Francesco Piazza, Germán Rivas, Giorgio Schirò, Piero Andrea Temussi, and Annalisa Pastore. Revitalizing an important field in biophysics: The new frontiers of molecular crowding. *Frontiers in Molecular Biosciences*, 10, 2023. ISSN 2296-889X. doi: 10.3389/fmolb.2023.1153996. URL `https://www.frontiersin.org/articles/10.3389/fmolb.2023.1153996`.

[182] Fivos Perakis and Christian Gutt. Towards molecular movies with x-ray photon correlation spectroscopy. *Phys. Chem. Chem. Phys.*, 22:19443–19453, 2020. doi: 10.1039/D0CP03551C. URL `http://dx.doi.org/10.1039/D0CP03551C`.